UNIVERSITÀ DEGLI STUDI DI PADOVA

Department of Industrial Engineering

TECHNICAL UNIVERSITY OF DENMARK

DTU-MEK – Section of Fluid Mechanics, Costal and Maritime Engineering

Master of Science Degree in Mechanical Engineering

Numerical simulation of the in-nozzle flow during the opening and closing of the fuel valve for two-stroke diesel engines

Supervisors: Prof. Giovanna Cavazzini

Università degli Studi di Padova

Prof. Jens Honoré Walther

Technical University of Denmark

Eng. Simon Matlok

MAN Energy Solutions

Master thesis by:

Lorenzo Zambon

1154346 – s171971

Academic year 2018-2019

Numerical simulation of in-nozzle flow during the opening and closing of a fuel valve for two-stroke diesel engines

Master Thesis

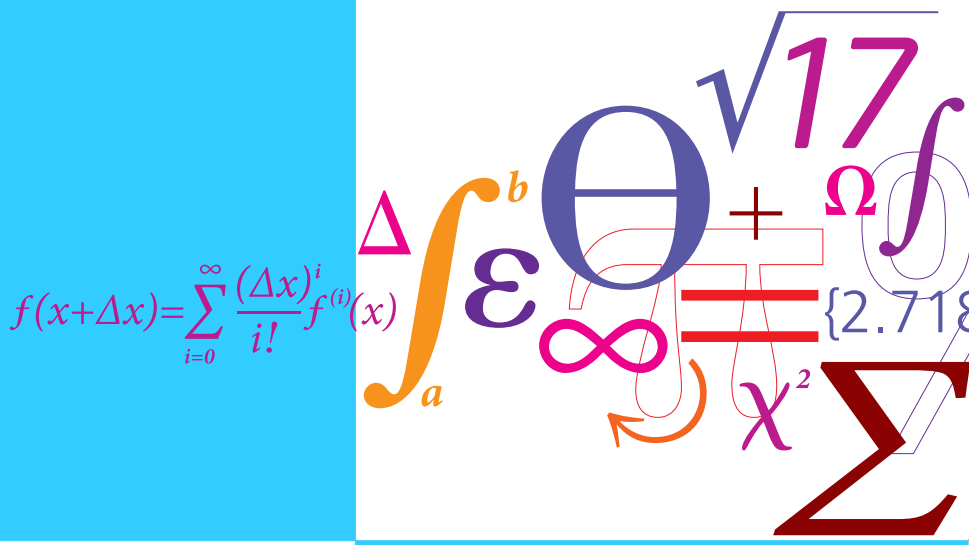

Lorenzo Zambon

DTU Mechanical Engineering

Section of Fluid Mechanics, Costal and Maritime Engineering

Università degli Studi di Padova

Department of Industrial Engineering

June 2019

Abstract

The strict emission standards for two-stroke slow-speed diesel engine used for marine propulsion have forced the manufacturers to conduct research on the fuel injection technology, sprays and combustion. The quality of combustion process is strictly related to the spray pattern and the scientific community agrees that the spray characteristics depend on a large extend on the in-nozzle flow, especially when cavitation appears. Cavitation enhances the mixture between the fuel core jet and the air, reducing the fuel consumption and the out-raw emission. In literature, most of the studies about cavitating flow in injectors have been performed in steady conditions: the fuel valve is at fixed lift, and the fluid has time to achieve the steady state. This model of the actual flow is accurate only when the main injection is considered, being the time-dominant event. To cope with the emission limits, pre-combustion and post-combustion injections are often adopted; in this case, the fast transients can not be neglected. In addition, experimental results could be obtained from the analysis of the flow in steady conditions, while it is not possible at the opening and closing of the fuel valve. For this reason, only little information is available and the flow is worth being investigated.

After the numerical validation of the cavitation model in transient condition, it was implemented in the actual geometry of the injector. The motion has been executed through the overset technology, one of the most popular method to move components in CFD simulations. The lack of experimental data forced to use in input the values of pressures and displacement from another one-dimensional code provided by MAN Energy Solutions. Despite this assumption, the mass flow and the pressure in the sac volume establish a satisfying agreement with the benchmarks, especially for the start of the injection. The cavitation regime known as supercavitation is observed in the nozzle holes and a relationship between the amount of vapor in the nozzles and time has been found. An additional investigation about in-nozzle cavitation is performed when the valve is at partial lift and the pressure at the boundaries is constant. Both in transient and steady simulations, hydrodynamic and string cavitation are observed.

Abstract (Italian)

Le stringenti normative riguardo le emissioni di motori diesel a due tempi per la propulsione navale ha incentivato la ricerca da parte dei costruttori; i principali ambiti di studio rigurdano i combustibili, l'iniezione e il processo di combustione. L'efficienza di quest'ultima è associata allo spray pattern e l'atomizzazione del getto dipende in larga misura dal flusso del combustibile negli ugelli di iniezione, specialmente quando si ha cavitazione. La cavitazione permette di migliorare la miscela di aria e combustibile, riducendo i consumi e le emissioni di incombusti. In letteratura, la maggior parte degli studi rigurdanti la cavitazione negli iniettori è svolta in condizioni stazionarie: la valvola dell'iniettore è alla massima alzata, le condizioni di pressione sono tempo invarianti e il fluido ha sufficiente tempo per raggiungere le condizioni stazionarie. Questo tipo di modellizzazione fluidodinamica dell'iniezione risulta essere accurato quando la sola iniezione prinicipale viene considerata, essendo questa la parte dominante dell'intero processo. A seguito delle limitazioni sulle emissioni, pre e post iniezioni sono spesso utilizzate nelle condizioni operative; in questo casto, i transitori dovuti alla apertura e chiusura della valvola non possono essere ignorati. In aggiunta, nonostante le pressioni e le dimensioni degli ugelli rendano complesso l'approccio sperimentale, è possible effetturare degli esperimenti quando la valvola si trova alla massima alzata. Al contrario ciò non è possibile nei transitori e dati sperimentali sono assenti in letteratura. Queste ragioni rendono lo studio del flusso di combustibile all'apertura e chiusura della valvola meritevole di approfondimento.

Dopo una validazione numerica delle equazioni responsabili del fenomeno di cavitazione in condizioni transitorie, queste sono state implementate in un modello CFD dell'iniettore. Il movimento della valvola è stato possibile grazie all'utilizzo della tecnologia overset, uno dei metodi più popolari per simulare il moto di componenti nei software CFD. La mancanza di dati sperimentali ha richiesto l'utilizzo in input di valori numerici derivanti da altri strumenti monodimensionali. Nonostante questa assunzione, le portate di massa e la pressione nel volume di sac mostrano una corrispondenza con i valori di benchmark, specialmente per quanto concerne l'avvio dell'iniezione. Il regime di cavitazione noto in letteratura come *supercavitation* è stato osservato negli ugelli e una relazione tra l'alzata dello spillo e volume di vapore di combustibile è stata ricavata. Uno studio aggiuntivo rigurdo il fenomeno di cavitazione negli ugelli in condizioni stazionarie e ad alzate parziali dello spillo è stata effettuato. Sia nelle simulazioni transitorie che in quelle in condizioni stazionarie, i meccanismi di cavitazione idrodinamica e dovuta ai moti vorticosi sono stati osservati.

Preface

This Master thesis was prepared at the department of Mechanical Engineering at the Technical University of Denmark (DTU), from the 28th of January to the 28th June 2019. The work fulfills the requirements for acquiring a Master degree in Mechanical Engineering at the Technical University of Denmark and Università degli Studi di Padova. The work has been carried out under the supervision of professors Jens Honoré Walther (DTU), Giovanna Cavazzini (UniPD) and the research engineer Simon Matlok, from the *Low Speed Engine* division of MAN Energy Solutions.

Kongens Lyngby, June 28, 2019

Lorenzo Zambon

Acknowledgements

I would like to express my gratitude for my supervisors, Jens Honoré Walther, Simon Matlok and Giovanna Cavazzini for their support and guidance through the project. Thank you for imparting your immense knowledge and expertise.

I want to thank all the friends I get in touch with during my studies in Padova and DTU; a special mention to Alberto, Gabriele, Federico, Cristiano, Marco, Alessandro, Elisa; I shared with you the best memories of my university life. Among the people I met in Denmark, I want to express my gratitude to Borja for the all the interesting conversation about fluid mechanics and CFD; I wish you a brilliant career. Finally, I would like to thank Per and Gitte for their hospitality and kindness.

Last, but definitely not least, I am greatly indebt to my parents, Stefano and Ledy, which provide unfailing support and continuous encouragement throughout my years of study.

Contents

List of Tables

List of Figures

Nomenclature

Abbreviations

Acronym	Meaning
CFD	Computational Fluid Dynamics
CM	Control Mass
CV	Control Volume
DNS	Direct Numerical Simulations
EDM	Electric Discharge Machining
EOI	End of Injection
EOS	Equation of State
FFT	Fast Fourier Transform
FIVA	Fuel Injection Valve Activation
HFO	Heavy Fuel Oil
IMO	International Maritime Organization
LES	Large Eddies Simulations
PMMA	Polymethylmethacrylate
SOI	Start of Injection
URANS	Unsteady Reynolds Averaged Navier-Stokes equations
VOC	Valve Covering Orifice
VOF	Volume of Fluid

Dimensionless Numbers

Symbol	Description	Definition
σ	Cavitation number (def.1)	$\sigma = \frac{p_i - p_{sat}}{\frac{1}{2}\rho u^2}$
C	Courant number	$\mathrm{C} = \frac{u\Delta t}{\Delta x}$
CN	Cavitation number (def.2)	$\mathrm{CN} = \frac{p_i - p_o}{p_o - p_{sat}}$
K	Cavitation number (def.3)	$\mathrm{K} = \frac{p_i - p_{sat}}{p_i - p_o}$
M	Mach number	$\mathrm{M} = \frac{u}{c}$
Re	Reynolds number	$\mathrm{Re} = \frac{uL}{\nu}$
St	Strouhal number	$\mathrm{St} = \frac{fL}{u}$

Greek Symbols

Symbol	Description	Dimensions	Units
α	Volume fraction	$-$	$-$
δ	Kronecker's delta	$-$	$-$
Δp	Pressure difference	$\mathrm{M\,L^{-1}\,T^{-2}}$	Pa
Δt	Time step	T	s
Δx	Grid size	L	m
ϵ	Roughness	L	m
γ	Surface tension	$\mathrm{M\,S^{-2}}$	$\mathrm{N\,m^{-1}}$
μ	Dynamic viscosity	$\mathrm{M\,L^{-1}\,T^{-1}}$	Pa s
μ_t	Turbulent viscosity	$\mathrm{M\,L^{-1}\,T^{-1}}$	Pa s
ν	Kinematic viscosity	$\mathrm{L^2\,S^{-1}}$	$\mathrm{m^2\,s^{-3}}$
Ω	Control Volume	$\mathrm{L^3}$	$\mathrm{m^3}$
ϕ	Generic intensive propriety	-	-
ρ	Density	$\mathrm{M\,L^{-3}}$	$\mathrm{kg\,m^{-3}}$

τ	Deviatoric stress tensor	M L^{-1} T^{-2}	Pa
τ_0	Wall shear stress	M L^{-1} T^{-2}	Pa
ξ	Borda-Carnot loss coefficient	-	-

Roman Symbols

Symbol	Description	Dimensions	Units
$\boldsymbol{b}$	Body forces	M L T^{-2}	N
$\boldsymbol{M}$	Momentum	M L T^{-1}	kg m s^{-1}
$\boldsymbol{n}$	Normal vector	-	-
$\boldsymbol{v}$	Velocity vector	L T^{-1}	m s^{-1}
$\boldsymbol{x}$	Position vector	L	m
$\dot{M}$	Momentum flow	M L T^{-2}	kg m s^{-2}
$\dot{m}$	Mass flow	M T^{-1}	kg s^{-1}
A	Area	L^2	m^2
c	Speed of sound	L T^{-1}	m s^{-1}
C_a	Contraction coefficient	-	-
C_d	Discharge coefficient	-	-
C_M	Momentum coefficient	-	-
C_v	Velocity coefficient	-	-
D	Diameter	L	m
d	Seeds' diameter	L	m
F	Friction coefficient	-	-
f	Frequency	T^{-1}	Hz
g	Gravity	L T^{-2}	m s^{-2}
k	Turbulent kinetic energy	L^2 T^2	m^2 s^2
n	Reboud's coefficient	-	-
n_0	Seeds' density	L^{-3}	m^{-3}
p	Pressure	M L^{-1} T^{-2}	Pa

p_{sat}	Saturation pressure	M L^{-1} T^{-2}	Pa
R	Radius	L	m
S	Surface	L^2	m^2
S_{α_i}	Source term i^{th} phase	-	-
T	Period	T	s
t	Time	T	s
u, v, w	Velocity components	L T^{-1}	m s^{-1}
U_f	Friction velocity	L T^{-1}	m s^{-1}
V	Volume	L^3	m^3
W	Molecular Wight	M MOL^{-1}	kg mol^{-1}
x, y, z	Position components	L	m
$y+$	Non dimensional wall coordinate	-	-

Subscripts

Symbol	Meaning
∞	Infinitely far
B	Bubble
c	Vena contracta
e	Entrance
i or 1	Inlet
L	Liquid
o or 2	Outlet
r	Reattachment point
V	Vapor

Superscripts

Symbol	Meaning
T	Transpose of
$(')$	Fluctuating component
$(\dot{})$	Time derivative
$(\bar{})$	Average
*	Non dimensional value

Chapter 1

Introduction

In the last fifty years, the growth of environmental awareness has led to public demand for environmental safeguards and remedies to air pollution. Under these circumstances, standards for the harmful exhaust produced by diesel engines were established and the regulations forced the manufactures to invest on research and development of new technologies. In common imaginary, diesel engine innovation is closely linked to the automotive industry; since the late seventies, more than 20 thousands patents have been registered in this sector [13]. Even today, although diesel engines have been called into question after the recent emission scandals, the major car firms are still pledging to invest billions on its development.

The maritime engineering industry has been affected by these standards more recently. The first international regulation on pollution due to merchant ships was ratified in 1997 by the International Maritime Organization (IMO) in the convention denominated MARPOL 73/78; the Annex VI, named *Prevention of Air Pollutants for Ships* came into force in May 2005. Year after year, the standards are continuously revised by limiting the amount of nitrogen oxides, sulphurs, hydrocarbons and soot. An overview of the evolution of the standards in terms of NO_x limits (similar plots could be obtained also for other exhausts) is presented in figure 1.1. The tightening of emission controls is evident from the analysis of the picture; in this regard, the percentage of the emission of NO_x has dropped of around 80% in the last 20 years and it will inevitably decrease further in future.

In this work, the focus is on slow-speed two-stroke diesel engines. This propulsion system is the most popular among the large freight ships; there are many different reasons for that. First of all, the two-stroke engine has as an higher power to weight ratio in comparison with the four stroke engine. In fact, there is a direct coupling between the crankshaft and the propeller, avoiding the need of reductor and gear shift. This solution is possible because of the low number of right per minute, on average, around 100 rpm. Higher regimes are not possible due to the high inertia of the moving parts. Just to mention only a few typical dimensions, the bore is from 30 to 95 cm, the height of the engine is from 5.9 m to

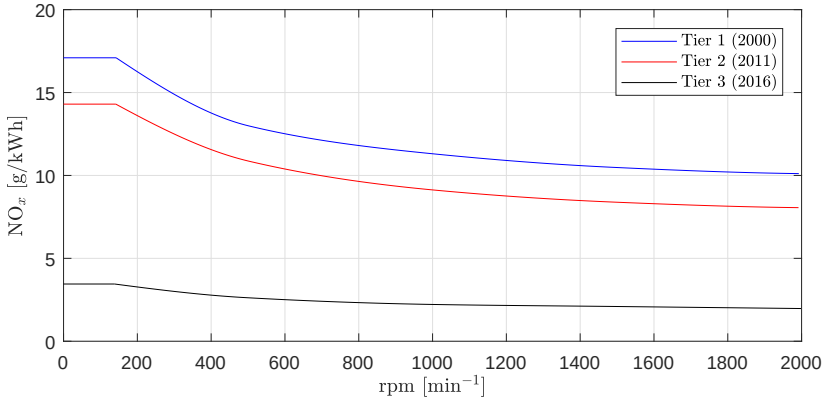

Figure 1.1: Standards on the emission of NO_x of maritime diesel engines. Data retrived from Dieselnet [3].

16 m, leading to a total power range from around 1,500 kW to 80,000 kW[1]. The quality of the fuel oil needed to run the engine (HFO, Heavy Fuel Oil) is lower than other solutions; it allows to reduce considerably the operating costs. Lastly, these engines are reliable and have a low maintenance cost compared to other solutions.

There are not many players in the market of two-strokes diesel engines for maritime application and MAN Energy Solutions is the world market leader of this sector. It is estimated that the 50% of the power needed for world trades is provided by engines from MAN Energy Solutions.

1.1 Motivation

In order to reduce the engine raw-out emission, the two-stroke engine research has been focused on the quality of the injected fuel spray. The reason is that the spray proprieties determine the break-up of the fuel jet, the quality of the air-fuel mixture and, finally, the combustion. The spray characteristics depend to a large extend on the flow inside the nozzles and the scientific community agrees on the fact that cavitation plays an important role in the disintegration of the fuel jet. This is particularly true for the slow-speed two-stroke diesel engines for maritime application where the pressure provided by the injection system is lower compared to the value from an automotive injection system. Cavitation is the adiabatic process of formation of vapour bubbles in liquid when the pressure falls below the saturation pressure at operating temperature. In injectors, it is typically due to the abrupt variation in the section area between the sac volume and the orifice holes and it is known as *hydrodynamic cavitation*.

Experts are still debating about the positive effects of cavitation since it is also respon-

[1] Data from MAN Energy Solutions catalogues

sible of enhancing mechanical wear as consequence of bubbles collapse and a lot of effort is being put on characterizing the phenomenon. Unfortunately, the experimental study of cavitation in the context of diesel injector is very complex to perform. In fact, the dimensions of the nozzle are in the millimeter range and the pressure difference is tremendously high. The visualization of the the vapour bubbles is only possible with the use of transparent nozzle made in acrylic (for instance in Polymethylmethacrylate, PMMA) but the pressures must be scaled to avoid the mechanical failure. In these experiments, even though the cavitation number, a non-dimensional parameter that describes the cavitation regime, identically replicates the operating condition, the Reynolds number could significantly differ from it. Moreover, the experimental investigation under transient conditions is even more challenging due to the short duration of the injection event. The study of transients (the opening and the closing of the fuel valve) is of importance since multiple and short duration injections are often used to cope with the emission targets. Indeed, in case of pilot injection, the transients are the dominant part of the entire process. Under these circumstances, the computational fluid dynamics (CFD) is a fundamental tool to predict the results and improve the injector design.

This project intends to investigate the cavitation in transient condition in two-stroke diesel engine injector by means of a commercial computational fluid dynamics software, *STAR CCM+*. Before going into details on the methods and results, the state of the art within this topic is briefly reported in the following section.

1.2 State of Art

In this section, the most relevant developments in the technology and design of direct injection system are introduced. In the last fifty years, a massive research has been conducted by the industry and the academia to characterize the flow inside the nozzle holes and in the first millimeters of the spray region. These studies led to some important achievements such as the introduction of a sliding fuel valve, allowing to cope with the emission regulations. Most of the researches were conducted with full lift valve, neglecting the motion of the needle; the underlying assumption was that the transients had a weak effect on the injection cycle, being only a small fraction of the entire injection cycle. This hypothesis is no more valid when pre-injections or post-injections are considered, since injectors work most of the time with partial lift and the event is extremely short. At the moment, most of the recent works are aimed at answering questions such as: what is the relationship between the needle lift and the in-nozzle flow and jet development? And between the needle lift and discharge and momentum coefficient? Despite the answers strictly depend on the geometry of the injectors, engineers and scientists are trying to demonstrate some common features and the main results are here presented.

1.2.1 Classification and design of injectors

Before starting with the description of the most popular classification of direct injectors, it is worthwhile to clarify the terminology in order to avoid misunderstandings. At this

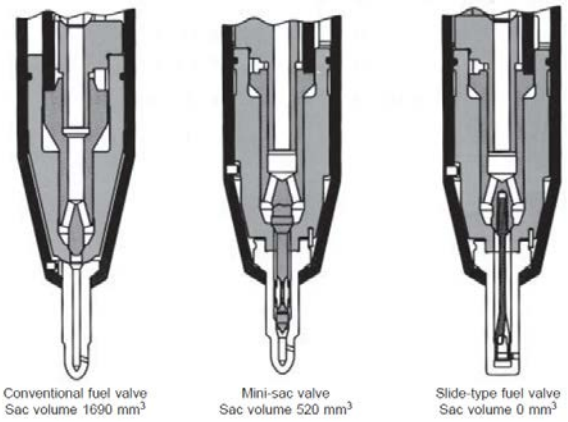

Figure 1.2: The evolution of the injector with the removal of the sac volume. Picture from Woodyard [50]

regard, the PhD thesis by Dam [18] is an excellent reference and this small vocabulary is inspired by his work. Let us start:

- The *nozzle* is the part of the injector below the seat; it includes the nozzle holes, the sac and the room for the sliding cut-off shaft.
- The *seat* is the place where the sliding cut off-shaft is in contact with the guide in the end of injection (EOI) and start of injection (SOI) events.
- The *nozzle holes* are the holes that connect the sac volume with the cylinder.
- The *sac volume* (or simply *sac*) is the volume beneath the sliding cut-off shaft; it is minimum when the shaft is in contact with the seat, it is maximum at full lift.
- The *cut-off shaft*, *needle* or *spindle* is the moving part of the injector.

Now that the reader is familiar with these terms, let us return back to the classification of diesel injectors. The direct injectors could be classified in two families based on the relative position between of the needle and the nozzle holes at the end of the injection. The families are VCO (Valve Covering Orifice) injectors and mini-SAC injectors. Both of these designs have strengths and weaknesses. Starting from the VCO injectors, the peculiar feature is that the needle covers entirely the nozzle holes at the EOI. The main advantage of this solution is that the EOI is very clean and there are not undesired leaks in the combustion chamber. This beneficial effect comes at the expense of reliability: the needle needs to be made of an high-resistance alloy in order to minimize the deformation due to the high temperatures and to avoid phenomena such as creep or thermal fatigue. Viceversa, the mini-SAC injectors are characterized by a cavity between the nozzle holes and the needle, the sac. The presence of the sac allows leakage and it increases the amount of unburned hydrocarbons, fouling and particulate emissions. On the other hand, this solution is more reliable than the previous one. Note that reliability is an important aspect in

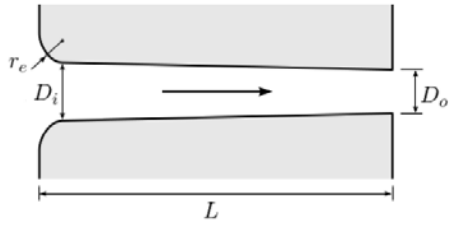

Figure 1.3: Nozzle hole with the most important geometrical dimensions: the inlet and outlet diameter (D_i and D_o), the length L and entrance radius r_e. Picture from Martí Gómez-Aldaraví [34]

engineering, but it is crucial in the marine sector, being the navigation of the large cargo ships in open ocean.

In the early 2000s, the research engineers of MAN Energy Solutions (at the time MAN Diesel & Turbo) redesigned the fuel injection valve in order to have both the advantages of the VOC and mini-SAC injectors. The improved design consists in a sliding valve that eliminates completely the sac volume and reduces the consequent waste of oil. It decreases the emissions and, at the same time, assures great reliability. Of course, because of the clearance between the inner surface of the nozzle and the other surface of the cut-off shaft and the high pressure difference between the two rooms, leakage will occur but it is minimized. Because of its large beneficial effects, this type of valve has become the standard in the engines designed and produced by MAN Energy Solutions. A representation of the mini-SAC fuel valve and the slide fuel valve is depicted in figure 1.2.

With regards to cavitation, the scientific community has studied the impact of shape of the nozzle hole on the nucleation and growth of vapor pockets. The main reference of this paragraph is the PhD thesis by Martí Gómez-Aldaraví [34], where the most relevant results are summarized. Refer to figure 1.3 for the most significant geometrical dimensions. The ratios of the parameters plotted in figure 1.3 give indications on the onset of cavitation. Let us start considering the ratio between the entrance radius r_e and the inlet diameter D_i. When r_e/D_i is large enough (Martí Gómez-Aldaraví reported the value 0.2), the pressure losses due to the sudden contraction (Borda-Carnot losses) could be neglected. As a consequence of that, it is unlikely that the pressure drops under the saturation limit. In other words, high values of r_e/D_i allow to avoid cavitation.
The ratio between the inlet and outlet diameter, D_i/D_o, is extremely relevant too; when it is larger than 1 the shape of the nozzle holes is convergent; when it is equal to 1 it is cylindrical, otherwise it is divergent. In the literature, it is popular to introduce a new variable, namely the k-factor:

$$\text{k-factor} = \frac{D_i - D_o}{10\mu\text{m}} \tag{1.1}$$

A positive k-factor (or alternatively when the ratio D_i/D_o is larger than 1) is favorable to suppress cavitation.

Lastly, the other characteristic ratio is L/D_o, where L is the length of the nozzle. An high value of L/D_o reduces the possibility of cavitation since the pressure losses due to the friction are larger. This means that, assuming that the pressure at the boundaries is constant, the pressure in the critical section is larger for a high value of the ratio L/D_o, and, ideally, above the saturation limit. Moreover, in this solution, the discharge coefficient is maximized because the location of detachment is far from the exit.

1.2.2 The Unsteady Cavitation in Literature

Cavitation in diesel engines injectors under stationary conditions has been widely investigated by the scientific community from 1959 when Bergwerk [10] published the first article related to this topic. Since then, scientists and engineers have focused both on experimental studies and numerical modeling of the in-nozzle flow and fuel spray pattern. The experiments are aimed at showing the effects of cavitation in terms of jet proprieties such as spray cone angle, penetration length or Sauter Mean Diameter (SMD). Because of the costs and limitations of setting up an experimental cavitation rig and the increase of computing power, the flow modelling through CFD software has become more and more popular in the industry and academia even though experiments are still needed to validate the codes. The technical literature on in-nozzle cavitation is very comprehensive, especially regarding the cavitation at full lift valve or at partial lift valve but always in steady condition. The reason is that the attention of the scientific community is addressed to the main injection because it is the predominant event; in fact, the transients have only a short duration. Because of the use of the pilot injection to cope with the emission limits, the transients are getting more and more relevant in these days, and they have started to be investigated. In the following paragraphs, the most relevant papers on this topic are reported in order to give the reader an overview about the main results that were achieved. Being the slide valve used mainly in the marine engineering, most of the authors referred to VCO and mini-SAC injectors, because they are used in the automotive sector. Despite of that, it is believed that the some of the results might be applied also for the injector of this project.

Among the first experimental works which take into account the transients, there is the study by Badock et al. [7]. The authors used both shadowgraph and laser sheet techniques to visualize cavitation inside a mini-SAC injector made of perspex with a cylindrical nozzle. Badock et al. observed the presence of large bubbles of gas in the sac hole at the start of the injection as a consequence of the ingestion of air at the end of injection of the previous cycle. This phenomenon was later shown using x-ray phase contrast by the Argonne National Laboratory; a nice visualization might be found in [2]. When the pressure difference of the common rail and discharge chamber is around 240 bar, Badock et al. noted a film of vapor around the walls of the nozzle holes (situation known as super-cavitation regime). The authors measured the time required to the development of the vapor film and they found that it is equal to 0.1 ms for their geometry. Moreover they noted that increasing the pressure at the inlet does not produce any significant effects on the cavitation film and they concluded that the effective area of the liquid jet is almost independent of the injection pressure when the super-cavitation is reached. Nevertheless, a liquid core was observed in all the experimental conditions.

Neroorkar et al. [37] simulated the transient needle effects in a tapered five holes mini-SAC injector. In order to simulate the motion, the authors used a method consisting in adding or removing cell layers when the cells around the needle are stretched or compressed more than an user-specified value. Unfortunately, their method requires a minimum lift; in other words, the needle and the seat never get in contact and a leak of fuel always occurs. For large duration of the injection and large amplitude of the needle motion, their simulations established a satisfactory agreement with the experimental data. Neroorkar et al. demonstrated the presence of swirling flow which affects the amount of fuel mass discharged in the cylinder. In particular, this swirling flow has a higher intensity for small needle lifts. The authors tested the code for small duration injection events too but, due to the assumption of the minimum lift, their results showed large discrepancies from the experiments.

Blessing and al. [12] studied the flow in a mini-SAC injector at different needle lift. They used a not scale close-to-reality geometry for validation and a real multi-holes mini-SAC injector; their investigation is mainly addressed to the influence of the needle lift on the spray parameters. In particular, for their geometry, the authors related the needle lift with cone spray angle and the penetration length. In addition, they studied the influence of the k-factor on the cavitation onset. They found that a divergent nozzle shows the strongest cavitation tendency. For a cylindrical nozzle, it is reported that the cavitation tendency at the center of the nozzle hole is increased during the needle opening phase. It is unclear how the authors performed their experiments and simulation; in fact it is not stated how the needle is moved in their rig and what numerical method is used in their CFD code. For this reason, it seems that they performed the tests in steady state condition.

A recent article which evaluated the influence of the needle lift in diesel injector nozzles is by Salvador et al. [19]. With the assumption that the actual transient injection process might be simplified considering the needle at different lift and steady-state, the authors performed several simulations using a multi-holes micro-SAC injector and LES turbulent model. At small lift, they noted the presence of cavitation pockets close to the needle seat; same results was also obtained by other authors as reported by Baumgartner [8]. The needle lift has a large impact on the in-nozzle flow, in terms of vorticity and turbulent structures within the holes.

Even if it does not deal with transients, the work by Payri et al. [41] is an excellent reference to understand the effect of cavitation on mass discharge, momentum flux and outlet velocity. As other authors, Payri et al. analysed the influence of the nozzle geometry (cylindrical and conical) when the needle is at maximum lift for VCO injector. The main conclusion from the authors is that cavitation appears only in cylindrical nozzle, due to the fact that the flow acceleration is more gradual in the conical nozzle. In addition, the noted that, in cavitating condition, the mass flow decreases almost linearly with the square root of the cavitation number, K. On the contrary, the momentum flux is always proportional to the pressure difference and the momentum coefficient is independent from the cavitation number. The authors showed that the outlet velocity increases in case of cavitation while, in the same conditions, the section area decreases.

The experimental investigation by Hult, Simmonk, Matlok and al. [27] is particularly relevant to this work. Indeed, it is one of the few papers in literature where the object of the study is a slide fuel valve. This typology of injector has recently become the standard for slow-speed two-stokes diesel engines and, more importantly, it is the injector that will be analysed in this project. Unfortunately, because of the practical difficulties in assessing the transients, the authors put most of their effort on characterizing cavitation in stationary condition. In other words, the experiments are conducted at fixed lift and steady conditions. Shadowgraphy in transparent nozzle made in PMMA is the technique used to visualize the cavitation pattern and PIV (Particle Image Velocimetry) is used to study the velocity in the sac and nozzle. The authors showed that cavitation appears to originate at the edge of the nozzle holes due to the high velocity gradient and at the centre of small vortex-shape structure. When the cavitation number is severely increased, the cavitation filled the outlet section entirely. The experiments were reproduced through a CFD numerical simulation and the authors found a good agreement between the two dataset in terms of discharges mass flow and velocity distribution.

1.3 The Project and its Objective

The aim of this project is to study the transient in-nozzle flow in two stroke diesel injectors, focusing on the motion of the cut-off shaft and the vapor structures which might occur in the nozzle holes and seat. The project is conducted in collaboration with MAN Energy Solutions, which provided the geometry of the injector and some data for the validation.

The project followed four major stages:

- Literature review and critical analysis of paper about in-nozzle flow for diesel engines.
- Validation of unsteady cavitation. The simulation of the periodic shedding of vapor bubbles in a converging-diverging nozzles is performed and the results are compared with the experimental data. This test allows to tune up the cavitation model and gain confidence with it.
- Validation of the overset mesh, considering the real injector system and one phase flow. The motion of the needle is implemented in the software, as well as the boundary conditions and the diesel proprieties. The results are compared with the data from an internal code of MAN Energy Solutions.
- Simulation of the multiphase flow with still and moving needle.

As far as I know, this is the first work aimed at simulating the motion of the fuel valve in a slide valve injection system through the use of the overset mesh technique. At the start of the project, the lack of know-how about the modelling of cavitation and the use of the overset forced to spend a lot of time in reading the Userguide to understand the effects of these method on the governing equations.

Chapter 2

Theory

This chapter is intended to provide the reader with the basic notions of the in-nozzle flow in diesel injectors. In the first section, after a brief introduction of cavitation theory and cavitation mechanisms which might occur in diesel injectors, the effects of the multiphase flow in the break-up of the fuel jet are discussed. The presence of vapor cavities within the nozzle of diesel injectors have both beneficial and adverse consequences which are explored in the paragraph. The next section is aimed at introducing the milestone of all the theoretical studies of in-nozzle flow: the one dimensional theory by Nurick [39]. It explains why cavitation occurs in diesel injectors and its influence on the mass and momentum flux at the outlet section. These two parameters are well describe by as many coefficients, the discharge and momentum coefficients. The application of Nurick's theory will lead to the definition of one of the most important parameter for cavitating flow: the cavitation number. With the aim of predicting the amount of fuel mass introduced in the cylinder at every injection cycle, the scientific community has put a large effort in relating the discharge coefficient with the Reynolds number and the cavitation number. Some of the main results are provided in this chapter through empirical equations and charts. Finally, the description of the entire injection system of this project is presented.

2.1 Cavitation: Definition and Application in Diesel Engines

Cavitation is the phenomenon of nucleation of vapour bubbles in liquid when the pressure falls below the saturation limit at the operating temperature. In this condition, the formation of vapor bubbles from pre-existing nucleii (generally impurities) is energetically favourable; the vapor pockets grow, interact with each others and, at the end, collapse.

At the first glance, cavitation might seem very similar to boiling: indeed, they both lead to the same phase change, from liquid to vapor. In reality, the physics behind the two processes is completely different. Consider the thermodynamic process paths depicted in

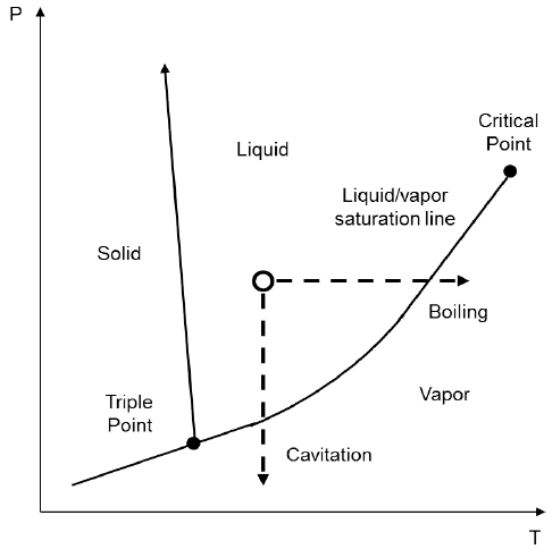

Figure 2.1: The thermodynamic process paths for boiling and cavitation in a pressure-temperature plane. Picture from Hogendoorn [26].

the pressure-temperature plane in figure 2.1. Starting from a generic point of the plane in the liquid phase, the boiling process is depicted as an horizontal straight line crossing the saturation liquid/vapor line. The change of phase is at constant pressure; in other words, it is *isobaric*. On the contrary, cavitation is illustrated as a vertical straight line crossing the saturation liquid/vapor line, meaning that the phenomenon is *isotherm*. In real conditions, heat is required for the vaporization but the variation in temperature is negligible for all the main application, including the case presented in this project[1].

In engineering and, in particular, in hydrodynamics, cavitation has been widely studied because of its negative effects on machinery. In fact, the period collapse of the vapour bubbles generates cyclic stresses on the surface in contact with the liquid. This phenomenon is known as *surface fatigue* and it is responsible for enhancing mechanical wear. This is the reason why volumetric pumps, impeller of centrifugal pumps and water turbines and propellers are designed and installed in order to avoid cavitation. In other contexts, the cavitation might be desired. Just to mention only few examples, in chemistry it is used to enhance the mixing of different species and in medicine it is used to crush kidney stones.

It has been known from almost fifty years that in-nozzle cavitation might produce positive effects in the primary break-up of the fuel jet during the injection event in diesel engines. According to Baumgartner [8], it is possible because of the energy release of the collapsing bubbles. This energy is transmitted to the surrounding fluid, increasing the turbulent

[1] This assumption is no more valid in when a cryogenic liquid are studied, for instance, in rocket engines

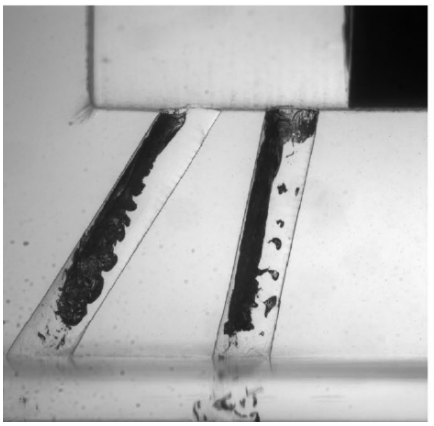

(a) Hydraulic cavitation in the nozzles, picture from Hult et al. [27]

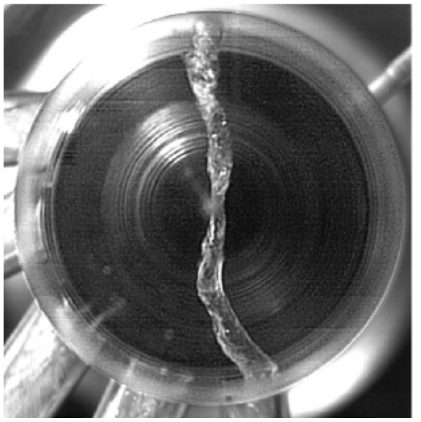

(b) String cavitation in the sac, picture from Gavaises et al. [21]

Figure 2.2: Photos of the two cavitation mechanisms in the marine diesel injectors.

kinetic energy and causing local jet break-up.
Depending on the geometrical dimension of the nozzle, cavitation could cause an increase of the spray cone angle of the fuel jet. In particular, it is likely to happen when the ratio between the length of the nozzle and the outlet diameter (L/D_o) is small enough that the vapor bubbles have only the time to nucleate but not to collapse within the nozzles. Payri and al. [41] demonstrated experimentally an increase of 15% of the cone spray angle when the most severe cavitation regime is reached in cylindrical nozzles. Same conclusions were obtained by Hiroyatsu and al. [25], who also demonstrated the decrease of the penetration length due to the bubble nucleation and growth. Another parameter that is particularly important in the context of mixture formation is the Sauter Mean Diameter (SMD). It is defined as the diameter of the sphere that has the same ratio between volume and area of the particle of interest. Cavitation allows to reduce the SMD of the droplets of the jet, minimizing the chemical delay due to the pre-combustion reactions. The main consequence of the combination of the above-mentioned effects is a better performance of the engine and, ideally, a reduction of the unburned hydrocarbons and emissions. Moreover, Baumgartner [8] reported that cavitation is not only important in the combustion reaction but also in preventing fouling, maintaining clean the injector holes.

On the other hand, cavitation might have adverse effects in diesel injectors. The multiphase flow inside the injectors causes the reduction of the discharge coefficient, C_d. The discharge coefficient is a non dimensional parameter defined as the ratio of the actual and theoretical mass flow. Payri et a. [41] demonstrated that the discharge coefficient decreases almost linearly with the square root of the cavitation number. The knowledge of the discharge coefficient is crucial in engines because it allows to know the exact amount of fuel injected in the cylinder and, therefore, the stoichimoetric air/fuel ratio. Underestimating the cavitation or, even worst, not predicting the phenomenon might have large

consequences on the performance of the machine. Lastly, cavitation could cause surface fatigue in the internal walls of the injector, reducing the operative life of the components.

Cavitation takes place in diesel injectors because of two mechanisms. They are named *hydraulic* (or *sheet*) *cavitation* and *vortex* (or *string*) *cavitation*. The hydraulic cavitation is due to the rapid motion of the fluid from the sac to the nozzle hole as a consequence of the high pressure difference. Assuming an ideal flow and the conservation of the total pressure along a streamline, the velocity increment due to the abrupt variation in section area implies a pressure drop. If the pressure falls under the saturation limit, the nucleation and growth of the vapor pockets is energetically favourable. The physics behind the second mechanism is different; the string cavitation occurs in the center of vortexes as a consequence of the pressure drops generated by the centrifugal forces. This mechanism has been discovered recently in diesel marine injectors by Gavaises and al [21]; the authors found that the vapor structures might originate from a large vortex located in the sac, as depicted in figure 2.2.

2.2 Nurick's One-Dimensional Theory

The hydraulic cavitation in diesel injector is due to the abrupt variation in the section area from the sac volume to the nozzle hole. In order to explain this statement, let us assume an inviscid, incompressible, one-dimensional flow and apply the Bernoulli equation. At this point, it is useful to refer to the figure 2.3 for the meaning of the subscripts used in the equations of this section.

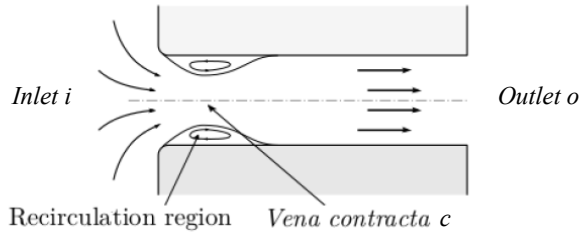

Figure 2.3: A simplified representation of a two-dimensional nozzle. Three significant locations are indicated with the letters i, c and o, respectively at the inlet, vena contracta and outlet. Picture from Martí Gómez-Aldaraví [34].

From the Bernoulli equation, with the assumption of still fluid in the inlet and neglecting the gravitational effect (very low in the context of diesel injectors, because of their dimension and shape):

$$p_i = p_c + \frac{\rho}{2} u_c^2 \tag{2.1}$$

Recalling the incompressability assumption, from continuity:

$$u_c A_c = u_i A_i \tag{2.2}$$

It is useful to define some non-dimensional parameters. The first one is the contraction coefficient C_a. It is defined as the ratio between the effective section area and the actual section area. When it is evaluated in the point c of the picture 2.3 (vena contracta) and the nozzle is cylindrical:

$$C_a = \frac{\text{Effective area}}{\text{Actual area}} = \frac{A_c}{A_o} = \frac{A_c}{A_i} \tag{2.3}$$

The second parameter is the velocity coefficient, C_v. It is equal to the ratio between the effective velocity and the theoretical velocity at the outlet. It accounts the losses due to the friction, turbulence and the sudden variation in section area (Borda-Carnot losses). In symbols:

$$C_v = \frac{\text{Effective velocity}}{\text{Theoretical velocity}} = \frac{u_o}{\sqrt{\frac{2(p_i - p_o)}{\rho}}} \tag{2.4}$$

The last coefficient could be calculated from the previous two and it is named discharge coefficient, C_d. The discharge coefficient is equal to the ratio between the effective and theoretical mass flow. When the contraction coefficient (C_a) is referred to the outlet section, it is equal to:

$$C_d = \frac{\text{Actual mass flux}}{\text{Theoretical mass flux}} = C_v C_a \tag{2.5}$$

Having introduced these parameters, inserting the above mentioned coefficients in the Bernoulli equation (2.1), the following relation could be obtained:

$$\frac{p_i - p_c}{p_i - p_o} = \left(\frac{C_v}{C_a}\right)^2 \tag{2.6}$$

The condition for the incipient cavitation is that $p_c = p_{sat}$. Updating eq. (2.6):

$$\frac{p_i - p_{sat}}{p_i - p_o} = \left(\frac{C_v}{C_a}\right)^2 \tag{2.7}$$

In literature, the left hand side of the eq. (2.7) is known as cavitation number:

$$\mathrm{K} = \frac{p_i - p_{sat}}{p_i - p_o} \approx \frac{p_i}{p_i - p_o} \tag{2.8}$$

where the last expression in the right hand side of eq. (2.8) is a good approximation when the saturation pressure is much less than the inlet and outlet pressure. In the context of diesel injectors, this is always true. In fact, the saturation pressure of the diesel fuel has a magnitude of 1 kPa, while the injection and cylinder pressures have a magnitude of 10^4 kPa.

In literature, it is possible to meet some other definitions of the cavitation number. For instance, the following in eq. (2.9) is very popular:

$$\mathrm{CN} = \frac{p_i - p_o}{p_o - p_{sat}} \approx \frac{p_i - p_o}{p_o} \tag{2.9}$$

In context different from diesel injectors, for instance when cavitation is studied around hydrofoils or other geometries, the formulation in eq. (2.10) is used:

$$\sigma = \frac{p_i - p_{sat}}{\frac{1}{2}\rho u_c^2} \tag{2.10}$$

In this work, it will be explicitly stated which definition is used (K, CN or σ) when the cavitation number is mentioned.

2.3 Cavitation Regimes

Regardless of the definition of cavitation number which might be used, this non dimensional parameter is fundamental to predict amount of vapor due to the hydrodynamic cavitation. In literature, two regimes are of importance: they are named *onset of cavitation* and *supercavitation*.

At this point, it is useful to refer to the article by von Kuensberg Sanne [48] to show the different situations which might be present in the one dimensional nozzle hole of a diesel injector. The picture 2.4, which is inspired by von Kuensberg Sannes's work, presents four situations: a simple turbulent flow (a), the onset of cavitation (b), supercavitation (c) and hydraulic flip (d). The focus is addressed to the pressure distribution along the length of the nozzle.

Let us start describing the first case, the simple turbulent flow. In this situation, the separation of the boundary layer occurs due to the abrupt variation in the section area. Since the streamlines can not follow the sharp angle of the nozzle inlet, the diameter of the stream reaches its minimum, meaning that a vena contracta forms. From the figure 2.4 (a), it is possible to observe that the flow reattaches in r (rettachment point) and, from this point, the boundary layer starts developing again. At the exit, the flow is not fully developed since at least 10 diameters [16] (some authors use the conservative length of 40 diameters [38]) are needed to reach this condition. From the point indicated with the number 1 in figure 2.4, the pressure decreases but it still remains above the saturation value. The lowest pressure is reached in the vena contracta c, because of the Borda-Carnot losses:

$$\Delta p = \xi \frac{1}{2}\rho(u_r - u_1)^2 \tag{2.11}$$

where ξ is an empirical loss coefficient which only depend on the geometry of the injector. From point c to r, the fluid reattaches to the wall of the nozzle, meaning that the section area increases, the velocity decreases and the flow expands. Lastly, from r to 2 the pressure drop is mainly due to the friction losses; using the Darcy-Weisbach equation:

$$\Delta p = \frac{1}{2} F \frac{(L - L_r)}{D} u_r^2 \tag{2.12}$$

where the friction coefficient, F, might be recursively calculated for turbulent flow thought the Colebrook's equation:

$$\frac{1}{\sqrt{F}} = -2\log\left(\frac{\epsilon}{3.7D} + \frac{2.51}{\mathrm{Re}\sqrt{F}}\right) \tag{2.13}$$

where the ratio ϵ/D is the relative roughness.

The flow in the figure 2.4 (b) is known as onset of cavitation. In this situation, the pressure reaches the saturation value in the vena contracta, allowing the growth of the vapor pockets. Again, from point c to r, the fluid expands and reattaches to the walls. A new boundary layer starts to develop from point r. The main losses from the reattachment point to the exit are due to the wall friction.

In the situation described in figure 2.4 (c), the cavitation region reaches the nozzle exit leading to a supercavitation regime. Again, the saturation pressure is reached in the vena contracta, due to the pressure loss caused by the sudden contraction of the section area. From point c to 2, the pressure increases. This situation might be explained considering that the inlet and outlet pressures are fixed boundary condition.

Finally, in the picture 2.4 (d), the hydraulic flip is depicted. In this situation the pressure at the point located in the vena contracta, c, is equal to the pressure in the point 2 but higher than the saturation pressure. Von Kuensberg Sarre reported that the flow at the exit is "*smooth, glass-like without any visible disturbance*". In the hydraulic flip, the discharge coefficient, C_d, reaches its minimum. The scientific community agrees that, in diesel injectors, the hydraulic flip is unlikely to occur.

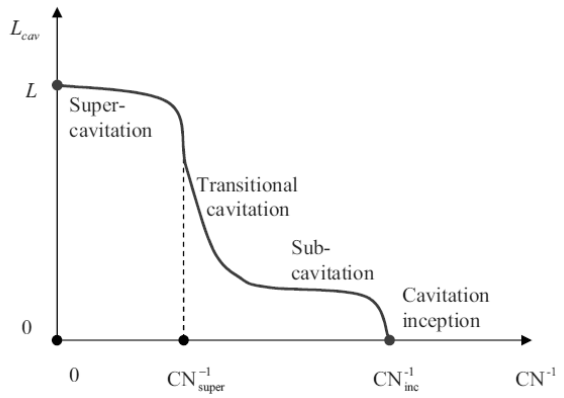

Figure 2.5: The cavitation regimes as a function of the inverse of the cavitation number, CN^{-1}. Picture from Martynov [33]

In order to predict the cavitation regime from the pressure condition at the inlet and outlet of the nozzle, the authors Sato and Saito [44] proposed the map reported in figure 2.5. The inverse of the cavitation number, CN^{-1}, is related with the length of the cavitating region, L_{cav}. Note that, in addition to the cavitation regimes described in the previous paragraph, the authors introduced also the *subcavitation* and *transitional* cavitation stages. In the subcavitation stage, the length of the cavitation zone is almost constant, meaning that it is not

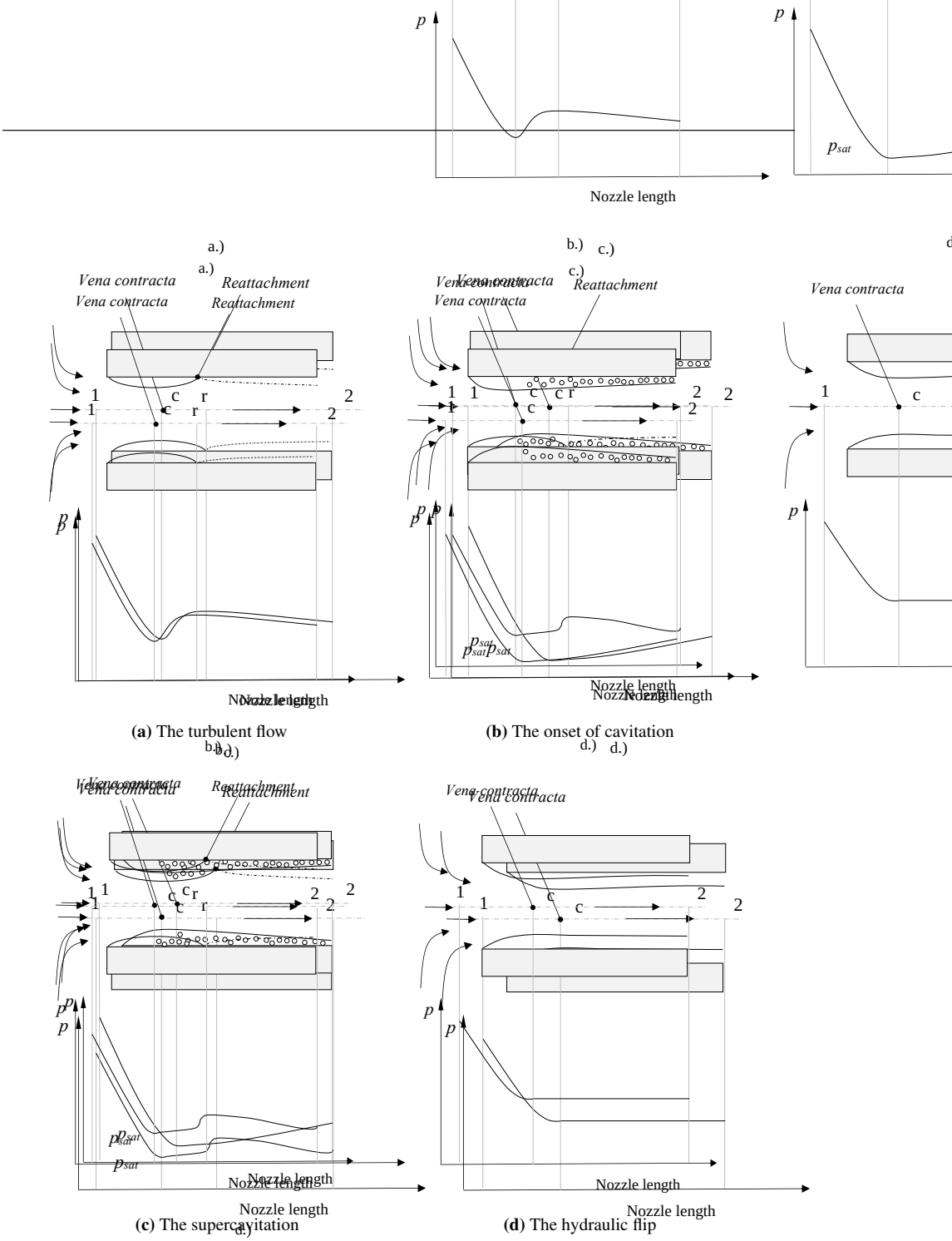

(a) The turbulent flow **(b)** The onset of cavitation

(c) The supercavitation **(d)** The hydraulic flip

Figure 2.4: The four regimes inside a sharp edge nozzle and the pressure distribution along the length of the nozzle. Picture inspired by von Kuensberg Sarre [48].

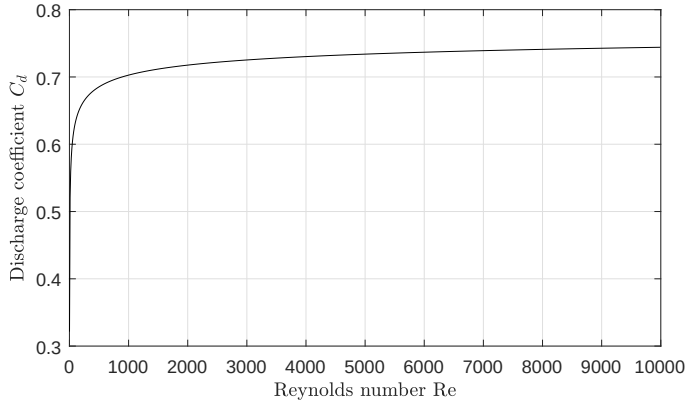

Figure 2.6: The discharge coefficient versus the Reynolds number in case of non-cavitating flow, according to the empirical equation by Hall for $L/D_o = 5$ (a typical value).

dependant on small variation of the inverse of the cavitation number. Decreasing further the inverse of CN, the transitional stage is reached. From this situation, a small increment of the cavitation number might lead to the supercavitation regime.

The scientific community has worked to determine empirical correlations between the cavitation number and the the discharge coefficient too. In a non cavitating flow, the discharge coefficient is only dependant on the Reynolds number and the geometry of the nozzle. In particular, in case of laminar flow, the relationship between C_d and Re is almost linear while it is very weak in case of turbulent flow. At this regard, refer to figure 2.6 where the function proposed by Hall and reported in eq. (2.14) has been plotted versus the Reynolds number for $L/D_o = 5$ (a typical value for diesel injectors).

$$C_d = 1 - 0.184\frac{(L/D_o + 1.11\mathrm{Re}^{0.25} - 1)^{0.8}}{\mathrm{Re}^{0.2}} \tag{2.14}$$

For cavitating flow, when that the cavitation number K is less than the critical value, the discharge coefficient decreases almost linearly with the square root of K, as predicted by Nurick [39]. In symbols:

$$C_d \propto \sqrt{K} \tag{2.15}$$

2.4 Bubble dynamics

The first model of the dynamics of a bubble in an infinite domain of fluid is by Rayleigh in 1917 [32], and it was applied for the first time in a cavitation problem by Plesset in 1949 [42]. The model, which is named Rayleigh-Plesset because of its authors, is based on the assumptions that the bubble is submerged in a Newtonian and incompressible fluid and that there is negligible mass exchange at the interface. The equation that is going to be

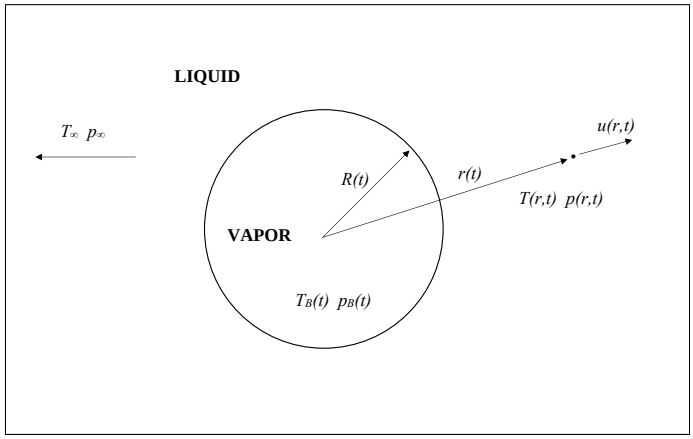

Figure 2.7: A spherical bubble of radius $R(t)$ immersed in a liquid. Picture inspired by Brenner's work [14].

derived in the following section describes the radial motion of a bubble in an incompressible fluid when there is only a singular spherical bubble in an infinite domain of liquid. This approach, which could seem very theoretical at the first glance, allows to identify the most important parameters in the physics of the process. The derivation here presented is based on the work of Brenner [14], at which this author suggests to refer to in case of a more exhaustive explanation.

Let us consider a bubble of radius $R(t)$ with an internal pressure $p_B(t)$ and temperature $T_B(t)$, as indicated in figure 2.7. This bubble is submerged in a liquid having a constant density, ρ_L, and dynamic viscosity, μ_L. The pressure and temperature infinitely far from the bubble are equal to p_∞ and T_∞. With the variable r, it is intended the distance from the center of the spherical bubble to an arbitrary point in the liquid, as indicated in the figure 2.7. The radial velocity of the liquid in this point and in an arbitrary time t is $u(r,t)$. It is fair to assume that the velocity $u(r,t)$ follows an inverse square law:

$$u(r,t) = \frac{F(t)}{r^2} \tag{2.16}$$

where $F(t)$ is a generic function of time.

In order to derive the function $F(t)$, let us consider a point of the bubble interface, where $r = R$. Here, the radial velocity $u(R,t)$ must correspond to the growth velocity of the bubble because of the aforementioned assumption of no mass transport across the interface:

$$u(R,t) = \frac{\mathrm{d}R(t)}{\mathrm{d}t} \tag{2.17}$$

Therefore, inserting eq. (2.17) in eq. (2.16), the following expression for $F(t)$ could be derived:

$$F(t) = R^2(t)\frac{\mathrm{d}R(t)}{\mathrm{d}t} \tag{2.18}$$

In general, the zero mass transport across the interface between the vapor and the liquid is a good approximation for all the main engineering approximation. To show this statement, let us calculate the complete expression for the function $F(t)$. It could be derived considering that the mass rate of evaporation ($\dot{m}_E$) must be equal to the mass flow of liquid inward respect to the interface ($\dot{m}_L$). The mass rate of evaporation, $\dot{m}_E$, could be calculated multiplying the production of vapour by its density:

$$\dot{m}_E = \rho_V \frac{\mathrm{d}}{\mathrm{d}t}\left(\frac{4}{3}R^3(t)\pi\right) = 4\rho_V \pi R^2(t)\frac{\mathrm{d}R(t)}{\mathrm{d}t} \tag{2.19}$$

The mass flow of liquid inward relative to the interface is:

$$\dot{m}_L = 4\rho_L \pi R^2(t) u_L(t) \tag{2.20}$$

where $u_L(t)$ is the velocity of the liquid phase at the interface.

Because of mass conservation, eq. (2.19) and eq. (2.20) must be equivalent. Thus, it is possible to express the liquid velocity at the interface as follows:

$$u_L = \frac{\rho_V}{\rho_L}\frac{\mathrm{d}R}{\mathrm{d}t} \tag{2.21}$$

The velocity $u(R,t)$ must be updated removing the inward component of velocity:

$$u(R,t) = \frac{\mathrm{d}R}{\mathrm{d}t} - u_L = \frac{\mathrm{d}R}{\mathrm{d}t}\left(1 - \frac{\rho_V}{\rho_L}\right) \tag{2.22}$$

The expression for the function $F(t)$ could be derived inserting eq. (2.22) in eq. (2.16):

$$F(t) = \left(1 - \frac{\rho_V}{\rho_L}\right) R^2(t)\frac{\mathrm{d}R(t)}{\mathrm{d}t} \approx R^2(t)\frac{\mathrm{d}R(t)}{\mathrm{d}t} \tag{2.23}$$

The last approximation is justified by the fact that the density of vapor is much lower than the density of the liquid for diesel fuel.

Returning back to the radial velocity of the bubble, it has been shown that, with a good approximation:

$$u(t) = \left(\frac{R(t)}{r(t)}\right)^2 \frac{\mathrm{d}R}{\mathrm{d}t} \tag{2.24}$$

This expression (eq.(2.24)) is going to be used in the Navier-Stokes equation in spherical coordinate:

$$\rho_L\left(\frac{\partial u}{\partial t} + u\frac{\partial u}{\partial r}\right) = -\frac{\partial p}{\partial r} + \mu_L\left[\frac{1}{r^2}\frac{\partial}{\partial r}\left(r^2\frac{\partial u}{\partial r}\right) - 2\frac{u}{r^2}\right] \tag{2.25}$$

Dividing the expression by the liquid density, ρ_L, and re-ordering the terms:

$$-\frac{1}{\rho_L}\frac{\partial p}{\partial r} = \frac{\partial u}{\partial t} + u\frac{\partial u}{\partial r} - \nu_L\left[\frac{1}{r^2}\frac{\partial}{\partial r}\left(r^2\frac{\partial u}{\partial r}\right) - 2\frac{u}{r^2}\right] \tag{2.26}$$

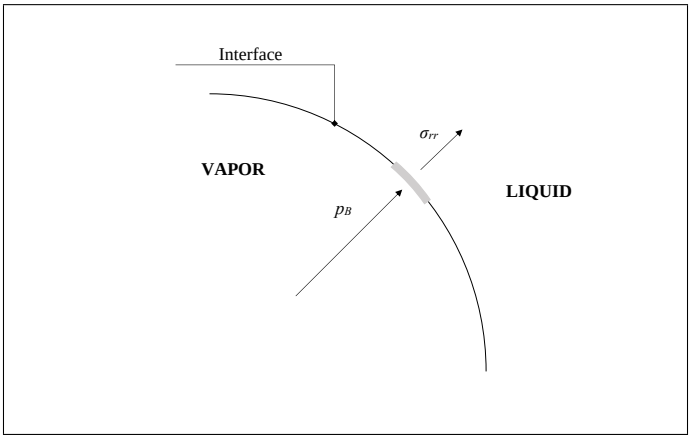

Figure 2.8: The forces per unit of area acting on a portion of the interface. Picture inspired by Brenner's work [14].

Introducing the eq. (2.24) in eq. (2.26) above, and integrating:

$$\frac{p(R) - p_\infty}{\rho_L} = R(t)\frac{\mathrm{d}^2 R(t)}{\mathrm{d}t^2} + \frac{3}{2}\frac{\mathrm{d}R(t)}{\mathrm{d}t} \tag{2.27}$$

The last step consists in determine an expression for the pressure at the interface, $p(R)$. For this purpose, let us consider the infinite thin lamina containing a portion of the interface, as depicted in figure 2.8. The force per unit of area pointing outward the lamina, σ_{rr}, in spherical coordinate, is equal to:

$$\sigma_{rr} = -p(R) + 2\mu_L \left.\frac{\partial u}{\partial r}\right|_{r=R} \tag{2.28}$$

Therefore, the net force per unit of area acting on the lamina is:

$$\sigma_{rr} + p_B - 2\frac{\gamma}{R} = -p(R) - 4\frac{\mu_L}{R}\frac{\mathrm{d}R}{\mathrm{d}t} + p_B - 2\frac{\gamma}{R} \tag{2.29}$$

where σ_{rr} is replaced by the expression in eq. (2.28), the derivative $\frac{\partial u}{\partial r}|_{r=R}$ is calculated from eq. (2.24) and γ is the surface tension.
With the assumption of zero mass transfer through the interface, this force per unit of area must be equal to zero. This leads to the following expression for the pressure $p(R)$:

$$p(R) = p_B - 4\frac{\mu_L}{R}\frac{\mathrm{d}R}{\mathrm{d}t} - 2\frac{\gamma}{R} \tag{2.30}$$

Inserting eq. (2.30) in eq. (2.27), the final expression, known as Rayleigh-Plesset equation, is obtained:

$$\frac{p_B(t) - p_\infty(t)}{\rho_L} = R(t)\frac{\mathrm{d}^2 R}{\mathrm{d}t^2} + \frac{3}{2}\frac{\mathrm{d}R^2}{\mathrm{d}t} + 4\frac{\nu_L}{R}\frac{\mathrm{d}R}{\mathrm{d}t} + \frac{2\gamma}{\rho_L R(t)} \tag{2.31}$$

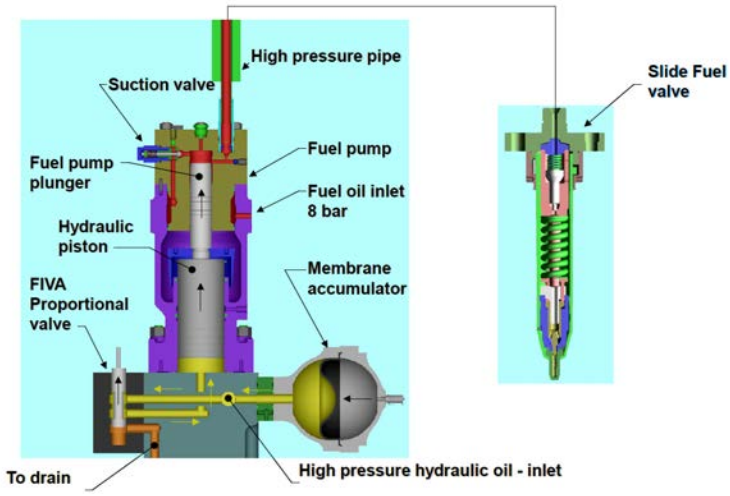

Figure 2.9: Scheme of the fuel injection system of a two-stroke diesel engine. Picture provided by MAN Energy Solutions

2.5 The Fuel Injection System

In the project, the fuel injection system depicted in figure 2.9 is analysed. This system is installed in ME-B and ME-C two-stoke slow-speed diesel engines designed by MAN Energy Solutions and it is completely controlled by electronics. It is characterized by an high level of flexibility since it allows to control, and possibly adjust, the fuel injection in each cylinder of the engine independently.

The system works with two fluids: hydraulic oil (colored in yellow in the picture), and fuel oil (in red). Hydraulic oil and fuel are separated by an hydraulic piston sealed with a fuel pump plunger. The injection process starts from the pressurized hydraulic oil stored in a membrane accumulator. This device, which is made of a membrane that separates the hydraulic oil from a gas (typically nitrogen) is aimed at delivering the pressurized oil to hydraulic piston through piping. This is only possible when the FIVA (Fuel Injection Valve Activation) proportional valve allows the hydraulic oil flow.

The FIVA valve is an electromagnetic component that controls both the injection of the fuel in the combustion chamber and the opening and closing of the exhaust valve. A scheme of the FIVA proportional valve is depicted in figure 2.10. The motion of the main spool of the FIVA valve is controlled by the Cylinder Control Unit (CCU), which processes the data coming from position feedback sensor. Eventually, the main spool is moved by a solenoid actuator and the valve geometry allows the flow of the hydraulic oil in pipes. In this way, the hydraulic oil reaches the piston that now can move upwards.

This piston is sealed with the fuel pump plunger; this component moves in a chamber filled with fuel. The quiescent fuel in the time span of the two consecutive injection is at

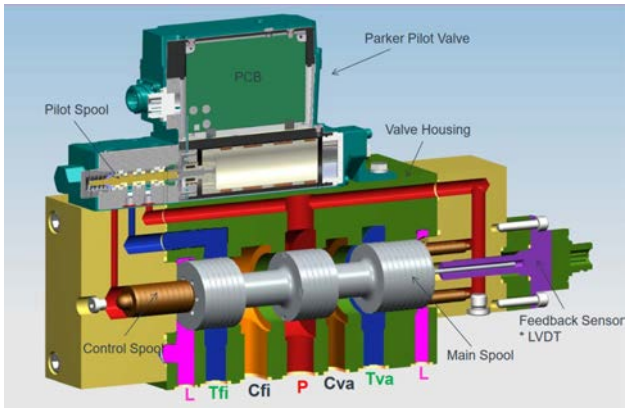

Figure 2.10: Scheme of the FIVA valve. Picture from [1]

8 bar of pressure and it is supplied by the suction valve depicted in figure 2.9. The ratio between the radial dimension of the hydraulic piston and fuel plunger plays a fundamental role in the fuel compression. In fact, because of the third Newton's law, the forces acting on the heads of the piston and plunger must be equal in absolute value. This means that, under the assumption of the Pascal's principle, the following relation among areas and pressures could be derived:

$$p_o A_o = p_f A_f \tag{2.32}$$

where the subscribes o and f refer to the hydraulic oil side and fuel side respectively.
In other words, the ratio between the area of the piston heads is equal to the pressure ratio of fuel and oil. In the injection system of this project, the radius of the piston in the fuel side is half of the radius in the hydraulic oil side; this means that the pressure ratio is around 4.

The pressurized fuel flows through the high pressure pipe, only when the springs in the fuel valve have opened. The springs in the fuel valve react to the pressure given by the booster pump and they eventually open, allowing the start of the injection. The piping connects the Hydraulic Cylinder Unit (HCU) (booster pump, FIVA and the exhaust valve actuator) with the fuel valve; its length is approximately equal to 1.9 m.

As the fuel increases its pressure, it flow through a non-return valve and feeds down the body of the injector. In fact, in this component, there are compressed springs that divide the internal volumes in chambers. These springs only open when the force generated by pressure of the fluid overcomes the elastic force. For the design used in the project (installed in the MAN 4T50ME-X test engine), the threshold value is around 370 bar. When the pressure reaches this value, the spindle starts to move upwards and the fuel flows in the seat, increasing the lift. The geometry of the spindle is quite complex, since it is expressly designed to fulfill the IMO standards. The details are presented in the *Validation cases* section.

Chapter 3

Model and implementation

The aim of this chapter is to present and comment the main models and solvers of this Master thesis. The simulations are run in *STAR CCM+*, which is one of the most popular sofware for CFD; it was developed by CD-Adepco and, nowadays, it is owned by Siemens. *STAR CCM+*, which stands for Simulation of Turbulent flow in Arbitrary Region - Computational Continuum Mechanics, uses the finite volume method to solve the conservation equations in unstructured meshes. This presentation, after a brief discussion of the governing equations, follows the workflow presented in the software when a new simulation is launched.

3.1 The governing equations

In fluid mechanics, the governing equations are based on the mass and momentum conservation. The derivation of the governing equations is here omitted but the reader could refer to any books about fundamentals of fluid mechanics; good references are Kundu et al. [31] and Perić et al. [20]. The derivation is based on Reynolds' transport theorem, which establishes the link between a the control mass system (CM) and the control volume system (CV). Let us be ϕ any intensive propriety:

$$\frac{\mathrm{d}}{\mathrm{d}t}\int_{\Omega_{CM}} \rho\phi \,\mathrm{d}\Omega = \frac{\mathrm{d}}{\mathrm{d}t}\int_{\Omega_{CV}} \rho\phi \,\mathrm{d}\Omega + \int_{S_{CV}} \rho\phi(\boldsymbol{u}-\boldsymbol{u_b})\cdot\boldsymbol{n}\,\mathrm{d}S \tag{3.1}$$

where Ω_{CM} is the volume occupied by the control mass system, Ω_{CV} and S_{CV} are the volume of the control volume system and its surface, $\boldsymbol{n}$ is the outpointing normal vector, $\boldsymbol{u}$ is the velocity of the fluid and $\boldsymbol{u_b}$ is the velocity of the control volume.

The popular integral form of the mass conservation could be calculated for $\phi = 1$, when $\boldsymbol{u_b} = 0$:

$$\frac{\partial}{\partial t}\int_{\Omega} \rho \,\mathrm{d}\Omega + \int_{S} \rho\boldsymbol{u}\cdot\boldsymbol{n}\,\mathrm{d}S = 0 \tag{3.2}$$

Through the use of the Gauss' theorem and with the assumption that the control volume is infinitely small, the differential form of the continuity equation might be derived:

$$\frac{\partial \rho}{\partial t} + \nabla \cdot (\rho \boldsymbol{u}) = 0 \tag{3.3}$$

The momentum conservation is derived from the Newton's second law and using the Reynolds' transport theorem. In general, with the aim of counting the surface stresses on the control volume, the assumption of Newtonian fluid is made and the following integral expression is obtained:

$$\frac{\partial}{\partial t} \int_{\Omega} \rho \boldsymbol{u} \, \mathrm{d}\Omega + \int_{S} \rho \boldsymbol{u} \boldsymbol{u} \cdot \boldsymbol{n} \, \mathrm{d}S = \int_{S} \mathcal{T} \cdot \boldsymbol{n} \mathrm{d}S + \int_{\Omega} \rho \boldsymbol{b} \mathrm{d}\Omega \tag{3.4}$$

where $\boldsymbol{b}$ is the vector of the body forces and $\mathcal{T}$ is the stress tensor. In case of Newtonian fluid, it is defined:

$$\mathcal{T} = -\left(p + \frac{2}{3}\mu \nabla \cdot \boldsymbol{u}\right) \mathcal{I} + 2\mu \left(\frac{1}{2}\left[\nabla \boldsymbol{u} + (\nabla \boldsymbol{u})^T\right]\right) \tag{3.5}$$

and $\mathcal{I}$ is the identity tensor.
The differential form of the momentum conservation could be obtained applying the Gauss' theorem to the convective and diffusive terms of eq. (3.4):

$$\frac{\partial (\rho \boldsymbol{u})}{\partial t} + \nabla \cdot (\rho \boldsymbol{u} \boldsymbol{u}) = \nabla \cdot \mathcal{T} + \rho \boldsymbol{b} \tag{3.6}$$

Using the Cartesian coordinates and with the assumption that the gravity is the only body force, eq. (3.6) could be written in index (Einstain) notation, as follows:

$$\frac{\partial (\rho u_i)}{\partial t} + \frac{\partial (\rho u_i u_j)}{\partial x_j} = \frac{\partial \tau_{ij}}{\partial x_j} - \frac{\partial p}{\partial x_j} + \rho g_i \tag{3.7}$$

The eqs. (3.3) and (3.4) are discretized using the Finite Volume Method. This method consists in dividing the entire domain in smaller control volumes through a suitable grid (or mesh); the computational node is usually located in the centroid of the cell. A generic conservation equation must be valid not only for the entire volume but also for the small control volumes. Let us consider a generic control volume in three dimensions. The net flux through the surface of the cell is equal to the sum of the fluxes through each of its face:

$$\int_{S} f \, \mathrm{d}S = \sum_{S} \int_{S_k} f \, \mathrm{d}S \tag{3.8}$$

where f might be the component of the convective of diffusive flux normal to the reference face. Unfortunatley, the value of f on the surface S_k is unknown being the information available only in the centroid of the control volume. For this reason, the approximation of f in the face is necessary and several methods are studied in literature. In this project, both the convective and diffusive component of the flux vector in the normal direction is approximated using a second-order scheme.

As regards the integration of the terms over a volume, the simplest second-order accurate approximation consists in multiplying the mean value of the function by the volume of the cells; in symbols:

$$\int_{\Omega} q \, \mathrm{d}\Omega = \overline{q}\Delta\Omega \approx q_P \Delta\Omega \tag{3.9}$$

where q is a generic function and q_P is the value of the function at the center of the cell. Here, the information is available and no interpolation is needed. Again, being out of the scope of this project to present in detail the Finite Volume Method and the implementation of the equation in a CFD code, this authors suggests to refer to Perić et al. [20] or the lecture notes by Bingham et al. [11].

3.2 The Segregated Flow Solver

The software *STAR CCM+* offers two possibilities to solve the conservation equations presented in the previous section. They are named *Segregated flow solver* and *Coupled flow solver*. As their names suggest, they approach the problem in different manners. The *Segregated flow solver* solves for the velocity components (u, v, w) and the pressure (p) in a sequential manner; on the contrary, in the *Coupled flow solver*, the continuity and momentum equations are solved simultaneously. Since the software only permits to use the *Volume of Fraction (VOF)* method with the *Segregated flow solver*, in this paragraph the emphasis is focused on this method. In case of interests, the author suggests to refer to the User Guide of *STAR CCM+* [45].

The *Segregated flow solver* uses a predictor-corrector approach to couple the pressure and velocity to fulfill the continuity and momentum equations. The user of *STAR CCM+* can choose among two algorithms: SIMPLE (Semi-Implicit Method for Pressure Linked Equations) and PISO (Pressure-Implicit with Splitting of Operators). The SIMPLE algorithm is the one used in the simulations since it is the only one compatible with the *VOF* approach.

A brief presentation of the SIMPLE algorithm is here introduced. Solving the discretized continuity and Navier-Stokes equations for the three components of velocity and pressure is complex. The main reason is the lack of an independent equation for the pressure; in fact, only the pressure gradient (and not the pressure function) appears in the momentum equations. Moreover, the continuity equation is more a kinematic restriction rather than a dynamic equation. In the years, as reported by Perić [20], in order to overcome this issue, the most popular approaches consist in formulating the pressure field in order to fulfill mass conservation. Under these circumstances, the SIMPLE algorithm was formulated in early 1970s by Spalding and Patankar [40]. The discussion presented is inspired from the OpenFOAM blog [4]. Let us assume a steady, incompressible and laminar flow. The conservation equations in vector form are:

$$\nabla \cdot \boldsymbol{u} = 0 \tag{3.10}$$

$$\boldsymbol{u} \cdot \nabla \boldsymbol{u} - \nabla \cdot \nu \nabla \boldsymbol{u} = -\nabla p \tag{3.11}$$

where, in this context, p is the kinematic pressure (p/ρ).

The discretized momentum equation (using, for instance, the Finite Volume Method) could be expressed as follows:

$$\mathcal{M}\boldsymbol{u} = -\nabla p \tag{3.12}$$

where $\mathcal{M}$ is a matrix having constant entries whose values only depend on the decomposing method. It is clear that $\mathcal{M}$ has a dimension equal to the number of cells in the mesh. To recap, only the coefficients M_{ij} are known in equation (3.12).
The matrix $\mathcal{M}$ could now be decomposed in a diagonal matrix, $\mathcal{A}$ and in a off-diagonal matrix, $\mathcal{H}$, so that:

$$\mathcal{A}\boldsymbol{u} - \mathcal{H} = -\nabla p \tag{3.13}$$

This operation is aimed at obtaining a matrix which is easy to invert, $\mathcal{A}$.
$\mathcal{H}$ could be easily calculated as:

$$\mathcal{H} = \mathcal{M}\boldsymbol{u} - \mathcal{A}\boldsymbol{u} \tag{3.14}$$

Rearranging equation (3.13), the velocity is now:

$$\boldsymbol{u} = \mathcal{A}^{-1}\mathcal{H} - \mathcal{A}^{-1}\nabla p \tag{3.15}$$

Substituting the equation (3.15) in the continuity equation:

$$\nabla \cdot (\mathcal{A}^{-1}\mathcal{H} - \mathcal{A}^{-1}\nabla p) = 0 \tag{3.16}$$

and, finally, the Poisson equation for pressure is obtained:

$$\nabla \cdot (\mathcal{A}^{-1}\nabla p) = \nabla \cdot (\mathcal{A}^{-1}\mathcal{H}) \tag{3.17}$$

Now that the equations (3.12) and (3.17) are obtained, the SIMPLE algorithm follows the procedure here described:

1. The value for the pressure gradient is initialised.
2. The momentum equation (3.12) is solved for the velocity field. In general, the velocity field will not fulfill the mass conservation.
3. The Poisson equation (3.17) is solved for the pressure field.
4. The velocity field is corrected through equation (3.15).
5. Now the continuity equation is satisfied but the momentum equation is not fulfilled anymore. The new loop starts for point 2 until a threshold value for the error in the conservation equations is reached.

In case of turbulent flow, additional equations must be fulfilled in the loop. For instance, using URANS and $k-\omega$ turbulent model, the equation for the turbulent kinetic energy and the specific rate of dissipation are:

$$\mathcal{M}_k k = S_k \quad \text{and} \quad \mathcal{M}_\omega \omega = S_\omega \tag{3.18}$$

This is a brief simplified description since it neglects for instance the under-relaxation factors. It is out of the scope of this work to describe in depth the algorithm; again refer to Perić [20] to a more exhaustive discussion.

3.3 The Volume of Fluid (VOF) Method

The *Volume of Fluid (VOF)* is a popular numerical method used to simulate immiscible flow. It is a multiphase model and it requires an Eulerian framework. Its main assumption is that the interface proprieties could be derived as function of the volume fraction of the phases in the domain. Referring to a control volume, the volume fraction of the phase i is defined as:

$$\alpha_i = \frac{V_i}{V} \tag{3.19}$$

where V_i is the volume occupied by the phase i in the cell and V is the total volume of the cell.
It is clear that the sum of all the phases in the same cell must be equal to 1; in symbols:

$$\sum_i^N \alpha_i = 1 \tag{3.20}$$

where, in this context, N is total number of phases.

Once that the volume fraction of the different phases are known in the same cell, the physical propriety of the mixture could be calculated. The method is reported for the density:

$$\rho = \sum_i \alpha_i \rho_i \tag{3.21}$$

and dynamic viscosity:

$$\mu = \sum_i \alpha_i \mu_i \tag{3.22}$$

The introduction of the volume fraction requires an additional equation in order to obtain a close problem. At this point, neglecting the Reynolds stresses that will be treated in the *Turbulent Model* paragraph and considering two phases (liquid and vapour for instance), the number of unknown is 5 (three components of the velocity vector, the pressure and the volume fraction), while the number of equation is 4 (continuity equation and the three momentum equations). The additional equation, the phase mass conservation, is here reported:

$$\frac{\partial}{\partial t}\int_\Omega \alpha_i \,\mathrm{d}\Omega + \oint_{S_i} \alpha_i \boldsymbol{u}\cdot\boldsymbol{n}\,\mathrm{d}S = \int_\Omega \left(S_{\alpha_i} - \frac{\alpha_i}{\rho_i}\frac{\mathrm{D}\rho_i}{\mathrm{D}t}\right)\,\mathrm{d}\Omega - \int_\Omega \frac{1}{\rho_i}\nabla\cdot(\alpha_i\rho_i\boldsymbol{u}_{d,i})\,\mathrm{d}\Omega \tag{3.23}$$

where $\boldsymbol{u}$ is the mixture (mass-averaged) velocity, $\boldsymbol{u}_{d,i}$ is the diffusion velocity of the i^{th} phase; S_{α_i} is the source term; $\frac{\mathrm{D}}{\mathrm{D}t}$ is the Lagrangian derivative.

In the simulation, the diffusion velocity is neglected, and so it is the last integral too. Moreover, when the fluids are incompressible, the time derivative of the density is null.

The total mass conservation could be expressed as follows:

$$\frac{\partial}{\partial t}\left(\int_\Omega \rho\,\mathrm{d}\Omega\right) + \oint_S \rho\boldsymbol{u}\cdot\boldsymbol{n}\,\mathrm{d}S = \int_\Omega S\,\mathrm{d}\Omega \tag{3.24}$$

where the source term S is equal to the sum of the source terms of all the phases:

$$S = \sum_i S_{\alpha_i \rho_i} \tag{3.25}$$

The vectorial momentum equation is

$$\frac{\partial}{\partial t}\left(\int_\Omega \rho \boldsymbol{u}\ \mathrm{d}V\right) + \oint_S \rho \boldsymbol{u} \times \boldsymbol{u} \cdot \boldsymbol{n} \mathrm{d}S = \oint_S p\mathcal{I} \cdot \boldsymbol{n}\ \mathrm{d}S + \oint_A \mathcal{T} \cdot \boldsymbol{n}\ \mathrm{d}S + \int_\Omega \rho \boldsymbol{g}\ \mathrm{d}\Omega + \\ + \int_\Omega \boldsymbol{b} \mathrm{d}\Omega - \sum_i \int_S \alpha_i \rho_i \boldsymbol{u}_{d,i} \times \boldsymbol{u}_{d,i} \cdot \boldsymbol{n}\ \mathrm{d}S \tag{3.26}$$

where $\mathcal{I}$ is the unit tensor, $\mathcal{T}$ is the stress tensor and $\boldsymbol{b}$ is the vector of body forces.

3.4 The Cavitation Model

The phase and mass conservation from the eqs. (3.24) and (3.26) of the previous section require the knowledge of a source term. In this project, this source is responsible to the phase change due to cavitation. In *STAR CCM+*, there are three cavitation models: *Full Rayleigh-Plesset model*, *Schnner-Sauer model* and *Homogeneous Relaxation model*. Each of them has some peculiarities and it models the bubbles growth rate in different manners.

The *Full Rayleigh-Plesset model* implements the Rayleigh-Plesset equation presented in the *Theory* section in eq. (2.31). The *Schnner-Sauer model* is a simplification of the previous model, where the bubble growth acceleration and the viscous and tension effects are neglected. Lastly, the *Homogeneous Relaxation model* is based on a finite rate equation with an empirical time scale formulation [45]. In this work, only the first two cavitation models are applied. In fact, the *Homogeneous Relaxation model* is not recommended for the project (the Userguide [45] reports that it is suitable for modeling phenomenon which occur in thermal non-equilibrium). Moreover, Brenner [14] reports that, in engineering application, the results from the *Schnerr-Sauer model* are comparable with those obtained applying the *Rayleight-Plesset model*. This statement will be test further in the project when both of the models will be implemented.

All the cavitation models in *STAR CCM+* are based on homogeneous distribution of the nucleation sites; they are also called *seeds* in the software. One of the parameters that the user needs to set is the density of seeds per unit of volume, n_0 (*Seed density*). The model assumes that these seeds are spherical and uniformly distributed in the volume, moreover, all seeds have initially the same radius, R_0. This is the the second parameter that must be set by the user, in the software it is named *Seed diameter*, $D_0 = 2R_0$. The initial radius corresponds also to the smallest value of the radius that the bubble could assume in the domain during the simulation. Another important assumption is that the number of seeds in a control volume is proportional to the volume of liquid. The amount of seeds in this control volume is thus:

$$N = n_0 \alpha_L V \tag{3.27}$$

where α_L is the the volume fraction of liquid.

The total amount of vapour, under the assumption of spherical bubbles, is:

$$V_V = N\left(\frac{4}{3}R^3\pi\right) \tag{3.28}$$

and the phase fraction of vapour:

$$\alpha_V = \frac{V_V}{V} = n_0\alpha_L\left(\frac{4}{3}R^3\pi\right) \tag{3.29}$$

Therefore, once that the volume fraction of liquid and vapour are known, the local radius could be calculated, inverting equation (3.29):

$$R = \left(\frac{3\alpha_V}{4n_0\alpha_L\pi}\right)^{\frac{1}{3}} \tag{3.30}$$

At these point, the user should be aware that the density of seeds and the seed diameter have not a physical meaning. They are simply used to tune-up the physical model and establish a satisfying agreement with the eventual experimental values. In his Master thesis, Andersen [5] reported the following tables of recommended values in case of main phase is diesel fuel; it was taken from the PhD thesis by Giannadakis [23].

	n_0 [1/m^3]	R_0 [m]	α_0
Range of recommended values	$10^{12},\ 10^{14}$	$0.3\ 10^{-6},\ 2\ 10^{-6}$	$5\ 10^{-6},\ 5\ 10^{-5}$

Table 3.1: Recommended values for the initial parameter of the cavitation model suggested by Giannadakis [23]

Lastly, the mass transfer per unit of volume is:

$$\dot{m} = \rho_V\frac{\mathrm{d}V_V}{\mathrm{d}t}\frac{1}{V} = \rho_V\frac{\mathrm{d}}{\mathrm{d}t}\left(N\frac{4}{3}\pi R^3\right)\frac{1}{V} = 4\rho_V n_0\alpha_L\pi R^2\frac{\mathrm{d}R}{\mathrm{d}t} \tag{3.31}$$

Now, the above-mentioned models differ by the method used to calculate the radial bubble growth, $\mathrm{d}R/\mathrm{d}t$, in eq. (3.31). The *Schnner-Sauer model* estimates this quantity from the Rayleigh-Plesset equation, neglecting the bubble growth acceleration, the viscous term and the surface tension:

$$\left(\frac{\mathrm{d}R}{\mathrm{d}t}\right)^2 = \frac{2}{3}\left(\frac{p_{sat}-p_\infty}{\rho_L}\right) \tag{3.32}$$

where p_∞ is the surrounding pressure. When the saturation pressure is larger than the surrounding pressure, the radial bubbles' growth is positive:

$$\frac{\mathrm{d}R}{\mathrm{d}t} = \sqrt{\frac{2}{3}\left(\frac{p_{sat}-p_\infty}{\rho_L}\right)} \tag{3.33}$$

On the contrary, when the surrounding pressure is larger than the saturation pressure:

$$\frac{\mathrm{d}R}{\mathrm{d}t} = -\sqrt{\frac{2}{3}\left(\frac{p_\infty - p_{sat}}{\rho_L}\right)} \tag{3.34}$$

In general:

$$\frac{\mathrm{d}R}{\mathrm{d}t} = \mathrm{sign}(p_{sat} - p)\sqrt{\frac{2}{3}\left(\frac{|p_\infty - p_{sat}|}{\rho_L}\right)} \tag{3.35}$$

Substituting eq. (3.35) in eq. (3.31), the mass transfer per unit of volume is:

$$\dot{m} = 4\rho_v n_0 \alpha_l \pi R^2 \mathrm{sign}(p_{sat} - p)\sqrt{\frac{2}{3}\left(\frac{|p - p_{sat}|}{\rho_L}\right)} \tag{3.36}$$

Lastly, the source term in eq. 3.24 is:

$$S_V = 4n_0 \alpha_l \pi R^2 \mathrm{sign}(p_{sat} - p)\sqrt{\frac{2}{3}\left(\frac{|p - p_{sat}|}{\rho_L}\right)} \tag{3.37}$$

3.5 The Temporal Discretization

The problem of this project is transient, this means that the additional variable *time* must be taken into account. In order to approximate the time derivative of any physical quantity, several methods could be used. In engineering application, the most popular is *Implicit Euler*; it is implemented in *STAR CCM+* and it is applied in the all the simulations of this project.

Depending on the stencil, the user of the software might choose among the first and second order accuracy schemes. The first order time discretization uses the solution of the current (t_{m+1}) and previous (t_m) timestep; in other words, the stencil contains two points. The time derivative of the generic function $\phi(t)$ evaluated at time step t_{m+1} is:

$$\frac{\mathrm{d}\phi(t)}{\mathrm{d}t} = \frac{\phi(t_{m+1}) - \phi(t_m)}{\Delta t} \tag{3.38}$$

In the second order accuracy scheme, the stencil counts three points; in addition of the solution at level t_{m+1} and t_m, the value of the function at time t_{m-1} is needed too:

$$\frac{\mathrm{d}\phi(t)}{\mathrm{d}t} = \frac{\frac{3}{2}\phi(t_{m+1}) - 2\phi(t_m) + \frac{1}{2}\phi(t_{m-1})}{\Delta t} \tag{3.39}$$

The choice of the time-step Δt is based on the Courant-Friedrichs-Lewy (often abbreviated as CFL) condition, which establishes the condition for convergence when partial differential equations are solved. In CFD, the time step is calculated from the definition of the Courant number:

$$C = \frac{u\Delta t}{\Delta x} \tag{3.40}$$

This non dimensional number must be smaller than 1 to ensure that the information is not propagating through more than cell in the given time-step. Values higher than 1 might lead to instabilities and the solution might not be reliable.

3.6 The Turbulence Model

In all the simulations, the Reynolds number is expected to be higher than the critical value. In fact, the laminar limit for a flow in pipe, which could be considered a simplified model of a nozzle hole, is around 2,000 while the expected Reynolds number has an order of magnitude at least equal to 10^6. Therefore, the flow is turbulent and the Reynolds stresses must be taken into account. It is not the purpose of this work to discuss in detail the turbulence modelling; please refer to Wilcox [49] for a very detailed analysis with the focus on the implementation in CFD codes.

The signal of every fluid-dynamic quantity in a turbulent flow could be decomposed in mean value and fluctuating component. With this in mind, consider the horizontal component of the velocity vector, u:

$$u = \overline{u} + u' \tag{3.41}$$

where $\overline{u}$ refers to the mean value and u' to the fluctuating component. Note that, by definition, $\overline{u'} = 0$. The procedure of decomposing the signal in mean value and fluctuating component is called Reynolds decomposition. When the three components of the velocity vector and the pressure are decomposed as above, and they are inserted in the Navier-Stokes equations, eq. (3.7), one could get the following expression (known as Unsteady Reynolds Average Navier-Stokes equation, or more simply, URANS):

$$\rho\left(\frac{\partial \overline{u_i}}{\partial t} + \overline{u_j}\frac{\partial \overline{u_i}}{\partial x_j}\right) = \rho g_i + \frac{\partial}{\partial x_j}\left(\overline{\tau_{ij}} - \rho\overline{u_i' u_j'}\right) \tag{3.42}$$

The main difference from eq. (3.7) is the presence of the terms $-\rho\overline{u_i' u_j'}$ in the right hand side brackets. They come from the convective term of the Navier-Stokes equation:

$$\frac{\partial}{\partial x_j}(\overline{\rho u_i u_j}) = \rho\overline{u_j}\frac{\partial \overline{u_i}}{\partial x_j} + \frac{\partial}{\partial x_j}\left(\rho\overline{u_i' u_j'}\right) \tag{3.43}$$

The terms $-\rho\overline{u_i' u_j'}$ are the components of a symmetric second order tensor (9 entries but only 6 independent) and they might be interpreted as additional stresses due to turbulence. This is the reason why they are called Reynolds stresses and they are merged with the viscous stresses in eq. (3.42), even though they originate from the convective term, in the left hand side of the Navier-Stokes equation.

At this point, there are four equations (continuity and three Reynolds Averaged Navier Stokes equations) but ten unknowns (pressure, three components of velocity and the six Reynolds stresses); it means that the problem is not closed. Consequently, methods to compute the terms $\overline{u_i' u_j'}$ have been developed. In literature, the turbulence models could be classified in three families: algebraic models, turbulence-energy equations model and simulation models, which includes Large Eddies Simulation (LES) and Detached Eddies Simulation (DES). In this project, only the turbulence-energy models are used because they offer the best compromise between computational time and precision. Indeed, the LES and DES require that the number of grid point to resolve the smallest length-scale of turbulence (Kolmogoroff's length scale) is proportional to Re^3 [36]. For high Reynolds

number ($\approx 10^6$), the domain require a tremendously large number of cells. This is the reason why these turbulence models are only used for simple geometry and small scales.

The most common turbulence-energy models are based on two additional equations. Because of that, they are named $k-\epsilon$ model and $k-\omega$ model, where k refers to the turbulent kinetic energy, ϵ is the rate of dissipation of turbulent energy and ω is the specific dissipation rate. *STAR CCM+* provides the possibilities to use both of these models. In particular, the $k-\omega$ model is implemented using Menter's modification ($k-\omega$ SST), which is aimed to have higher sensibility in case of adverse pressure gradient. The software allows to scale the turbulent viscosity too, which is the analogous term of the dynamic viscosity in the Reynolds stresses.

3.7 The Overset Mesh

The overset mesh (also known as *chimera*) is a technique used to simulate the motion of overlapping meshes. The method requires one fixed mesh (commonly known as background), and one (or more) moving mesh, the overset. The theoretical approach was developed in 1983 by Atta and Vadyak [6] and their work represents a milestone in this field. It is not the aim of this thesis to discuss in depth the technique and the algorithm (the User Guide [45] provides a lot of information in this sense) but the main ideas are here presented.

The overlapping of the meshes poses a central topological problem: how is the flow field information transmitted from one mesh to another? This question is solved by the algorithm implemented in *STAR CCM+* sorting the cells in the domain in four families: *active cells*, *passive cells*, *donor cells* and *acceptor cells*. In the active cells, as the name suggests, the discretized governing equations are solved. This does not happen in the passive cells; they are the cells in the background that are blanked out due to the motion of the overset region. Of course, during the simulation, depending on the position of the overset mesh, an active cell could become passive, and viceversa. The donator cells are the cells used to provide information between the meshes; this is possible through the acceptor cells that are located in the boundary between background and overset. They receive the interpolating information from the donor cells. A simple representation of how the information are exchanged from cell to cell is depicted in figure 3.1. The background mesh is colored in blue, while the overset is in red. From the mathematical point of view, the information in the external cells (coloured in blue and orange and belonging respectively to the background and overset) is calculated through the use of the acceptor cells. In the picture, two acceptor cells (one in the background and the other in the overset mesh) are depicted with dashed lines. The information in the centroid of the acceptor cell is calculated from the cells in the background. In case of a 2 dimensional analysis, three background cells are used for this purpose. In three dimension, they are four. These cells are selected in a way that the centroid of the acceptor cell is located in the triangular (in 2D) or in tetragonal (in 3D) shape formed connecting the centorids of the background cells, as depicted in green in the figure. In this way, through interpolation (*STAR CCM+* provides four different methods of interpolation) the information is calculated in the centroid of the acceptor cell, and

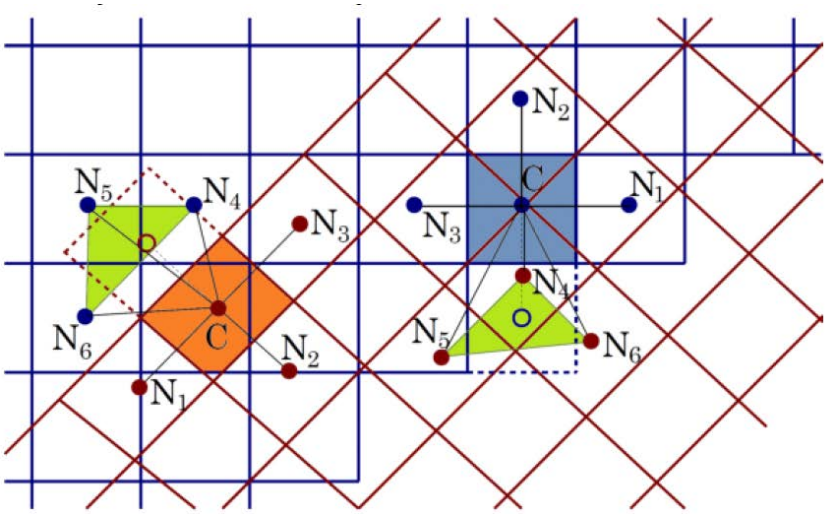

Figure 3.1: The two overlapping meshes and the relation between the acceptors, donors and active cells. Picture from the Userguide [45]

finally it is transmitted to the cell in the out-most layer of the active cells. The software provides the scalar functions *Cell type* and *Cell status* to visualize the cell attributes; they are extremely important to debug eventual errors.

Another important topic regarding the overset mesh is the interaction between the wall boundaries of the background and overset mesh. It is clear that when the gap between the walls is small, there are not enough acceptor cells that could be used for the exchange of information. This might be an issue for all the mechanical components (in most of the cases, valves) which require contacts between the moving and still parts. Fortunately, *STAR CCM+* provides the command named *Zero Gap Overset Interface*. Through this command, a new wall boundary is created to artificially closing out some cells and simulate the real contact. This command is essential in the simulations of this project since it allows to simulate the contact between seat and cut-off shaft.

In the project, the option *Alternate Hole Cutting* is used; let us summarize its effects. The algorithm responsible for the detection of the acceptor cells is called *hole cutting*. The hole cutting algorithm in its classic version (also known as *layered approach*) deactivate all the cells of the background mesh that are completely covered by the cells of the overset region. The alternative algorithm (known as *global approach*) consists in deactivating the background cells whose centroids are covered by the overset mesh. The evident consequence of this approach is that the number of background cells deactivated is larger and it might return in a higher stability of the simulation.

In conclusion, there are several practices to make the best use of the overset technique, here the most important are listed.

Topological rule: mesh size should match as much as possible around the overset boundary [45]. The main reason is that it assures the most correct interpolation possible. Most of the issues due to the robustness and conservation could be solved in this way. In general, the user should prefer a tight fit mesh for the overset region. This shape allows to have smaller cell counts and it permits the motion of the overset in small gaps.

Temporal discretization rule: when the time integration is set to the 1^{st} (or 2^{nd}) order implicit Euler scheme, the maximum displacement of the overset must be equal to the smallest (or to half the smallest) cell size in the overlapping region. The difference in the scheme order is due to the time discretization; in fact, as shown in the section *The Temporal Discretization*, the first order Euler requires the values of the previous time step, while the second order Euler requires the values from the previous two time steps (see eqs. (3.38) and (3.39)).

Chapter 4

Validation cases

As reported in the previous sections, there are not experimental data of the motion of the cut-off shaft in the real injector system. Consequently, there are not information about the cavitation intensity: where and how the vapor bubbles form remains an open question that still needs an answer. Recall that it is very difficult to reproduce experimentally the operating condition of the injector due to the high pressure involved in the process and the velocity of the flow inside the nozzle holes. Moreover, the small dimension of the nozzle and the need of using optical method to detect the vapour bubbles make the investigation extremely complex. This is the reason why computational fluid dynamics is an essential tool to predict the behaviour of the fluid and, eventually, optimize the design of the injector.

The lack of the experimental data at the opening and closing of the fuel valve implies the need of taking a step back and validating the physical models using test cases. With the aim of making *everything as simple as possible but not simpler*[1], two validation cases are considered. The first of the list is about the unsteady cavitation in a converging-diverging nozzle. This test allows to gain confidence with the numerical simulation of multiphase flows when the geometry is not too complex. The second validation case is about the single phase flow of diesel fuel in the injector when the cut-off shaft is moving. This is possible through the use of the overset technique, one of the most popular method to simulate the motion in CFD. A more detailed description of the tests is presented in the following sections.

4.1 Unsteady cavitation in an axisymmetric Venturi nozzle

Time-dependant cavitation is expected in the injection system at the operating condition; for this purpose, a validation of the multiphase flow with respect to time is required. The

[1]The sentence in italics is attributed to Einstain (The Herbert Spencer Lecture, delivered at Oxford in June 1933) and it is known as Einstain's razor, in analogy of Occam's razor.

unsteadiness of the vapor bubbles is mainly due to the displacements of the cut-off shaft and the time-dependant inlet and outlet pressures at the boundaries.

In literature, there are several experiments regarding the periodic shedding of cavitation clouds around different geometries. For instance, extensive researches have been conducted for cavitating hydrofoils, in the hope of studying erosion, vibration and noise produced by the collapse of the vapor bubbles [35, 30]. Being an external flow, this experiment is not really suitable for the investigation of this Master project, where the attention is addressed to internal flows. Internal flow means that the fluid must be bounded by a surface where the boundary layer develops. With this in mind, the simulation of the unsteady cavitating flow in a converging-diverging nozzle is performed, replicating in *STAR CCM+* the laboratory conditions reported in the article *Dynamics of partial cavitation in an axisymmetric converging-diverging nozzle* by Jahangir, Hogendoorn and Poelma [28]. The numerical results will be then compared with the authors' data.

It is relevant to mention that, even for simple geometries, the cavitation mechanisms are not fully understood, especially as regards the onset of cavitation. The unsteadiness, the turbulence and the interaction between vapor cavities contribute to making cavitation difficult to comprehend. This is the reason why experiments performed with more and more complex techniques are needed even in these days. It is clear that it affects the reliability of numerical models and, in general, it is hard to obtain results with a sufficient accuracy. In literature, there are several articles aimed at reproducing the unsteady cavitation in two dimensional Venturi nozzle or in axisymmetric geometries. For instance, Yuang et al. [51] worked with the *Volume of fluid* technique and the Schnerr-Sauer cavitation model to model the two phase flow in an axisymmetric 2D nozzle. The authors used the URANS equation with the standard k-ϵ model and they reported slightly oscillation in the location of the cavity wake. As it will be discussed in the further sections, the turbulence model plays an important role in the modelling of this problem. Reboud et al. [43] and Coutier-Delgosha et al. [17] studied the influence of several turbulence model in a two dimensional Venturi-type section. In particular, noting an underestimation of the turbulent viscosity near the vapor cavity, Reboud proposed the use of a scaling factor. The only article I was able to find about the axisymmetric Venturi is by Gorkh et al. [24]. The authors used the same geometry presented in the following section (but in 3-D) and they were able to simulate the re-entrant mechanism for high cavitation number, σ. Unfortunately, in the paper, many information are missing; the turbulence model is not mentioned as well as the cavitation model.

This section is organized as follows: in the first subsection, the experiment by Jahanagir et al. [28] is presented and particular attention is addressed to the causes of the cavitating flow. The mechanisms of the multiphase flow are described and the non dimensional numbers are presented. The other subsections follow the work-flow of the software *STAR CCM+*: in the order, geometry, physics, boundary conditions, mesh and solvers. The results are described by means of pictures and plots. Lastly, in the discussion, the agreement between the numerical and experimental results is discussed.

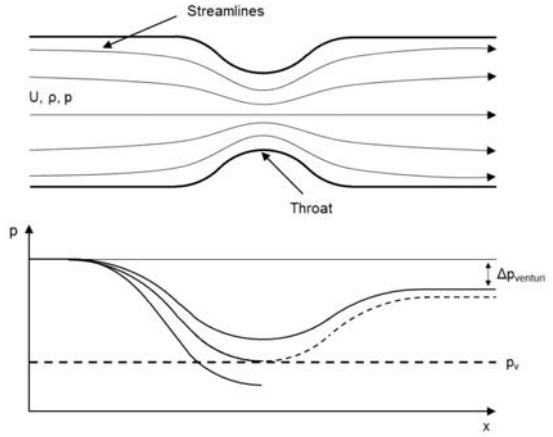

Figure 4.1: Streamlines ($above$) and the pressure distribution ($below$) along the length of a one dimensional converging-diverging nozzle. The dotted line shows the onset of the multiphase flow. In case of cavitation, it is not possible to describe the pressure distribution far from the throat. The picture is from Hogendoorn's Master thesis [26].

4.1.1 The Overview of the Experiment

The experiments by Jahangir et al. [28] are aimed at detecting the periodic shedding of cavitation clouds in a three dimensional axisymmetric converging-diverging nozzle. The nucleation and growth of the vapor bubbles could be explained as a consequence of the velocity increase in the throat section. This is very similar of what happens in diesel injectors; in this regard, refer to Nurick's one dimensional model [39] presented in the *Theory* chapter. Here, the physical reasons are reported again to give the picture of the phenomenon in a Venturi nozzle.

With the assumption of steady, incompressible, single phase flow, and neglecting the gravity, Bernoulli's equation might be applied along a streamline:

$$\frac{1}{2}\rho u^2 + p \mid_{\text{along a streamline}} = \text{const.} \tag{4.1}$$

Since the velocity reaches its maximum in the throat, here, the pressure might drop under the saturation limit at operating temperature. Therefore, the throat is the critical section where the onset of cavitation might occur.
A nice representation of the streamlines and pressure distribution in a one dimensional model is depicted in figure 4.1. Here, three pressure functions are depicted with the aim of visualizing as many different conditions. If the pressure along the symmetry axis is always above the saturation condition, cavitation will not occur. The onset of cavitation begins when, at least in one point, the pressure reaches the critical value: $p(\widetilde{x}) = p_{sat}$. As it was stated before, the coordinate $\widetilde{x}$ corresponds to the neck of the Venturi nozzle. Lastly, when a multiphase flow is expected, it is impossible to predict the trend of the pressure function

with respect of the x-coordinate.

In order to study different cavitation regimes, Jahanguir et al. [28] performed several experiments varying the outlet pressure. To explain their procedure, it is useful to recall one of the definitions of the cavitation number introduced in the *Theory* chapter:

$$\sigma = \frac{p - p_{sat}}{\frac{1}{2}\rho u_0^2} \tag{4.2}$$

In a converging-diverging nozzle, p refers to the outlet static pressure (in other context, it might be the inlet static pressure) and u_0 is the flow velocity at the throat. Hogendoorn [26] pointed out that the outlet static pressure is the driving force of the cavitation in a Venturi. Let us consider a situation where the inlet pressure is fixed. A large outlet pressure (but, of course, lower then the inlet pressure) implies a low Δp between inlet and outlet and low velocity at the throat because of eq. (4.1). In these circumstances, cavitation is not likely to occur and the cavitation number σ is large. On the contrary, low outlet pressure implies an high driving force, high flow velocity through the neck section and a tumultuous cavitation regime. This situation is described by a low cavitation number, σ.

In literature, depending on the cavitation number, three cavitation mechanisms are described in a Venturi nozzle. They are the re-entrant jet mechanism, side entrant jet mechanism and bubble shock mechanisms. In this validation case, the re-entrant jet mechanism is considered. It is the first (discovered in 1955 by Knapp [29]) and most studied mechanism. Moreover, it is relevant to this project since it was observed at the inlet of nozzles holes in diesel injectors too. In this regard, Sato and Saito [44] observed periodic cavities of vapor in a circular cylindrical nozzles. The authors noted that the bubbles grew until they reached a characteristic length, L_{cav}, after that, a portion of the bubble was set apart and it was advected by the surrounding flow. More recently, the same phenomenon was observed in the experiments by Stanley et al. [47].

A brief presentation of the re-entrant jet mechanism is here discussed. The cycle could be described in four time-steps:

- A cavity forms at the end of the breaking cycle in the throat of the Venturi nozzle. The bubble clouds (which is set apart from the previous cycle) is advected through the diverging section of the nozzle.

- When the cavity reaches its maximal length (L_{cav}), a re-entrant jet begins to form. As reported in several papers ([30], [15]), the re-entrant jet is due to the impingement of the fluid surrounding the vapor cavity on the wall.

- The re-entrant stream reaches the throat of the Venturi nozzle and a part of the cavity is set apart. A bubble cloud now is formed.

- The bubble cloud is advected while a new cavitation sheet begins to form again.

In figure 4.2, the four steps of the break-off cycle are depicted in a converging-diverging nozzle.

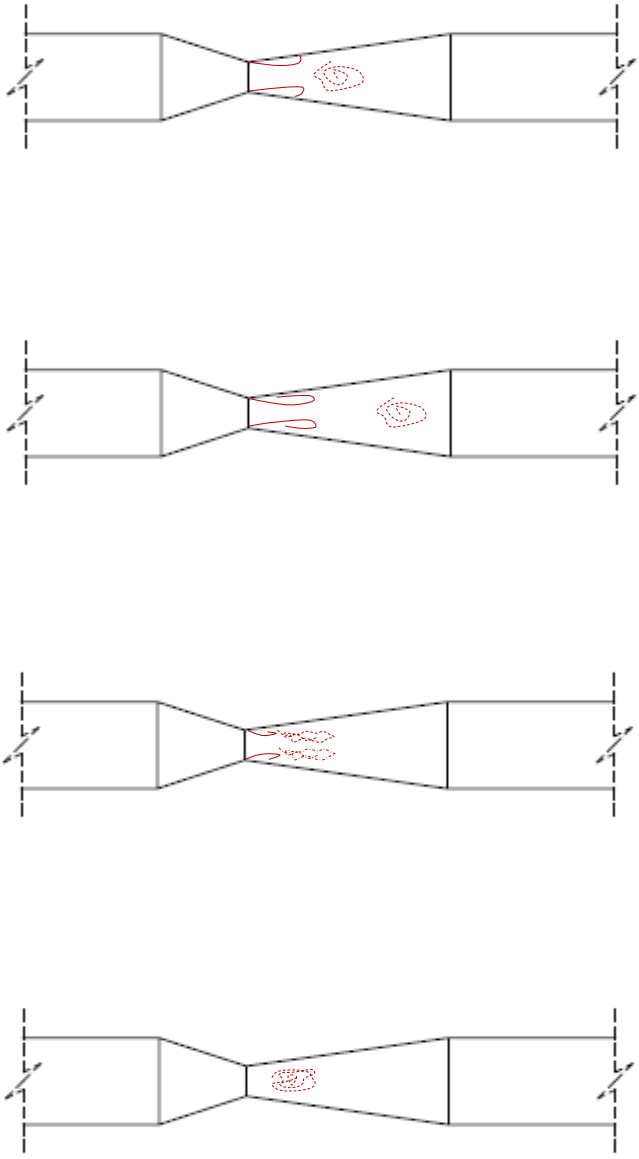

Figure 4.2: Scheme of the break-off cycle in a converging-diverging nozzle. The flow is from left to right.

Lastly, the non dimensional numbers used in this study are presented. They are the Reynolds number and Strouhal number. The Reynolds number is the ratio between the inertial and viscous forces. The throat diameter (D) is the characteristic length, and the fluid velocity at the throat (u_0) is the characteristic velocity:

$$\mathrm{Re} = \frac{u_0 D}{\nu} \tag{4.3}$$

In the simulations, the Reynolds number is above its critical value (in full pipe flows, $Re_{critical} = 2,000$). As a consequence of that the flow is turbulent.

The Strouhal number is the dimensionless number used to describe oscillating phenomenon. In this context, it is defined as follows:

$$\mathrm{St} = \frac{fD}{u_0} \tag{4.4}$$

where D and u_0 have the same meanings as above, and f is the shedding frequency. In literature [26], it is possible to find also another definition of the Strouhal number, where the length of detachment (L_{cav}) is considered instead of the diameter of the throat, D. In this case, the Strouhal number has the meaning of ratio between the cavity growth velocity and the free stream velocity:

$$\mathrm{St}_l = \frac{fL_{cav}}{u_0} = \frac{u_{cav}}{u_0} \tag{4.5}$$

4.1.2 Geometry

The experimental rig described by Hogendoorn [26] and Jahangir et al. [28] is depicted in figure 4.3. The circuit is closed and the flow is assured by a centrifugal pump which is installed at the lower place in the laboratory, in order to prevent cavitation inside the hydraulic machine. The pipe before the Venturi has a length of 40 diameters of the inlet section in order to have a fully developed turbulent flow. This condition (in literature it is attributed to Nikuradse [38]) appears very conservative on the numerical point of view. In the simulation, a length of 10 inlet diameters is considered sufficient to reach the fully developed turbulent flow as suggested by Cengel and Cimbala [16].

As regards the Venturi geometry, it is shown in figure 4.4. The cone angles are equal to 18° in the converging section and 8° in the diverging section. The diameters at the inlet and outlet of the Venturi nozzle are equal to 50 mm. Lastly, the ratio between the area of throat and inlet section is equal to 1/9, leading to a radius of 8.3 mm in the neck.

In general, simulations aimed at reproducing the cavitating flow require fine mesh and a small time step. The former is essential to have an adequate resolution of the phenomenon (especially when the *VOF* method is used), the latter is needed to avoid undesired averaging in time. The main consequence is that the simulations might be CPU intensive. For this reason, the axisymmetry is invoked. In fact, not only the geometry of the Venturi noz-

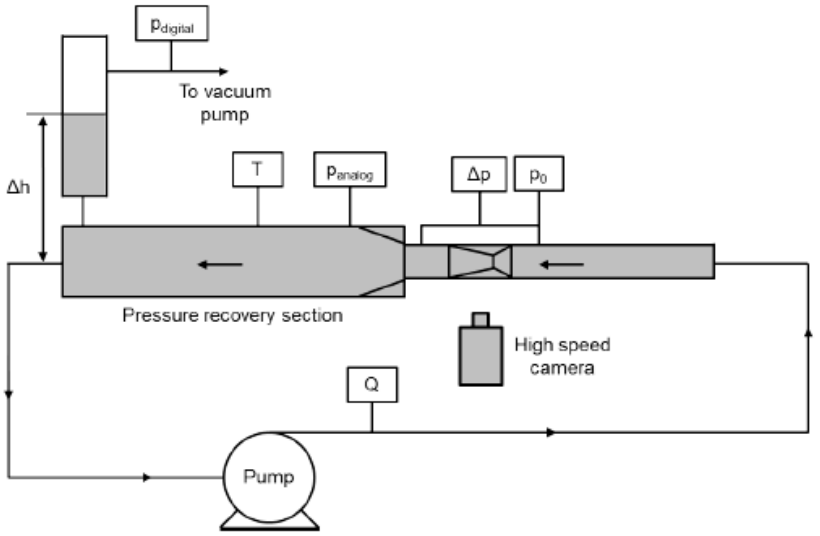

Figure 4.3: Overview of the experimental rig described in the experiment by Jahanguir et al. [28] and reported in Hogendoorn's Master thesis [26].

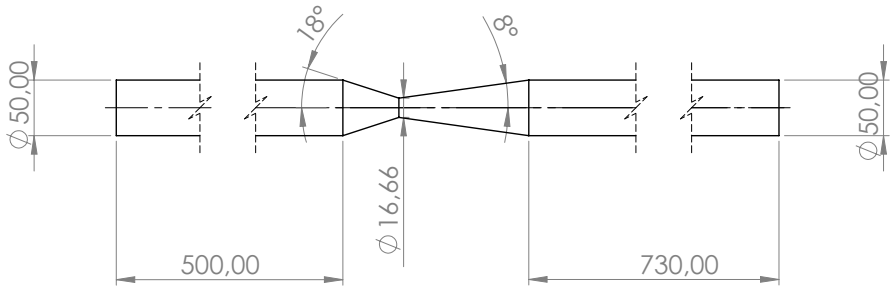

Figure 4.4: The geometry of the converging-diverging nozzle used in the simulations.

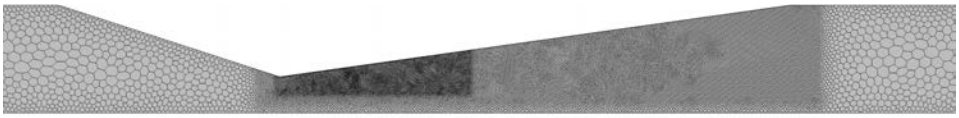

Figure 4.5: Picture of the mesh, with the two rectangular area refinement.

	Very coarse	*Coarse*	*Fine*	*Very Fine*
Base Size	1 mm	1 mm	1 mm	0.8 mm
Size Refinement 1	0.8 mm	0.6 mm	0.4 mm	0.3 mm
Size Refinement 2	-	0.4 mm	0.2 mm	0.1 mm
Number of cells	31,070	36,175	51,538	104,847

Table 4.1: Dimensions of the meshes used in the analyses.

zle is axisymmetric, but the vapour clouds appear to be axisymmetric too[2]. This is one of the most relevant assumption of this validation case.

4.1.3 Mesh

With the purpose of checking if the solution is mesh independent, four different grids are considered. They are named *Very coarse*, *Coarse*, *Fine* and *Very fine*, depending on the base size. All meshes are polygonal, unstructured and with prism layers. The most relevant dimensions are reported in table 4.1. In all the results presented in the further sections, the mesh *Fine* is used; the other meshes will be considered only in the further study presented in the *Discussion* section.

The mesh is depicted in figure 4.5, where the reader might note two area refinements. The first area refinement is in correspondence of the diverging part of the nozzle, the second one is located in the place where cavitation is expected. These two area refinements are needed in order to keep the scalar function *Volume change* in the recommended range (larger than 10^{-3}) [45]. The *Volume change* scalar field calculates the volume ratio between the cell of interest and its neighbors; large gradient of the cell areas must be avoided.

Another important parameter which must be taken into account in the meshing process is the $y+$ value. $y+$ is a non dimensional wall coordinate used to distinguish the three zones of the turbulent boundary layer: the viscous sub-layer, the buffer layer and the logarithmic layer. $y+$ is defined as reported in eq. (4.6):

$$y+ = \frac{yU_f}{\nu} \tag{4.6}$$

[2]Note that a symmetric geometry does not necessarily imply a symmetric flow field; in this regard, think about the flow around a cylinder for high Reynolds.

	ρ [kg/m^3]	μ [Pa s]	γ [N/m]	p_{sat} [Pa]
Water	998.2	0.001001	0.072	2339
Vapor	0.01731	9.7272 10^{-6}	-	-

Table 4.2: Physical proprieties of water and water vapor at $T = 20°$.

where U_f is the friction velocity. The friction velocity is defined as the square root of the ratio between the wall shear stress (τ_0) and the density:

$$U_f = \sqrt{\tau_0/\rho}. \tag{4.7}$$

In order to have a full resolution of the turbulent boundary layer including the viscous sub-layer, it is required that $y+ \approx 1$. This condition might be important in the reliability of the results since the re-entrant jet develops close to the walls.

4.1.4 Physics

The problem is approached using the solver *Segregated Flow* and the Eulerian multiphase approach *Volume of Fluid (VOF)*. As suggested by the Userguide [45], the two phases are simulated as incompressible fluids. It is worthwhile to mention that the compressibility effects of the liquid are negligible since the velocity is far below the speed of sound. In particular, it is less than 0.3 Mach, the threshold value from which the compressability effects starts to be relevant. The experiments are performed at constant temperature, thus, the thermal effects are neglected. In other words, the equation of state and the energy equations are not required.

STAR CCM+ demands in input the following physical proprieties for the liquid and gas phases: density, dynamic viscosity, saturation pressure and surface tension (only when the full Rayleigh-Plesset cavitation model is enabled). The numerical values are retrieved using the software *EES-Engineering Equation Solver*, which stores the thermodynamic proprieties of the most common fluids. In the experiments, the operating fluid is water at room temperature. Since it is not explicitly stated in the article by Jahanguir et al. [28], the temperature is set equal to 20°C (standard conditions). The physical proprieties of water and water vapor are summarized in the table 4.2.

As regards the cavitation modelling, both the Schnerr-Sauer and full Rayleigh-Plesset models are used. Regardless of which cavitation model is used, *STAR CCM+* requires two parameters in input: the seed density (n_0) and the seed diameter (d). At this point, it is relevant to mention that these parameters have not physical meanings: they are used to tune-up the simulations.

Incidentally, the way in which the seed density and diameter are defined in the User-guide [45] might lead to misunderstandings. In fact, the seed density and the seed diameter might be evaluated experimentally in the laboratory, since impurities are need as nucleation site for the vapor cavities. In general, they are small bubbles of air or other immiscible gases [14]. Unfortunately, there is not correlation between the seed density

and diameter in the numerical model and the same quantities in the actual experimental conditions. This means that a large number of tests needs to be performed varying the seed density and seed diameter to find the couple of values that best resemble the experimental results. This statement finds confirm in the article by Yuan, Schnerr and Sauer [51]. In the paper, referring to their projects, the authors wrote: "*... the nuclei concentration n_0 must be at least of the order of 10^{14} nuclei / m^3 in water to establish satisfying agreement with experiments*". Andersen [5] conducted an investigation on this two parameters and he reported in his Master thesis a table of recommended values retrieved from the literature [23]. This table is presented also in this work too, in table 3.1. As far as possible, the range of values reported in table 3.1 has been respected through the entire project.

The turbulence model deserves special attention. Because of time and resources, the closure problem is solved by means of the turbulence models based on the energy equations. Both the k-ϵ and SST k-ω (Menter) turbulence models are tested. These two models have strengths and weaknesses; on one hand, the k-ϵ model is more reliable in 2D but it is not built and optimized to deal with adverse pressure gradient problems as the k-ω model [36]. On the other hand, the k-ω turbulence model is not fully reliable in case of two dimensional axisymmetric problem. When these two turbulence models are used, only a weak unsteadiness was observed due to the high value of the turbulent (or eddy) viscosity around the vapor pockets [17]. Through further investigation in literature, a new formulation of the eddy viscosity was implemented. The method is by Reboud et al. [43] and it consists on multiplying the turbulent viscosity by a scaling function f. The function f depends on the fluids' densities, the local value of density and a constant n, namely Reboud's coefficient.

$$f(\rho) = \frac{1}{\rho}\left[\rho_V + \frac{(\rho - \rho_V)^n}{(\rho_L - \rho_V)^{n-1}}\right] \tag{4.8}$$

where:

$$\rho = \alpha_V \rho_V + (1 - \alpha_V)\rho_L \tag{4.9}$$

and the subscription L and V refer to the liquid and vapor phase. In the expression (4.8), Reboud suggests to use $n = 10$. The Reboud's correction is implemented using two *User field functions*, `n` and `Reboud` and activating the node *Turbulent viscosity scaling*. The field functions are:

```
n=10

Reboud =1/$Density*(0.01731+pow($Density-0.01731,$n)/
       /pow(998.2-0.01731,$n-1))
```

Lastly, a plot of the non dimensional function $f(\rho)$ for $n = 10$ is presented in figure 4.6.

4.1.5 Boundary Conditions

The numerical model requires four boundary conditions, one for each edge of the geometry. For clarity purposes, the edges are depicted in figure 4.7. In the inlet, the boundary condition is *Velocity inlet*. The numerical value of the velocity at the inlet of the nozzle is calculated from the cavitation number (σ) and the outlet pressure (p). In fact, from the

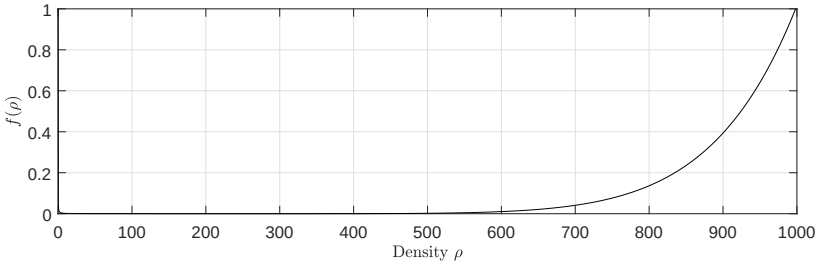

Figure 4.6: The function $f(\rho)$ for $n = 10$.

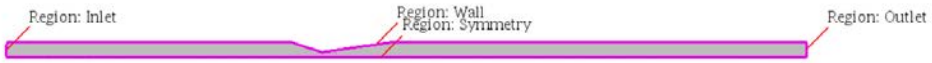

Figure 4.7: The four edges in the Venturi nozzles: inlet, outlet, symmetry and wall.

corresponding numerical values, the velocity at the throat could be computed as follows:

$$u_0 = \sqrt{\frac{p - p_{sat}}{\frac{1}{2}\rho\sigma}} \tag{4.10}$$

Moreover, invoking the continuity equation and the incompressability of the liquid, the velocity at the inlet is:

$$u_i = u_0 \left(\frac{D_0}{D_i}\right)^2 \tag{4.11}$$

When the *VOF* method is used, the additional boundary condition of the volume fraction of water/vapor in each surface is required. The minimum value of the volume fraction of vapor is calculated from the seed density n_0 and seed diameter d. Thus, the volume fraction in the boundary is:

$$\alpha_V = \frac{\frac{4}{3}n_0\pi(d/2)^3}{1 + \frac{4}{3}n_0\pi(d/2)^3} \tag{4.12}$$

As regards the outlet, the boundary condition *Pressure outlet* is used. Its magnitude is chosen from the experimental values reported by Jahangir [28]. The volume fraction of water/vapor must be defined also for this edge. Since it is expected that the bubbles collapse in the diverging part of the Venturi, the minimum value for the volume fraction of vapour is assigned using eq. (4.12).

The no-slip condition has been established through the boundary condition *Wall* for all the internal surfaces of the nozzle. Lastly, because of the axisymmetry, the boundary condition for the symmetry axis is simply *Axis*.

4.1.6 Solver

As reported in the chapter *Model*, the only solver compatible with the *VOF* method is *Segregated flow*. The time discretization is *Euler Second Order* and the time step is $\Delta t = 10^{-6}$ s. The choice of this time step is justified by the Courant-Friedrichs-Lewy convergence condition. The time step allows to obtain the maximum Courant number below 1 in all the cells of the domain.

In order to avoid the risk of divergence, the flow is initialized disabling the cavitation model. This has been achieved through two *User field functions*. The former resets the vapor source term in the transport equation when the time is below an user-defined threshold given by the latter function. The value used in the simulation is $\Delta t = 10^{-3}$ s. The source term is set equal to zero through the option *ScalingFac+* (which is a scaling factor for the source term) in the Schnerr-Sauer cavitation model. The just-mentioned field function `StartCavitation` and `Cavitiation` are defined as follows:

`StartCavitation=1E-3;` $\texttt{Cavitiation} = (\texttt{Time} < \$\,\texttt{StartCavitation})?0 : 1$

This procedure is compatible only when the Schnerr-Sauer cavitation model is implemented. Otherwise, a single-phase flow is initialized and the cavitation model is enabled only after that the continuity residual has reached a small value (10^{-6}). The inner number of iteration is set in order to have small residuals; tuning up the model, the value 15 is used. Lastly, the stopping criteria is based on the expected frequency, and its value is chosen to be large enough to collect a significant number of periods. In all the simulation, the stopping criteria is set $t_{stop} = 80$ ms.

4.1.7 Results

The test is performed with the outlet pressure equal to 90 kPa and cavitation number equal to $\sigma = 1$. From eqs. (4.10) and (4.11), the flow velocity at the throat and inlet sections is equal to 13.25 m/s and 1.46 m/s respectively. The Reynolds number is 2.2 10^5; the flow is turbulent.
To check the correctness of the model, in a preliminary analysis, the cavitation model is disabled and the single phase flow is analyzed, focusing on the pressure and velocity distribution. The numerical value of the mass flow has been compared with the theoretical value. Once that the results matched, the cavitation model is enabled. Because of the wide range of values which the free parameter (seed density and seed diameter) could assume and the time required to run each simulation, a Guess-and-Test approach is used to have a satisfying agreement with the experimental data.
It is expected that the vapor pockets nucleate and grow in the throat, close the the wall. For this reason a *point probe* is place in its proximity, with the aim of recording the volume fraction of vapor. To be more precise, the coordinate of the probe is $x = 0$ mm, $y = 8.3$ mm. From the analysis of the time evolution of the signal, it is possible to analyze the raw data in the frequency domain through the use of the FFT (in terms of amplitude of the fluctuations, $y = \alpha(t) - \overline{\alpha}$). This procedure has been found to be the most effective; indeed, in the first stages, it was believed that the detection of the shedding frequency could be performed through the effective volume of vapor monitor, but, as shown by Gorkh and al. [24], the dynamics of the vapour bubbles could hide the actual process.

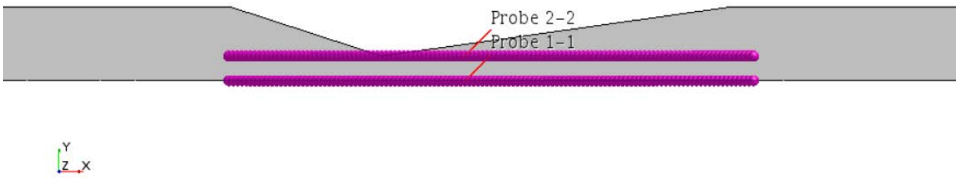

Figure 4.8: The *line probes* used to investigate the pressure distribution in the converging-diverging nozzle.

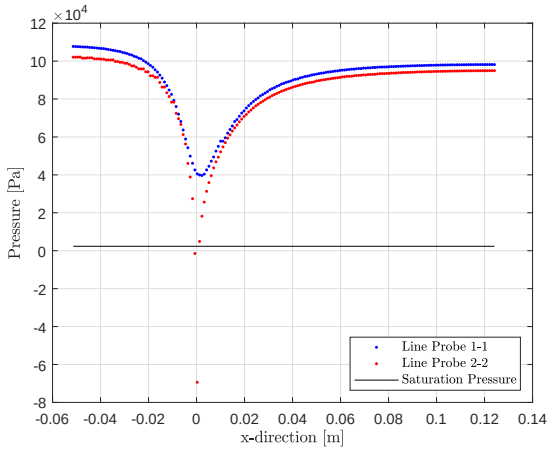

Figure 4.9: Pressure distribution in the converging-diverging nozzle when the cavitation model has not been enabled. This fact justifies the negative pressure detected at the throat by the *line probe 2-2*.

Cavitation Model Turned Off

The pressure distribution in the nozzle when the cavitation source is not enabled is presented in figure 4.9, for two *line probes*. They are parallel to the axis of symmetry and they extend from the inlet of the converging section to the outlet of the diverging section. The *line probes* are depicted in the figure 4.8, where the coordinate system is located in the throat of the converging-diverging nozzle. The plot of the pressure from the probe placed close to the wall looks similar to the one dimensional graph depicted in figure 4.1. Note that the negative pressure is due to the fact that the cavitation model has not been activated yet. This situation describes a metastable liquid where the activation energy is not available and the new stable state could not be reached [45]. The velocity field is presented in figure 4.10. As it was predicted, the velocity in the neck section is, on average, equal to 13 m/s and the maximum is in correspondence of the curvature, close to the wall. It is the location where cavitation is expected.

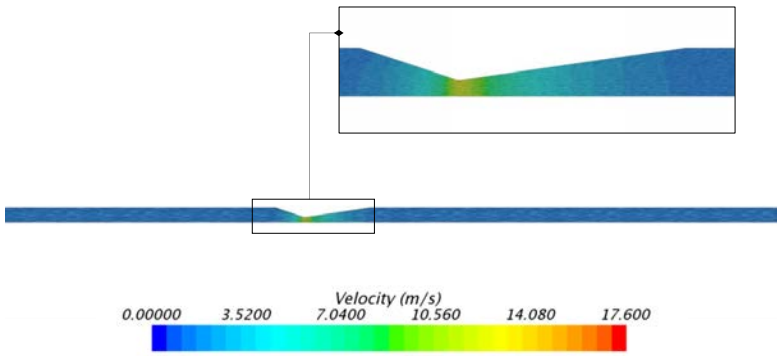

Figure 4.10: The velocity vector field (integral convolution) when the cavitation model is disabled.

Schnerr-Sauer Cavitation Model Turned On

From a preliminary analysis, the couple of values for the seed density and diameter which establishes the best agreement with the experimental results is $n_0 = 10^{11}$ m^{-3} and $d = 5\mu$m respectively. In order to study the turbulence models' influence on the re-entrant break-off period, the following turbulence models are tested:

- Standard k-ϵ
- Standard k-ϵ with Reboud's correction
- Standard SST k-ω
- Standard SST k-ω with Reboud's correction

Let us start considering the standard k-ϵ turbulence model. The time evolution of the signal α_v (volume fraction of vapor) is depicted in figure 4.11. Here the reader might find the analysis in the frequency domain too. In the spectral analysis, the highest peak is located at $f = 104$ Hz, leading to a period T equal to 9.6 ms. Consequently, the Strouhal number is St $= (fD)/u_0 = 0.1303$. From the study of scalar field volume fraction of vapor, the detachment of the vapor cavity is not observed; this means that the physics of the phenomenon is not correctly simulated. It is relevant to mark that this situation is observed by Coutier-Delgosha et al. [17] too, for a two-dimensional geometry of the nozzle. The authors used the standard k-ϵ turbulence model with the barometric cavitation model and they reported that, after an initial transient, the numerical results show a quasi-steady behaviour of the cavity sheet. This means that the re-entrant jet is stopped too early due to the high value of the turbulent viscosity. This explains why a scaling factor is needed for the turbulence viscosity. To reduce the dissipating turbulent term in the zone of the mixture, the scaling factor must be function of the local value of the density. The correction is proposed by Reboud and it was described in the previous section. In addition, the length of detachment appears severely underestimated.

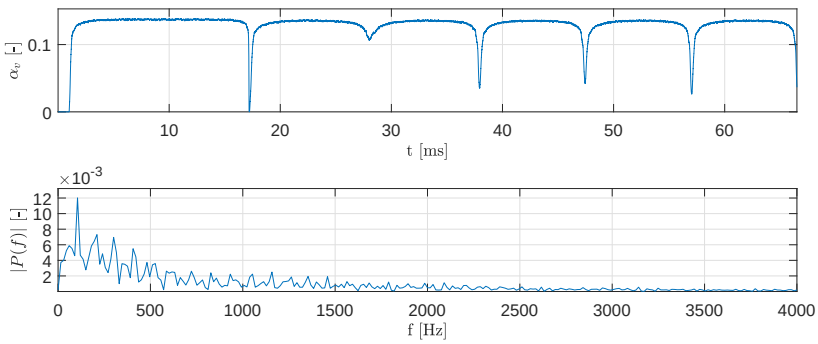

Figure 4.11: Time evolution of the volume fraction of vapor detected by a *point probe* located in the neck of the Venturi nozzle (*above*) and the spectral analysis (*below*). The test is conducted using the standard k-ϵ turbulence model.

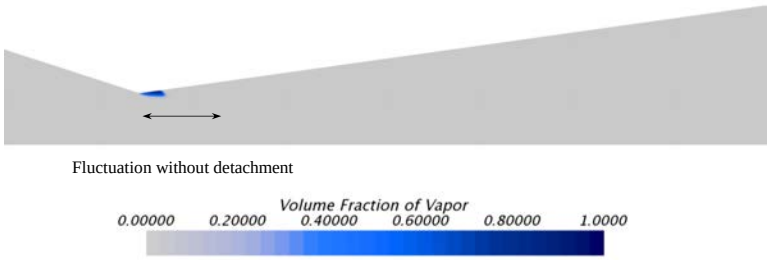

Figure 4.12: The volume fraction of vapor field when the standard k-ϵ turbulence model is used. No detachment is observed.

When the Reboud's correction is implemented in the standard k-ϵ turbulence model, the results in picture 4.13 and 4.14 are obtained. The spectral analysis shows multiple and adjacent peaks having a large amplitude. The highest peak is at 176 Hz, but the range extends from 150 Hz to 200 Hz. The characteristic period is 5.7 ms, leading to a Strouhal number equal to 0.2205. The introduction of the Reboud's correction has led to an increase in unsteadiness of the phenomenon, but the instability do not permit to detect a clear frequency of the cycle. In addition to that, the resolution of the frequency axis is quite large and it has an impact on the reliability of the analysis. On the other hand, it should be noted that the volume fraction of vapor reaches the null value during the simulation; this means that the re-entrant jet has caused the detachment of the vapor sheet, as shown in 4.14.

The introduction of the Reboud's correction has led to a significant increment of the shedding frequency and the detachment of the cavity sheet. For this reason, the standard SST k-ω turbulence model, which suffers of the same problems of the standard k-ϵ, is tested with this improvement. The results are depicted in figure 4.15. The spectral analysis

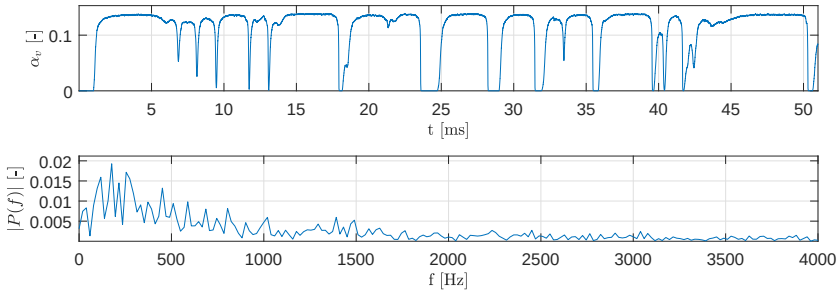

Figure 4.13: Time evolution of the volume fraction of vapor detected by a *Point probe* located in the neck of the Venturi nozzle (*above*) and the spectral analysis (*below*). The test is conducted using the k-ϵ turbulence model with Reboud's correction.

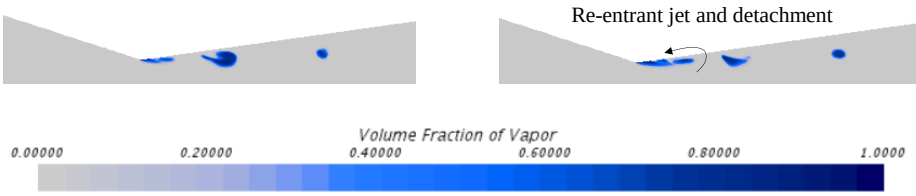

Figure 4.14: The re-entrant jet and the detachment of the vapor sheet. Results obtained through the implementation of the Reboud's correction in k-ϵ turbulence model.

clearly shows a peak located at the frequency of 200 Hz. The characteristic period is therefore equal to $T = 5.0$ ms and the Strouhal number is $St = (fD)/u_0 = 0.2506$.

Rayleight-Plesset Cavitation Model Turned On

In order to study the weight of the bubble growth acceleration, surface tension and the viscous term which are neglected in the Schnerr-Sauer cavitation model, a further simulation using the full Rayleigh-Plesset model is performed. Since the k-ω turbulence model with the Reboud's correction returned the most reliable results, it is used also in this simulation. In figure 4.16, the time-evolution of the signal volume fraction of vapor $\alpha(t)$ and the spectral analysis are presented; in figure 4.17 the detachment event is presented. The highest peak in the frequency domain is located at 225 Hz, leading to a period T equal to 4.4 ms. Thus, the Strouhal number is equal to 0.2819.

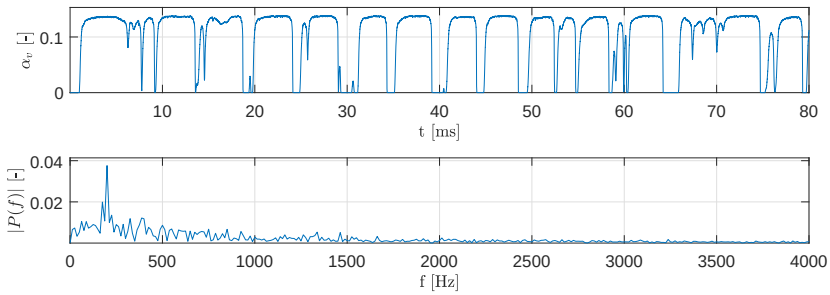

Figure 4.15: Time evolution of the volume fraction of vapor detected by a *point probe* located in the neck of the Venturi nozzle (*above*) and the spectral analysis (*below*). The test is conducted using the k-ω turbulence model with the Reboud's correction.

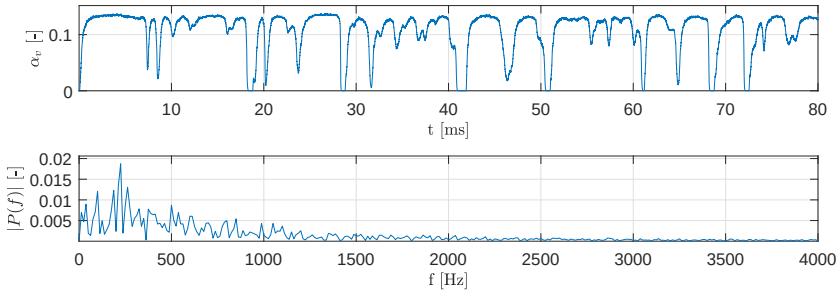

Figure 4.16: Time evolution of the volume fraction of vapor detected by a *Point probe* located in the neck of the Venturi nozzle (*above*) and the spectral analysis of the signal (*below*). The test is conducted using the k-ω turbulent model with Reboud's correction and full Rayleigh-Plesset cavitation model.

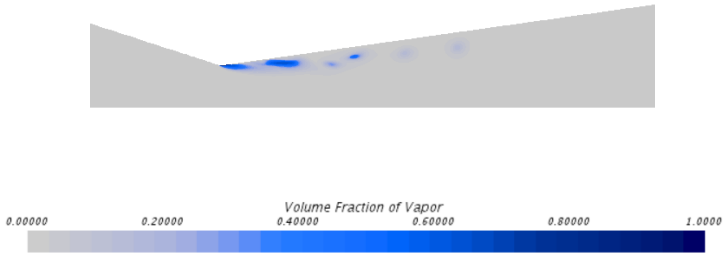

Figure 4.17: Detachment of the vapor bubble with the Rayleigh-Plesset cavitation model, Reboud's correction and $k - \epsilon$ turbulence model.

4.1.8 Discussion

Before discussing in details the numerical results, they are summarized in table 4.3. Again, all the results are obtained with the seed density and seed diameter equal to 10^{11} m^{-3} and 5 μm.

		Frequency [Hz]	Strouhal	Relative Error [-]
Schnerr-Sauer	Standard $k-\epsilon$	104	0.1303	44%
	$k-\epsilon$ Reboud	176	0.2205	7%
	$k-\omega$ Reboud	200	0.2506	6%
Rayleigh-Plesset	$k-\omega$ Reboud	225	0.2819	17 %
Experimental values		188.6	0.2319	-

Table 4.3: Summary of my numerical results and the experimental values by Jahangir et al. [28].

As it might be noted, the turbulence model has a large impact on the solution; this was expected from the analysis by Coutier-Delgosha et al. [17]. In particular, as shown by the authors, due to the high value of the turbulence viscosity close to the cavitation sheet, the re-entrant jet is not able to reach the throat and cause the detachment. This situation might be seen, for instance, in figure 4.11, where the *point probe* always detects a volume fraction of vapor. In addition, when the standard k-ϵ is used, the frequency is underestimated, despite the signal shows a nice periodic behaviour. The relative error is, indeed, large, $\varepsilon_r = 44\%$.

With the aim of decreasing the eddy viscosity close to the cavitation sheet and increasing the shedding frequency, the Rebound's correction is introduced in k-ϵ turbulence model. This leads to an increase of 69% of the shedding frequency. Moreover, in this case, the time evolution of the signal shows that the volume fraction of vapor reaches the zero, meaning that the re-entrant stream could arrive at the neck of the Venturi. However, in the spectral analysis, there is a complex time-evolution of the signal, since multiple peaks around 176 Hz are observed. The range is approximately from 150 Hz to 350 Hz.

Because of the reliability of the SST k-ω turbulence model in case of adverse pressure gradients, the Reboud's modified version of the SST k-ω model is tested. In this case, only one and evident peak is observed in the spectral analysis; it is at 200 Hz. It is close to the experimental data, being the relative error equal to 6%. This value, that at the first glance might appear quite large, is acceptable considering the assumption used in the simulation. The axisymmetry, the use of the URANS equations, the *VOF* method and the cavitation model introduce, unavoidably, errors. From picture 4.18, the dynamics of the cavitation bubbles shows a satisfying agreement with the actual physics. In this picture, the volume fraction of vapour is depicted in the region of interest. The time development is described using the non dimensional time $t^* = t/T$, where T is the shedding period.

The re-entrant jet is observed in the break-off cycle only when the Reboud's correction is implemented. A representation of the velocity field is presented in figure 4.19, zooming on the area of interest for the time-step $t^* = 0.24$. In order to detect the velocity

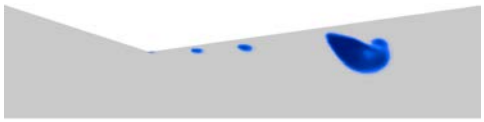

(a) $t^* = 0$

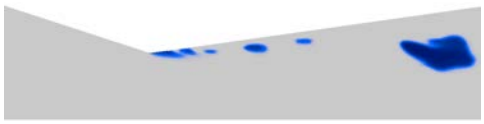

(b) $t^* = 0.24$

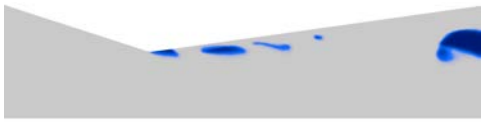

(c) $t^* = 0.29$

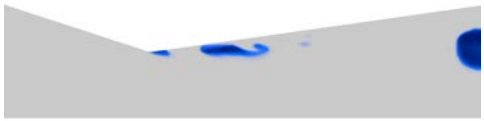

(d) $t^* = 0.41$

(e) $t^* = 0.78$

(f) $t^* = 1$

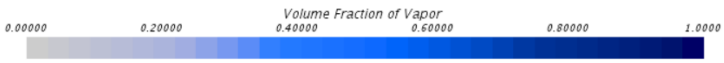

Figure 4.18: The break off cycle obtained using the SST $k - \omega$ turbulence model with the Reboud's correction

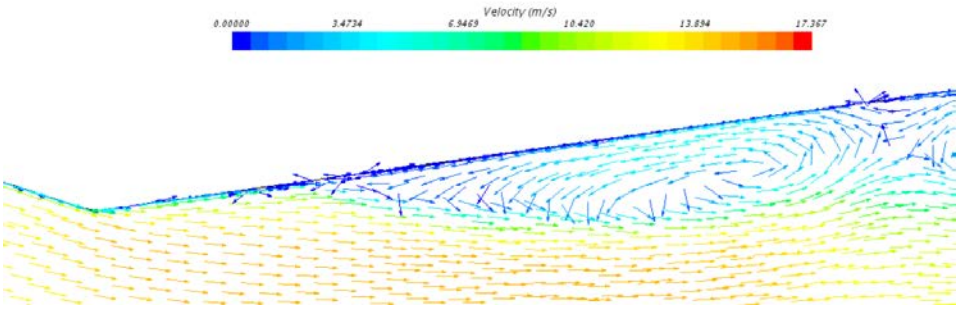

Figure 4.19: Representation of the re-entrant jet detected in the velocity field at the non dimensional time 0.24. The simulation uses the k-ω turbulence model with the Reboud's correction.

vectors, the option *Glyphs* is used. The velocity of the re-entrant jet is of the same order of magnitude of the free stream velocity in the section; this result was expected from the study of the mechanism presented by several authors ([29], [30]). It should be added that the introduction of the Reboud's correction has an impact on the velocity field, since a vortex street might be detected; it contribute to advect the bubble through the geometry.

In order to quantify the weight of terms neglected in the Schnerr-Sauer cavitation model (bubble growth acceleration, viscous term and surface tension), the full Rayleigh-Plesset model is implemented too. Apparently, the introduction of these terms has an impact on the solution, since the highest peak is now equal to 225 Hz. This leads to a relative error of around 17%. It should be mentioned that, in reality, a range of frequencies is detected, approximately from 180 Hz to 250 Hz (with a resolution of 12.5 Hz). In this interval of values, the experimental frequency is included, therefore it in agreement with the data from Jahangir et al. [28]. It is hard to explain this behaviour, but it is believed that the surface tension, bubble growth acceleration and viscosity terms make the flow slightly more unstable than the Schnerr Sauer cavitation model. In addition to that, it should be mentioned that the original Reboud's correction [17] refers to a cavitation model based on the barotropic equation of state[3] and not on the transport, growth and collapse of nuclei as implemented in *STAR CCM+*.

Unfortunately, all tests show an underestimation of the length of the cavity sheet; in fact, the experimenters reported a length of detachment, L_{cav}, equal to the diameter of the throat. In all my numerical simulation, it is approximately half this value. Further studies were conducted with the aim of obtaining the correct length, varying the input parameters, seed density n_0 and seed diameters d but the results were poor. In fact, when the cavity length established a good agreement with the experiments, the dynamics of the bubbles differed significantly from the experimental conditions. Again, this situation might be due to the assumptions used in the simulations. Because of the risk of getting out of track, further investigations are not possible, but this work might be useful for further investigations

[3] To clarify, depending on the local value of pressure, the author used the ideal gas equation ($p < p_v - \Delta p'$), the Tait's equation of state ($p > p_v - \Delta p'$) or a mixing model ($p_v - \Delta p' < p < p_v + \Delta p'$).

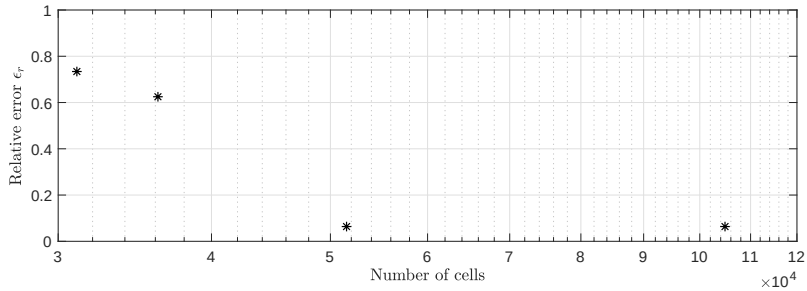

Figure 4.20: Mesh independence study; the four meshes have the following number of cells: 31070, 36175, 51538, 104847.

in the future.

Lastly, a mesh independence test is performed for the Schnerr-Sauer cavitation model, with the corrected k-ω turbulence model. As it was discussed in the previous section, four meshes are used; the reader might refer to the table 4.1 for the characteristic dimensions of each of them. The four simulation are run and, using the procedure of collecting the signal through a *point probe* and performing a spectral analysis, the four characteristic frequencies are recorded. The plot in figure 4.20 shows the relative error in terms of frequencies versus the number of cells. The graph reveals that, from the mesh $Fine$ to the mesh $VeryFine$, the shedding frequency is constant and equal to 200 Hz; further reduction in the base size does not produce visible improvements. This situation might be explained as a consequence of the fixed resolution of the frequency scale, being the time-step constant, thus smaller variation of the characteristic frequency can not be detected.

4.1.9 Conclusion

From this test-case, the following conclusions could be formulated:

- When the cavitation model is implemented, both the Schnerr-Sauer and full Rayleigh-Plesset models can reproduce the experimental unsteadiness of the flow, but only when the Reboud's correction is used. No detachment of the vapor pocket could be detected without the use of this correction.
- The turbulence model has a relevant impact on the mechanisms that causes the shedding. In particular, the k-ω turbulence model with Reboud's correction and Schnerr-Sauer cavitation model returns the most unambiguous results; the output from the Rayleigh-Plesset cavitation model is a range of frequencies, in which the experimental value stands.
- The re-entrant stream is observed once that the Reboud correction is implemented. Therefore, the physics behind the mechanism which governs the shedding is modelled correctly. In addition, velocity of the re-entrant jet was in agreement with the works in literature.

- The length of detachment is underestimated; this might be due to the combined effect of cavitation model and turbulence model. Further investigation using a different cavitation model (barotropic law), turbulence model (Large Eddies Simulation) and Eulerian multiphase method should be performed to obtain clear picture.

4.2 Single phase flow

The second validation case of this project is about the single phase flow in the nozzles of the injector when the cut-off shaft is moving. It allows to gain confidence with the overset technique and make a preliminary analysis of the effects of the motion of the cut-off shaft. Because of the lack of experimental records, the numerical values will be compared with the data from the one dimensional code *1D-Hydcode*, internally developed by MAN Energy Solutions. *1D-Hydcode* implements the one dimensional Navier-Stokes equation and it considers the entire injection system, from the high pressure line to the nozzle holes. In addition, the outputs of this tool (needle lift and pressure in the boundaries) are implemented as inputs for the CFD simulation. This procedure allows a cross validation of the two numerical models. The injection event lasts approximately 30 ms and, due to the small time-step required by the simulations (in the order of micro-seconds), the start of injection (SOI) and the end of injection (EOI) will be studied independently.

Similarly to the previous chapter, this section is organized following the workflow of *STAR CCM+*: the geometry, physics, boundary condition, mesh and solvers are presented. The results are shown and commented in the following two sections.

4.2.1 Geometry

The CAD geometry of the injector is provided by Simon Matlok, research engineer of MAN Energy Solutions. This project is not aimed at simulating the flow in the entire injection system because of the dimensions of the components (recall, for instance, that only the high pressure pipe has a length of 1.9 m) and their complexity. For this reason, only three components of the injector valve located beneath the spring (refer to section 2.9 to remind the injection system) are considered. They are named *spindle guide*, *spindle* and *fuel nozzle* and they are depicted in figure 4.21, 4.22 and 4.23 respectively.

The fuel nozzle is characterized by four orifices with a diameter of 1.05 mm. The nozzle holes are not tapered, meaning that the inlet diameter has the same dimension of the outlet diameter. In other words, the k-factor is equal to 0. As reported in the *Introduction*, in the *State of Art* section, this condition is favorable to cavitation. In fact, the section area decreases abruptly from the sac to the orifices and the same happens for the pressure, which could potentially drop under the saturation limit. With the aim of avoiding a tumultuous cavitation regime and its consequences in terms of erosion, the engineers designed spherical smooth entrance in two nozzle holes with a radius of 1.2 mm; in this way, the Carnot-Borda pressure losses are minimized. Lastly, the ratio between the length and the outlet diameter (L/D_o) is equal to 3 and 3.8 respectively for the two central and external holes. From this paragraph, the nozzle holes will be identified with the following notation, H1, H2, H3 and H4, as depicted in figure 4.23.

The CAD geometry is provided with some corrections to avoid problems due to small geometrical features and crevices. It is further simplified cutting off most of the upstream part of the spindle guide and spindle. In this way, the internal surface of the spindle guide and the external surface of the spindle are always in contact. In figure 4.24, a comparison

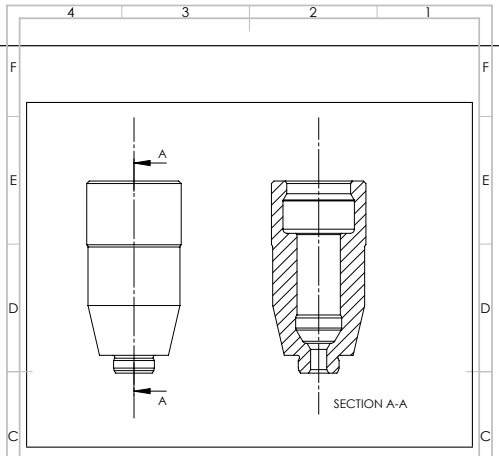

Figure 4.21: The spindle guide, the original geometry provided by MAN Energy Solutions.

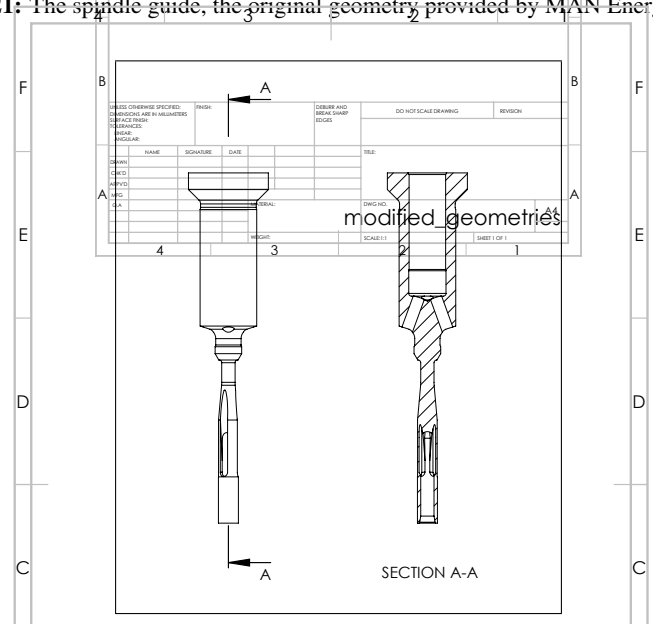

Figure 4.22: The spindle, the original geometry provided by MAN Energy Solutions.

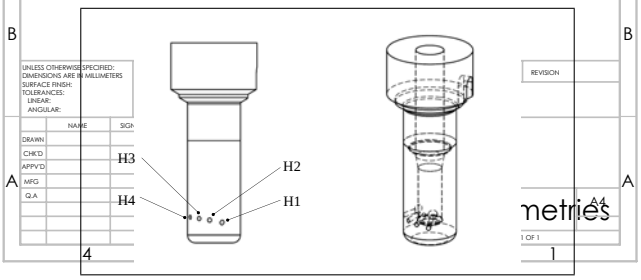

Figure 4.23: The fuel nozzle, the original geometry provided by MAN Energy Solutions. The nozzle holes are indicated with H1, H2, H3, H4 from right to left.

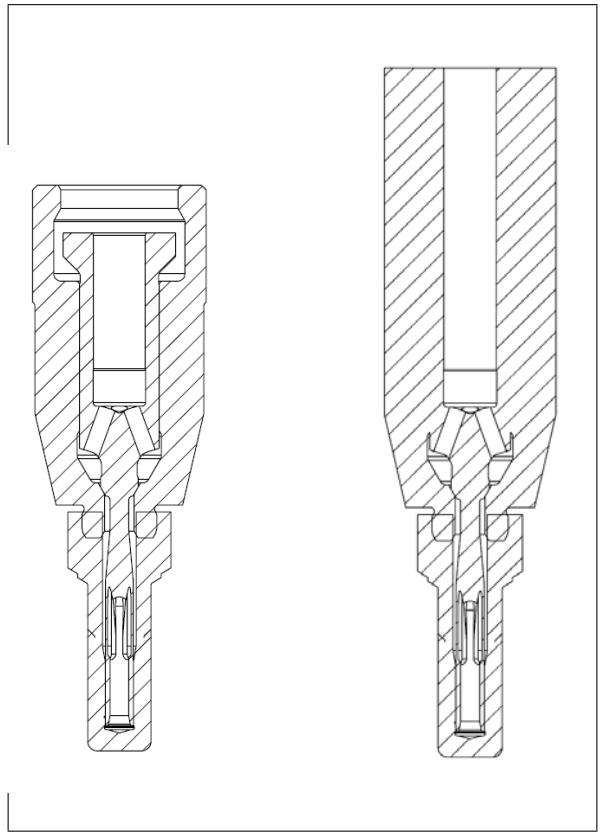

Figure 4.24: The original geometry of the assembly (*Left*) and its modified version (*Right*).

between the original assembly and the updated version is presented. Lastly, by means of the *Surface Repair Tool* integrated in the software, the inlet and outlet surfaces are defined.

Applying the *Outlet pressure* boundary condition directly on outlet surfaces (H1, H2, H3 and H4) might cause unrealistic flow and it might lead to divergence because it could influence the flow upstream. For this reason, as suggested by Gavaises et al. [21] and Andersen [5], expansion volumes of conical shape are created in CAD software (*Solidworks*, as *Loft volumes*) and imported in *STAR CCM+*. Special attention was given in the placement of the expansion volumes in the outlet surface of the nozzle holes. The geometry with the expansion volumes is presented in figure 4.25. In this picture, the fuel valve is completely open and the expansion volumes are depicted in orange. The inlet boundary is coloured in purple.

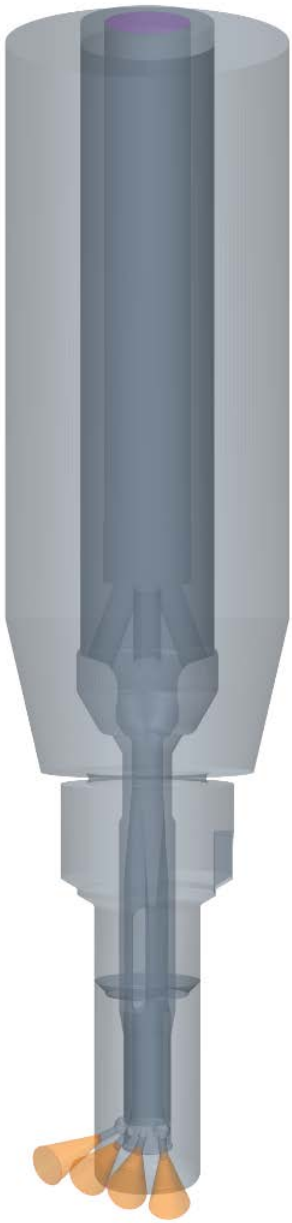

Figure 4.25: The geometry of the injector with expansion volumes (in orange). In this picture, the cut-off shaft is at full lift.

4.2.2 Mesh

The problem is a classic example of a multi-regions simulation; in fact, in total, there are six regions: the background, the overset and the four expansion volumes. Each region is meshed independently and interfaces are created in order to allow the exchange of information between the overset and the background and the background and the expansion volumes. The base size of the mesh of the background and the overset is set in order to respect the topological rule introduced in the *Theory* section and, at the same time, have a good resolution of the flow. The meshing process is crucial when the overset technique is applied: meshes of the overset and background must be homogeneous. This means that the base size of the cells in the background and overset must have (possibly) the same dimensions. In order to obtain a better match between the meshes, it is convenient to turn on the *alignment* option. This is feasible when the trimmer mesh is used, but not in case of a polyhedral mesh. Lastly, the user must consider that the prism layers' size must be comparable with the other cells of the domain. It should be mentioned that, because of the geometry of the injector, which counts of multiple small gaps, it is not easy to obtain a valid mesh configuration. In other words, it is not trivial that the algorithm recognizes correctly the acceptor cells in the background and overset regions. Therefore, quite a lot of time has been spent in achieving a valid mesh configuration.

	Polyhedral mesh	**Trimmer Mesh**
Number of cells *background*	3,228,113	12,212,455
Number of cells *overset*	3,082,333	3,624,468
Number of cells *expansors*	49,710	345,729
Total number of cells	6,360,156	16,182,652

Table 4.4: The proprieties of the meshes used in the single phase validation case

At the starting point of this validation case, the polyhedral mesh was selected; unfortunately, it was noted that the lack of alignment between the cells of the background and the overset produced "staircase" geometry during the opening and closing event. These inaccuracies might have an impact on the flow, especially on the pressure losses in the first milliseconds of the SOI. A wrong assessment of the pressure field might lead to an incorrect evaluation of the cavitation regime. For this reason, the same analysis is repeated using the trimmer mesh with alignment, to minimize the inaccuracies. Moreover, this procedure allows to study briefly whether the solution is mesh independent or not.

The first step of the meshing process consists in identifying the background volume. This is possible in *STAR CCM+* through the mesh option *surface wrapper* and selecting the volume of interest by means of a *seed point*. The mesh of the overset is obtained creating a new geometry part with the same shape of the spindle and using the Boolean operation *subtract*. In figure 4.26, the polyhedral and the trimmer mesh are depicted. In particular, the mesh of the background is in blue, while the mesh of the overset is in red. As it could be noted, the trimmer mesh present a refinement in the inlet section; this allows the algo-

rithm to select the active cells in the background with a better resolution, avoid ”scaling” geometries. Other refinements are in the region beneath the seat and in correspondence of the nozzle holes. In the same picture, the mesh just after the initialization is presented. In figure 4.27, portion of the background and the overset mesh are depicted around the spindle, in blue and in gray respectively. The mesh proprieties are summarized in table 4.4.

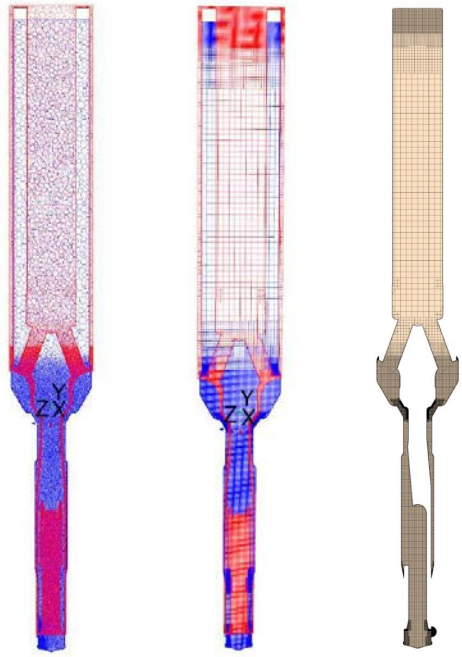

Figure 4.26: The polyhedral and the trimmer mesh, in red the overset, in blue the background when the fuel valve is full open. On the right the trimmer mesh after the initialization.

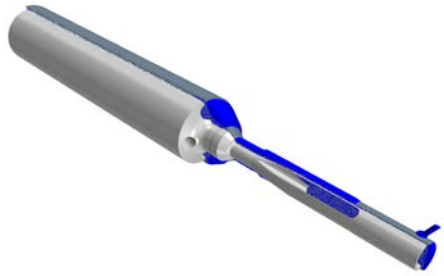

Figure 4.27: The spindle and a section of the background (in blue) and overset mesh (in gray)

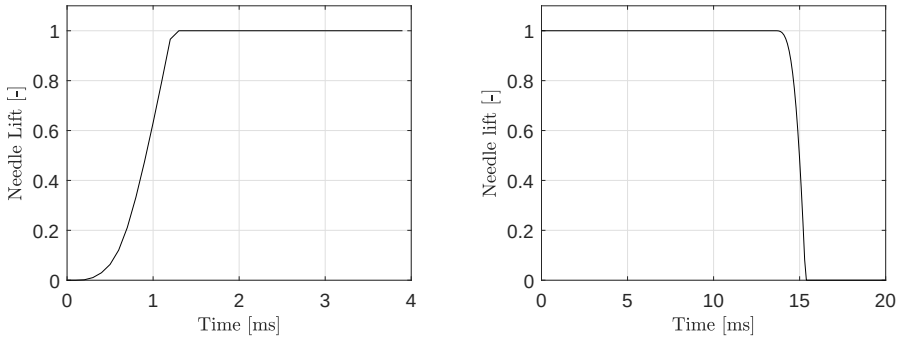

Figure 4.28: The displacement of the cut of shaft for the opening (*Left*) and closing (*Right*)

4.2.3 Physics

The solver is *Segregated Flow*, despite the cavitation model is disabled. The reason is that the multiphase flow will be considered in the next chapter and this solver is the only compatible with the *VOF* method.

It is expected that the fluid in the nozzle holes reaches high velocity, ideally around $0.3 \sim 0.4$ Mach. Accordingly, the compressability effects of the fuel must be taken into account. This is possible through the definition of a *User-defined equation of state* (EOS). With the assumption that the temperature remains constant in the injection process, there is not the need of an energy equation. In this case, the Userguide [45] suggests to use the EOS reported in eq. (4.13)[4]:

$$\rho = \rho_0 + \frac{p}{c^2} \tag{4.13}$$

where ρ_0 is the density of the fuel at the reference pressure. This equation is implemented in *STAR CCM+* through the *User-defined field function*:

```
$ (Density)=ρ0 + $(Pressure) / pow($ c,2)
```

Enabling the compressability option, the values for the following physical proprieties must be defined: density, derivative of the density with respect to pressure, dynamic viscosity, molecular weight and speed of sound. The density is defined through a *User field function* above, while the other values are taken from the Master thesis by Andersen [5], who retrieved the values from the American Oil Chemists' Society. They are presented in table 4.5.

	ρ_0 [kg m^{-3}]	dρ/dp [s^2 m^{-2}]	μ [Pa s]	W [g mol^{-1}]	c [m s^{-1}]
Diesel	836	5.65 10^{-7}	0.001672	170	1330

Table 4.5: Physical proprieties of Diesel

[4]The choice of this equation of state is commented in the Appendix

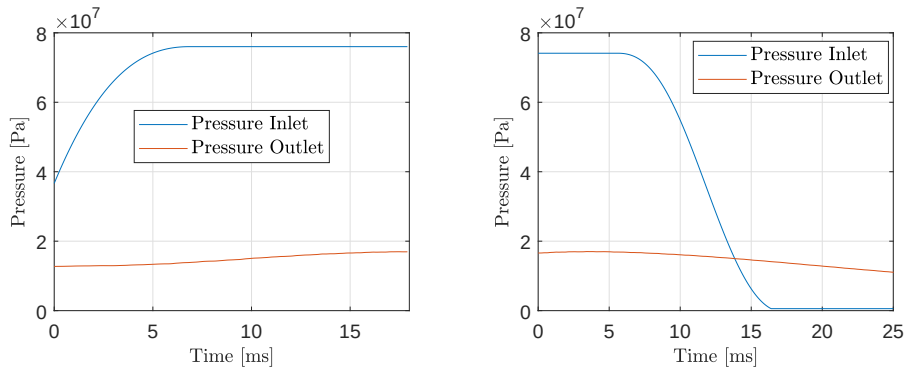

Figure 4.29: The inlet and outlet pressure at the SOI (*Left*) and EOI (*Right*)

The motion of the overset is possible through the option *Trajectory*. In particular, it is necessary to import in *STAR CCM+* a table with the coordinates x, y, z of the spindle with respect to time. These values are provided by MAN Energy Solution by means of the *1D-Hydcode*. The software automatically uses a linear interpolation to obtain a continuous function. The lift of the needle is presented in non dimensional coordinate ($x^*(t) = x(t)/x_{max}$) in figure 4.28 for the opening and closing event. Lastly, the turbulence model is the classic SST k-ω by Menter.

As regards the initial condition for the opening, the fluid is still and the pressure is given by a *User field function*. In particular, the pressure is equal to 366 bar in the section above the seat, while it is equal to 160 bar in the cells below the seat for the opening of the fuel valve. On the contrary, for the closing, the pressure is initialised assuming a constant value, 350 bar.

4.2.4 Boundary conditions

The unsteadiness of the flow is not only given by the motion of the cut-off shaft, but also by the transient pressure at the boundaries. The boundary condition chosen for the inlet surface is *stagnation pressure*, while for the outlet surface (faces of the expansion volumes) is *pressure outlet*. The numerical values are retrieved from *1D-Hydcode*. This code provides the pressure at the inlet of the high pressure pipe; the underlying assumption is that the pressure losses in the first components of the injector system are negligible. The plot of the pressure with respect to time at the inlet and outlet boundary is presented in figure 4.29 for the opening and closing events. The data are imported in *STAR CCM+* in *Tables* and they are interpolated through *User Field Functions*:

```
interpolateTable(@Table("Pres_In"),"Time",LINEAR,"Pressure",$Time)
interpolateTable(@Table("Pres_Out"),"Time",LINEAR,"Pressure",$Time)
```

Except the interfaces, all the other surfaces are considered *Wall*, where the no-slip condition is applied. The interface between the background and the overset is the *Zero Gap Overset Interface* with three cells layer at the boundary to treat the cell in the gap as

inactive, while the interfaces between the background and the expansors are *Internal Interfaces*.

4.2.5 Solver

The solver is *Segregated Flow* and the time discretization is *Euler Second Order*. The time step is changed during the simulation in order to have a trade-off between the time required to obtain a solution (the simulations are very CPU intensive) and the Courant number. In particular, the first milliseconds of the opening event were simulated considering a time step equal to 1 μs (Courant less than 15 in all the cells of the domain), and it was increased until 5μ in the further time interval.
The inner number of iteration is equal to 5; this value is chosen since it is observed that, for this value, the time derivative of the residuals is small enough. In the simulations, the default values for the under-relaxation factors need to be slightly decreased to avoid divergence. The option *Linear ramp* has been used both for the turbulence model and pressure solver.

4.2.6 Results

This section is aimed at presenting the most relevant results of the simulations. Let us start considering the start of injection event (the opening of the fuel valve); the end of injection event (the closing of the fuel valve) is reported in the following subsection.

The Start of Injection

The first parameter which deserves special attention is the mass flow. In fact, on the engineering point of view, it essential to know the amount of fuel diesel injected in the combustion chamber, in order to predict correctly the stoichiometric ratio air/fuel and, consequently, the performance of the engine. The mass flow per each of the four holes of the injector is calculated using eq. (4.14) and the pre-built functions in *STAR CCM+*:

$$\int_{A_{H_i}} \rho(\boldsymbol{u} \cdot \boldsymbol{n}) \mathrm{d}A \tag{4.14}$$

The results in terms of the mass flows through each of the holes of the injector are depicted in figure 4.30 and 4.31 for the polyhedral and trimmer meshes. Additionally, the total mass flow is calculated and plotted in figure 4.32, where the benchmark values from the *1D-Hydcode* are reported too. It is important to underline that, in the one dimensional code used as reference, the displacement of the spindle is the result of the forces acting on it. On the contrary, the motion of the spindle is prescribed in the numerical simulation; in other words, the output of *1D-Hydcode* is used as an input in the CFD model. This has a large implication on the results which will be commented in the *Discussion* section. Lastly, it should be mentioned that the 50% of the displacement of the needle does not cause the uncovering of the nozzle holes, this is the reason why a time-span of around 1 ms is needed to allow the flow.

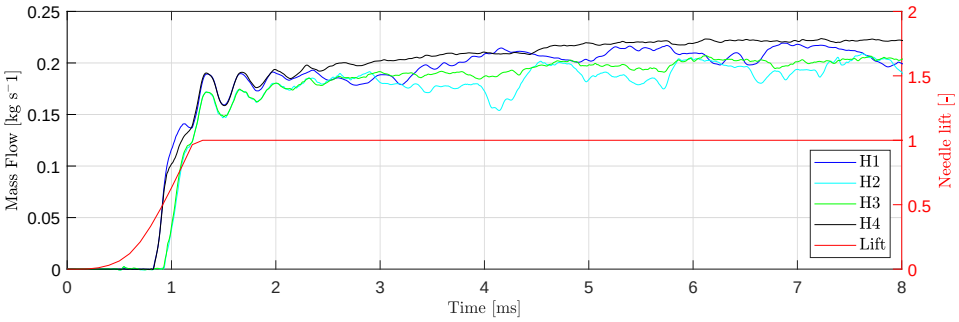

Figure 4.30: The mass flow per each of the nozzle holes; results from the polyhedral mesh.

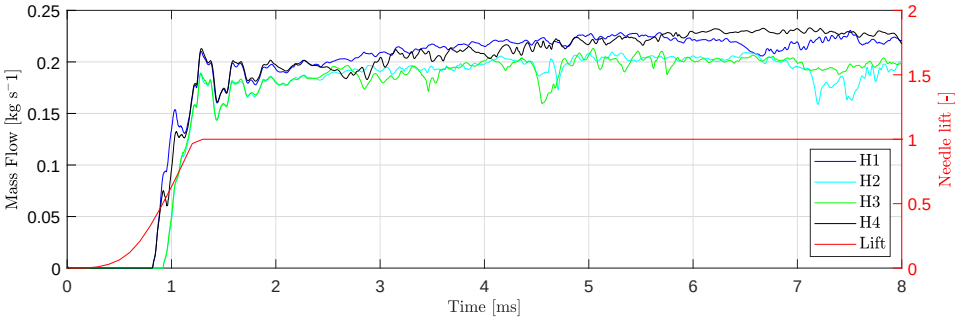

Figure 4.31: The mass flow per each of the nozzle hole; results from the trimmer mesh with alignment.

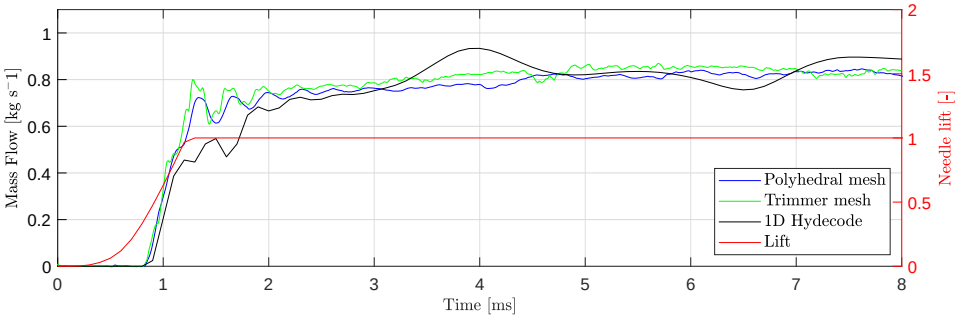

Figure 4.32: Total mass flow for the two meshes (in blue and green) and the reference values from *1D-Hydcode* (in black).

The displacement law of the spindle in figure 4.28 looks similar to the Heaviside step function, being the opening of the fuel valve extremely fast. In addition, the Dirichlet conditions at the boundaries, the pressure difference between the fluid above and below the seat and the compressability of the diesel fuel cause a pressure wave. The sudden opening of a valve has been widely studied for simple geometries; a good reference is the Benson's work [9]. With the aim of detecting the pressure wave, two *point probes* are placed at the two ends of the injector: in the sac volume and close to the inlet surface. They measure the variation of pressure in time. In this section, the time evolution of the signal recorded by the *point probe* located in the sac is presented. In particular, in figure 4.33, there are the plots in time and frequency domain. The plots of the *point probe* located in the inlet are here omitted, but the reader could refer to 6.1, 6.2 and 6.3 in the Appendix.

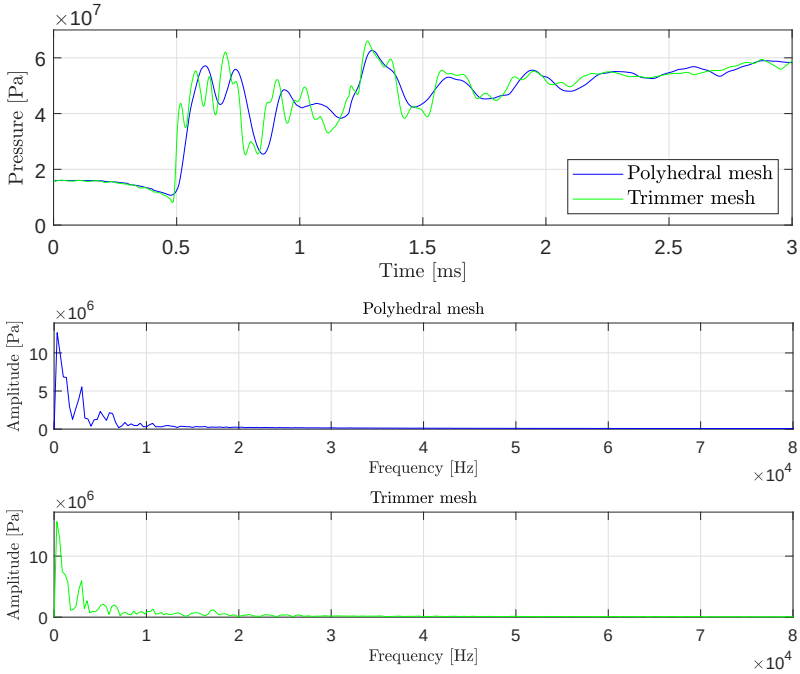

Figure 4.33: Pressure recorded by the *Point probe* located in the sac; evolution of the signal in time and in the frequency domain. The first peak in the spectral analysis is due to the increase of the pressure in the boundary, while it is believed that the second peak is due to the pressure fluctuations induced by the pressure wave.

In the context of diesel injectors, it is relevant to keep track of the momentum flux. In fact, as reported by Payri et al. [41], this quantity gives the magnitude of the mixing potential of the injection process. Indeed, it is responsible for the spray penetration, the cone angle and the air entrainment. The momentum is a vectorial quantity defined as:

$$\boldsymbol{M} = \rho \boldsymbol{u} \tag{4.15}$$

In this study, the momentum flow is calculated as:

$$\dot{M} = \int_{A_{H_i}} \rho |(\boldsymbol{u} \cdot \boldsymbol{n})\boldsymbol{u}| \mathrm{d}A \tag{4.16}$$

The plot of the magnitude of the momentum flow is depicted in figure 4.34 and 4.35 for the polyhedral and trimmer mesh.

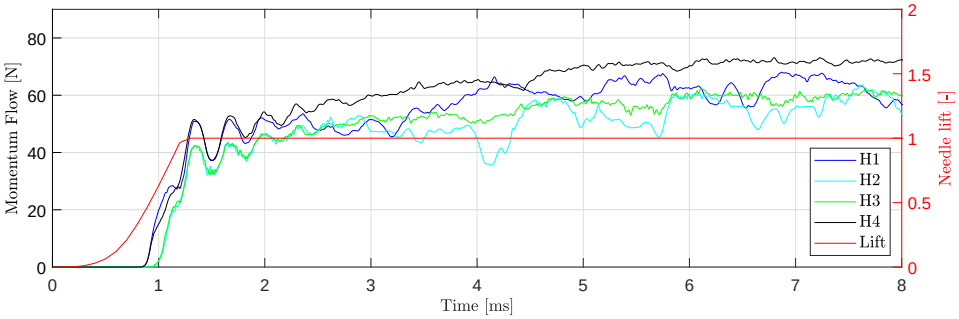

Figure 4.34: The momentum flow per each of the nozzle hole; results from the polyhedral mesh.

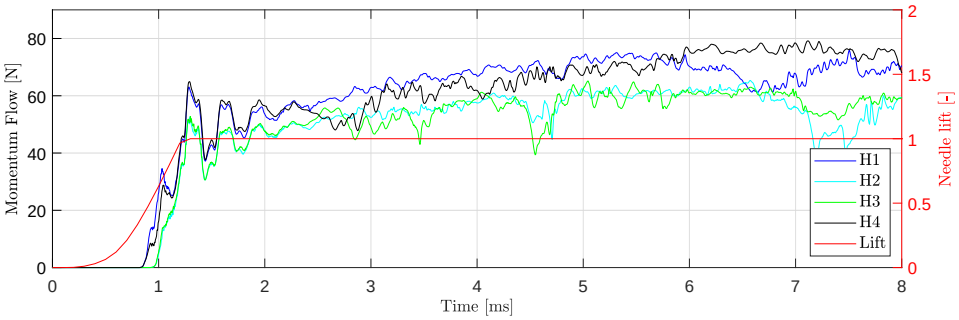

Figure 4.35: The momentum flow per each of the nozzle hole; results from the trimmer mesh.

Note that the momentum flow has the dimension of a force; thus, it could be evaluated experimentally, measuring, for instance, the force generated on a target surface placed in the first millimeters of the jet. Unfortunately, benchmark values for the momentum flow were not provided.
In the analysis, special attention is reserved for the velocity and pressure field. In fact, they might return useful information for the future analysis, when the cavitation model will be enabled. This is particularly true for the pressure field: the location where it reaches lower values, the nucleation and growth of vapor bubbles is expected. The pressure and the velocity field in six time steps during the opening event are depicted from figure 4.36 to figure 4.43 for the four nozzle holes.

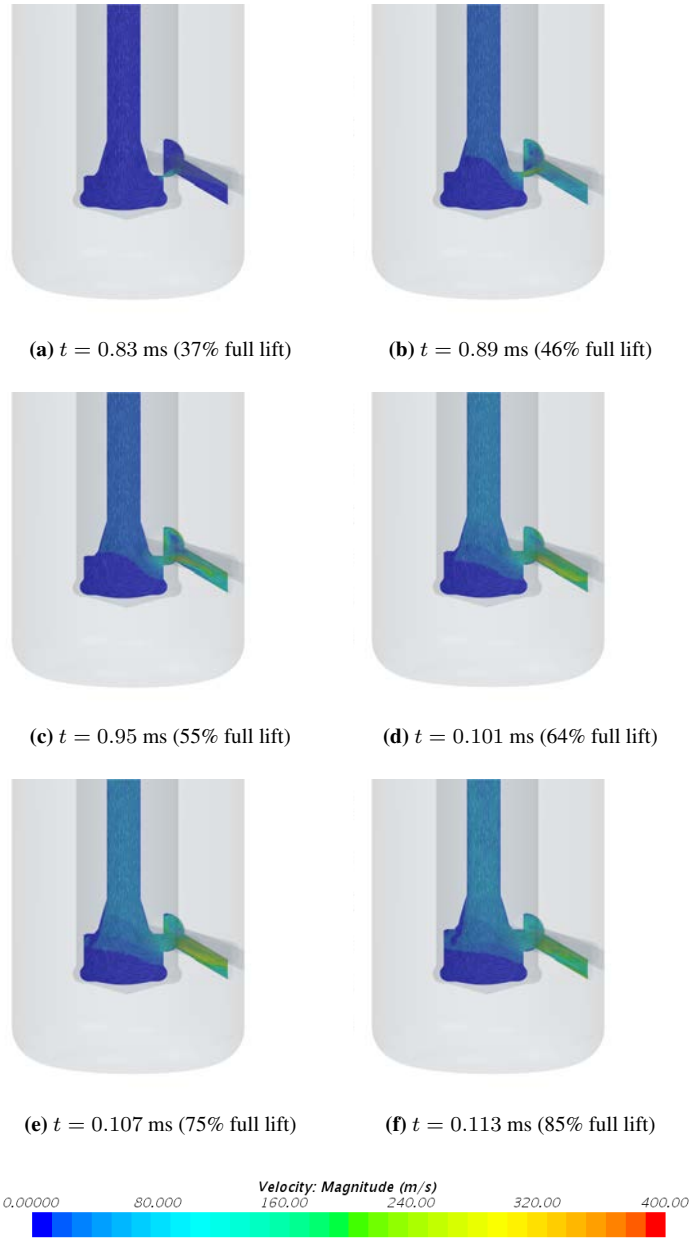

(a) $t = 0.83$ ms (37% full lift)

(b) $t = 0.89$ ms (46% full lift)

(c) $t = 0.95$ ms (55% full lift)

(d) $t = 0.101$ ms (64% full lift)

(e) $t = 0.107$ ms (75% full lift)

(f) $t = 0.113$ ms (85% full lift)

Figure 4.36: Velocity field (integral convolution) in a section of hole H1 at the opening of the fuel valve.

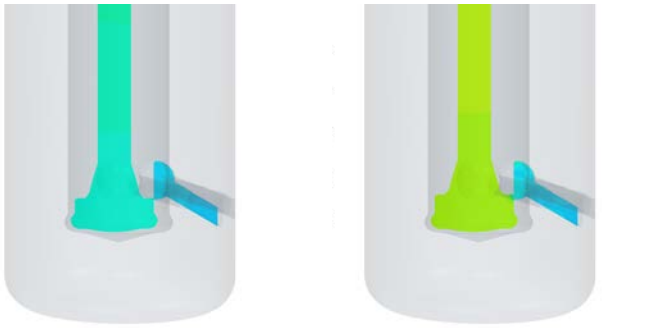

(a) $t = 0.83$ ms (37% full lift)

(b) $t = 0.89$ ms (46% full lift)

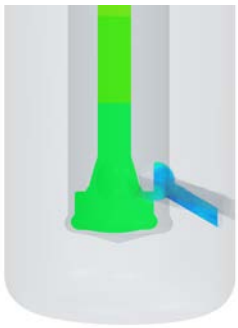

(c) $t = 0.95$ ms (55% full lift)

(d) $t = 0.101$ ms (64% full lift)

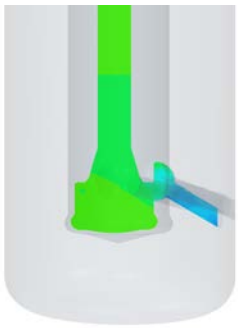

(e) $t = 0.107$ ms (75% full lift)

(f) $t = 0.115$ ms (85% full lift)

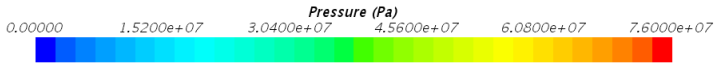

Figure 4.37: Pressure field in a section of hole H1 at the opening of the fuel valve.

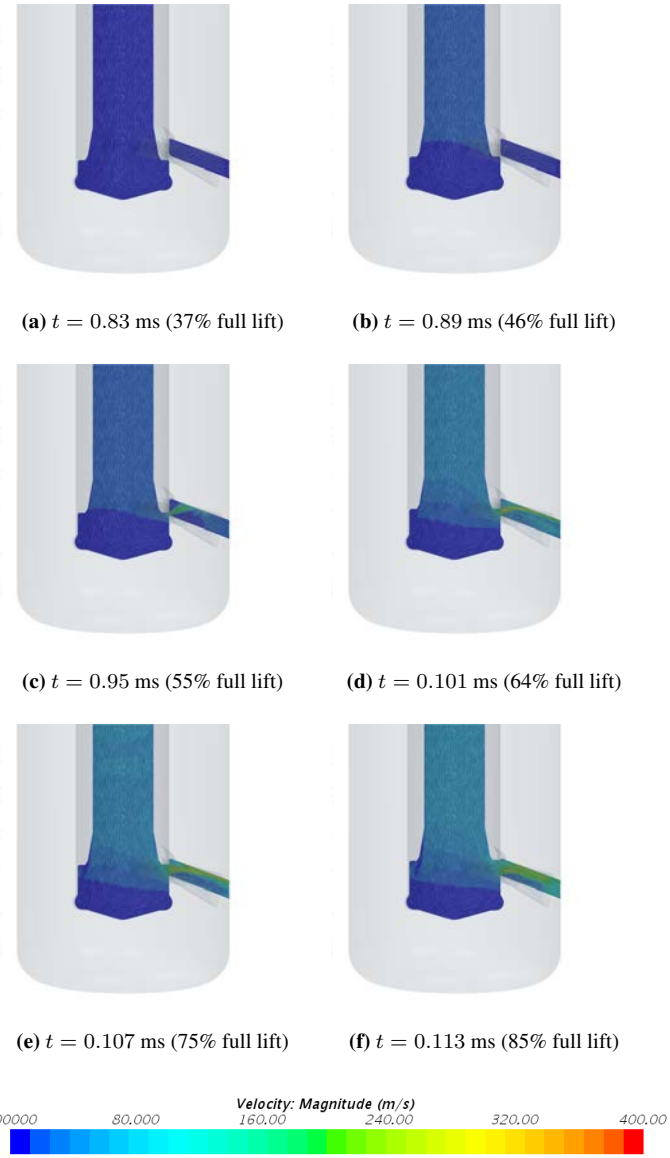

(a) $t = 0.83$ ms (37% full lift)

(b) $t = 0.89$ ms (46% full lift)

(c) $t = 0.95$ ms (55% full lift)

(d) $t = 0.101$ ms (64% full lift)

(e) $t = 0.107$ ms (75% full lift)

(f) $t = 0.113$ ms (85% full lift)

Figure 4.38: Velocity field (integral convolution) in a section of hole H2 at the opening of the fuel valve

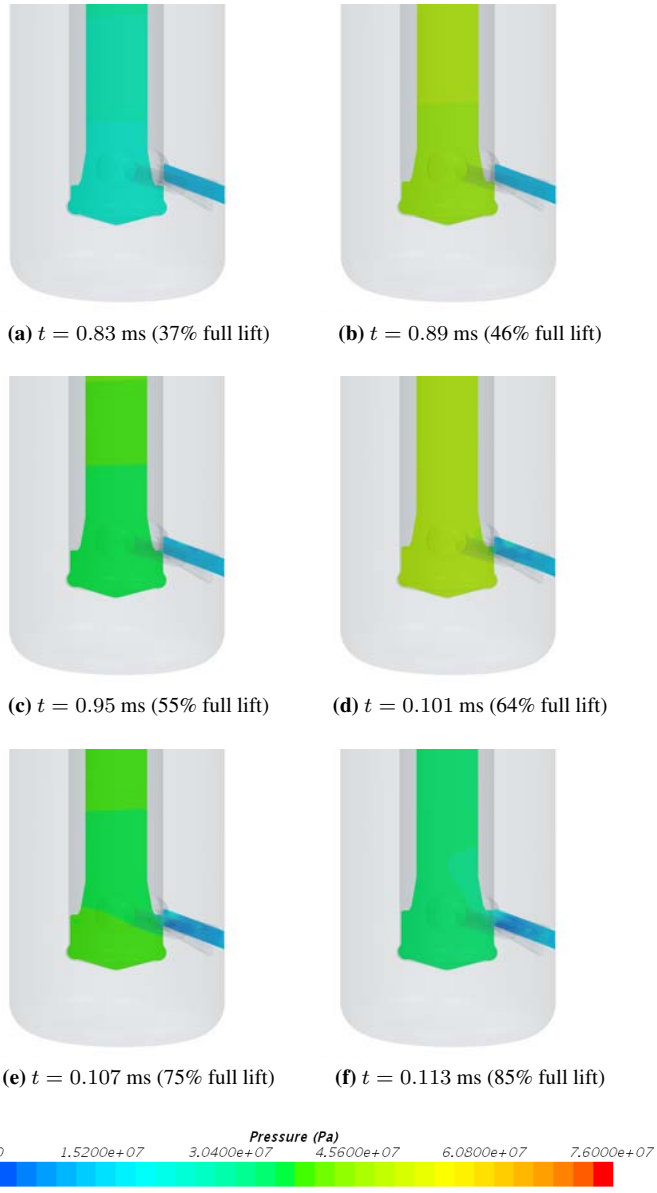

(a) $t = 0.83$ ms (37% full lift) **(b)** $t = 0.89$ ms (46% full lift)

(c) $t = 0.95$ ms (55% full lift) **(d)** $t = 0.101$ ms (64% full lift)

(e) $t = 0.107$ ms (75% full lift) **(f)** $t = 0.113$ ms (85% full lift)

Figure 4.39: Pressure field in a section of hole H2 at the opening of the fuel valve.

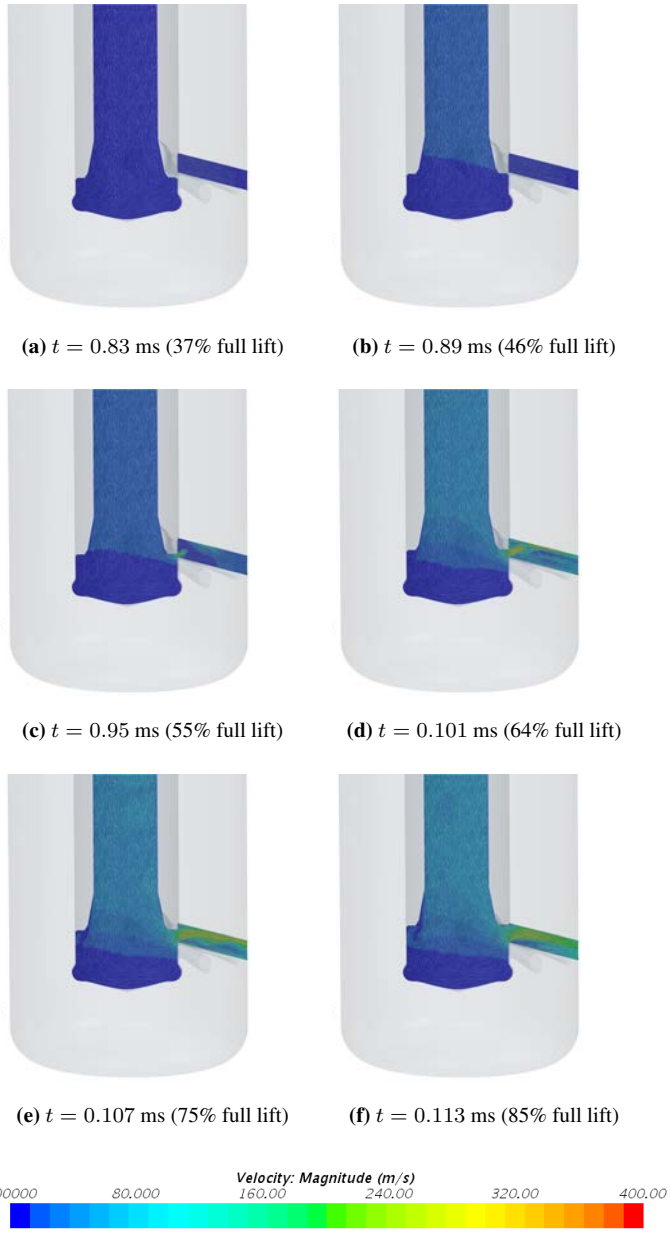

(a) $t = 0.83$ ms (37% full lift)

(b) $t = 0.89$ ms (46% full lift)

(c) $t = 0.95$ ms (55% full lift)

(d) $t = 0.101$ ms (64% full lift)

(e) $t = 0.107$ ms (75% full lift)

(f) $t = 0.113$ ms (85% full lift)

Figure 4.40: Velocity field (integral convolution) in a section of hole H3 at the opening of the fuel valve.

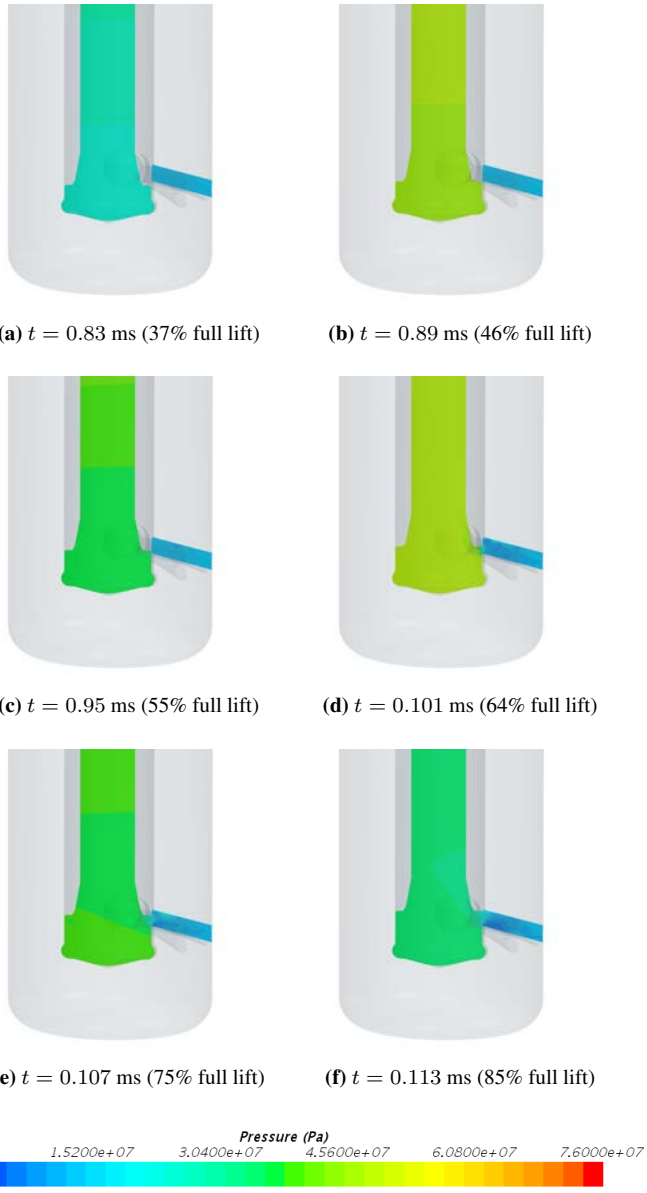

(a) $t = 0.83$ ms (37% full lift) **(b)** $t = 0.89$ ms (46% full lift)

(c) $t = 0.95$ ms (55% full lift) **(d)** $t = 0.101$ ms (64% full lift)

(e) $t = 0.107$ ms (75% full lift) **(f)** $t = 0.113$ ms (85% full lift)

Figure 4.41: Pressure field in a section of hole H3 at the opening of the fuel valve.

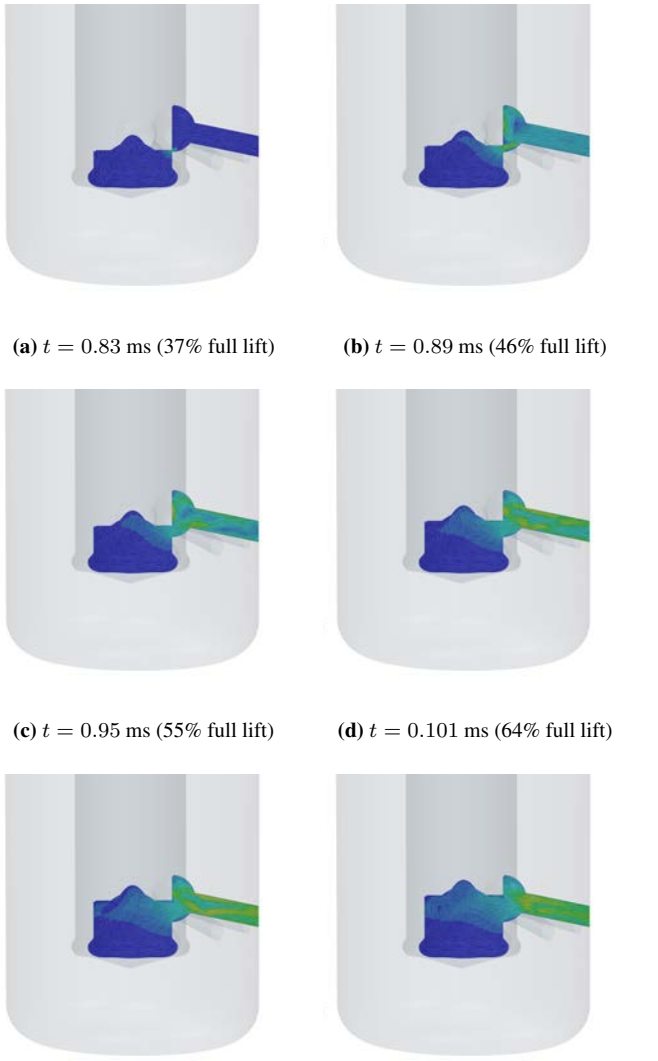

(a) $t = 0.83$ ms (37% full lift)

(b) $t = 0.89$ ms (46% full lift)

(c) $t = 0.95$ ms (55% full lift)

(d) $t = 0.101$ ms (64% full lift)

(e) $t = 0.107$ ms (75% full lift)

(f) $t = 0.113$ ms (85% full lift)

Figure 4.42: Velocity field (integral convolution) in a section of hole H4 at the opening of the fuel valve.

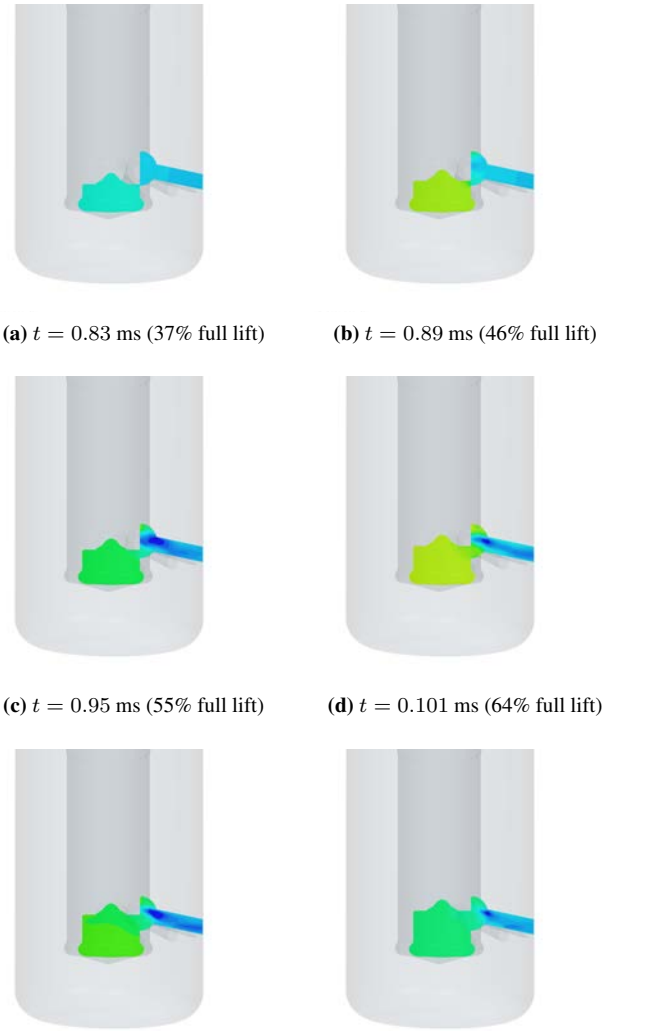

(a) $t = 0.83$ ms (37% full lift) **(b)** $t = 0.89$ ms (46% full lift)

(c) $t = 0.95$ ms (55% full lift) **(d)** $t = 0.101$ ms (64% full lift)

(e) $t = 0.107$ ms (75% full lift) **(f)** $t = 0.113$ ms (85% full lift)

Figure 4.43: Pressure field in a section of hole H4 at the opening of the fuel valve. It is interesting to note a large vortex which is generated at the entrance of the nozzle hole.

It should be mentioned that the above-reported results were obtained limiting the absolute pressure to 0 Pa for the *Segregated solver*. A paragraph concerning this limitation is dedicated in the *Discussion*.

The streamlines are depicted in picture 4.44, at the end of the opening ($t = 1.8$ ms) and zooming on the sac volume. As it will be discussed in the following section, the streamlines show the presence of a large re-circulation region in the sac. It is believed that it is responsible for the mass flow fluctuations once that the quasi-steady condition has been achieved.

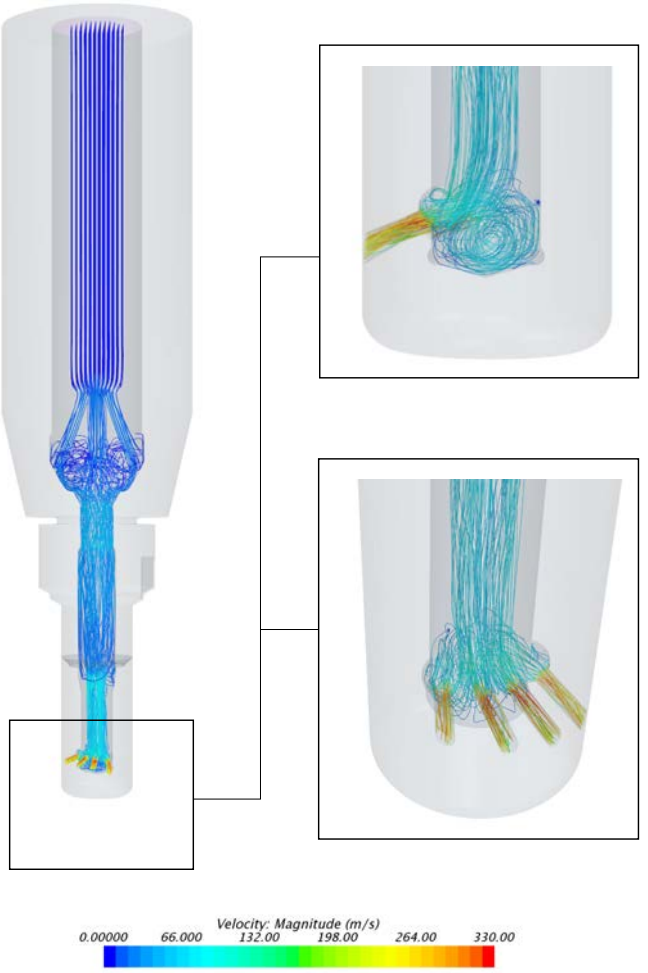

Figure 4.44: Streamlines at the end of the opening event ($t = 1.8$ ms)

The End of Injection

The study of the end of injection is performed using the polyhedral and trimmer mesh, in a similar way of what has been done for the start of injection. The EOI differs from the SOI because it is necessary to reach the quasi-steady condition before the cut-off shaft starts its motion. For this reason, in the first 13 ms the valve is at full lift and the flow has time to develop and evolve due to the time dependant pressure at the boundaries. The mass flow through the orifices is reported in figure 4.45 and 4.46, respectively for the polyhedral and the trimmer mesh. In figure 4.47, the total mass flow is calculated and it is compared with the data from the *1D-Hydcode*. The plots of the momentum flow are here omitted, but the reader could refer to the Appendix.

The reader might note that, at time-step 14 ms, the flow reverse; the mass flows through the four nozzle holes change sign and become negative. It is the moment when the pressure at the inlet starts to be lower than the pressure at the outlet (refer to figure 4.29). Negative mass flows are not realistic and they might be caused by the misalignment between the hypotheses of the CFD simulation and the *1D-Hydcode*, as it will be commented later in the *Discussion* subsection.

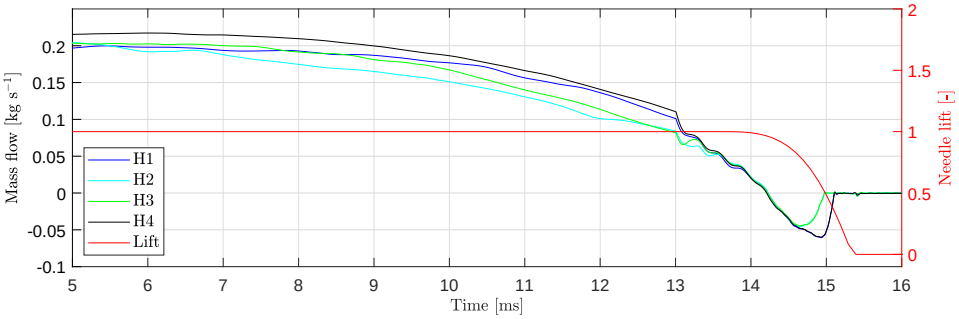

Figure 4.45: The mass flow per each of the nozzle hole; results from the polyhedral mesh.

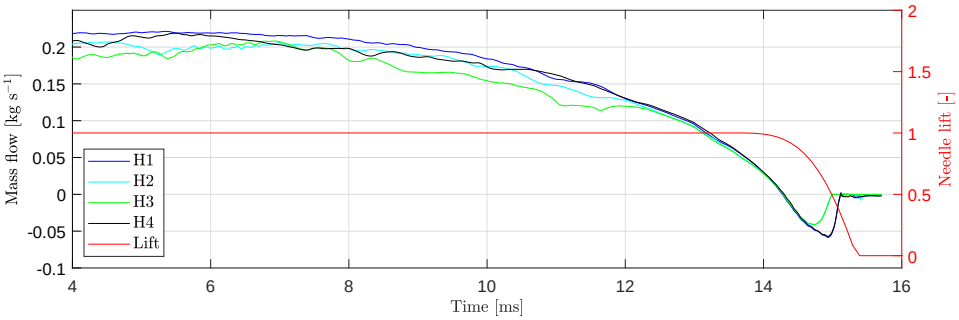

Figure 4.46: The mass flow per each of the nozzle hole; results from the trimmer mesh.

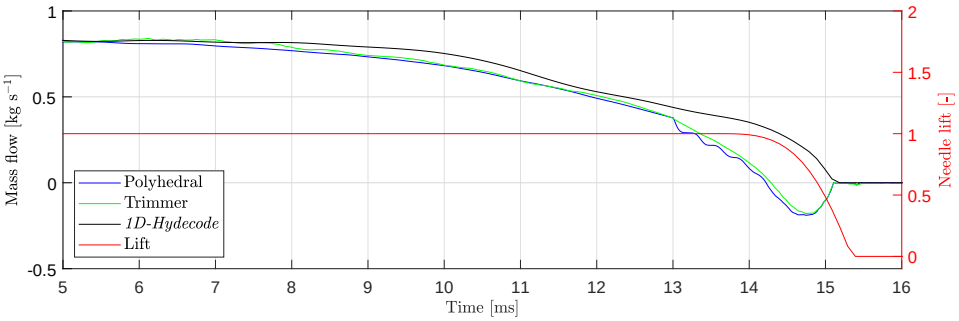

Figure 4.47: Total mass flow for the two meshes (in blue and green) and reference values from *1D-Hydcode*.

4.2.7 Discussion

Starting from the analysis of the SOI, the first milliseconds of the injection event are correctly detected through the use of the *Zero Gap Overset Interface*. It is worthwhile to mention that the nozzle holes are not uncovered by the spindle simultaneously: H1 and H4 are the first to be disclosed. The results of the mass flow show a satisfying agreement with the output of the *1D-Hydcode*, despite the model are based on different hypotheses. The difference in mass flow between the CFD simulations and the *1D-Hydcode* is reported in figure 4.48. The maximum difference takes place in the first millisecond the SOI and it is around 0.35 kg/s. The high error and the periodicity might be attributed to misaligned assumptions between the CFD simulations and *1D-Hydcode*. Let us recall that the *1D-Hydcode* implements the one dimensional Navier-Stokes equation and it deals with the entire injection system, from the high pressure pipe to the nozzle holes. In addition, being the model one dimensional, the EDM geometries of the actual injector are not modelled in the code. The main consequence is that the length of the injector is very different compared to the one in the CFD simulation, and this affects the frequency of the pressure wave. This explains the peaks in figure 4.48: they are due to the phase displacement of the pressure waves. As reported in the *Recommendations for the Future* section, one idea to improve the model consists in coupling the code *1D-Hydcode* and *STAR CCM+*; this allows to get the actual dynamics of the system without the need modelling and importing complex (and CPU intensive because of their extension) geometries in *STAR CCM+*.

It is interesting to evaluate the frequency of the pressure wave detected by the *point probes* and compare its value with the one given by the theory, considering the portion of the injector which is simulated. The speed of sound in diesel is equal to 1330 m/s and the injector has approximately an internal length of 20 cm. Under these assumptions, the time required by the pressure wave to travel back and forth through the system is equal to 0.3 ms, leading to a frequency of 3300 Hz. This value is in agreement with the frequency recorded by the probes placed in the inlet and sac. The numerical values of the frequency recorded in the CFD simulations are summarized in table 4.6.

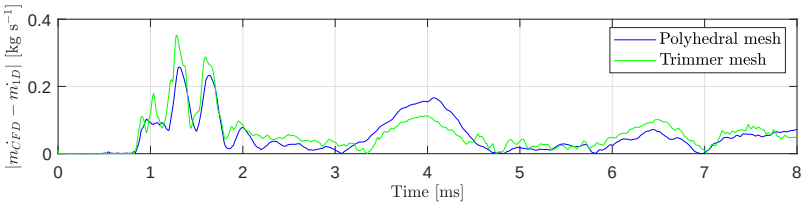

Figure 4.48: The error between the mass flow from the CFD simulations and *1D-Hydcode*.

	Point probe in sac [Hz]	**Point probe inlet [Hz]**
Polyhedral mesh	3,000	3,300
Trimmer mesh with alignment	2,975	3,300

Table 4.6: The frequency of the pressure fluctuations recorded by the probes.

Lastly, the pressure in the sac volume matches well the value reported by the one dimensional code, once that the steady condition has been reached, around 700 bar. A plot of the pressure in the sac volume is presented in figure 4.49. The pressure fluctuations in the first 3 ms are mainly due to the pressure wave, while in the following milliseconds, it is believed that they are due to the motion of a vortex in the sac volume. A simplified analysis about the amplitude of the pressure fluctuations due to pressure pulse is performed using the Allievi-Michaud' formula. This equation was obtained for simpler geometry (piping system) but, as a first approximation, it might be used also for this case. The pressure fluctuations are equal to:

$$\Delta p = \frac{2\rho L u}{T_c} \approx 50 \text{ bar} \tag{4.17}$$

where L is the length of the portion of the injector above the seat, u is the velocity once that the seat is at full lift and T_c is the time require for the opening/closing of the valve. The value of 50 bar is in agreement with the observed value. This analysis permit to conclude that cavitation should not occur as a consequence of the pressure pulse travelling in the system[5].

From the analysis of the streamlines a large vortex is observed in the sac volume when the valve is completely open. The re-circulation region is a consequence of the 90° angle between the flow upstream and the nozzle holes. The vortex is observed by Andersen [5] and Gavaises et al. [21] too when they analysed the slide fuel valve in steady conditions. It is believed that the re-circulation region is responsible for the fluctuations of the mass and momentum flow thought the nozzle holes. The time evolution of the vortical structure might be observed in figure 4.50; in the first milliseconds after the disclosure of the nozzle holes, the core line of the vortex is orthogonal to the axis of the nozzle hole, while it changes orientation when the flow has developed. In this situation, it might be noted that the vortex core is aligned with the axis of H2 and H3, where the swirling flow is evident

[5]This mechanism is known as *acoustic cavitation*; it is common for large pressure fluctuations, for instance, in case of water hammer.

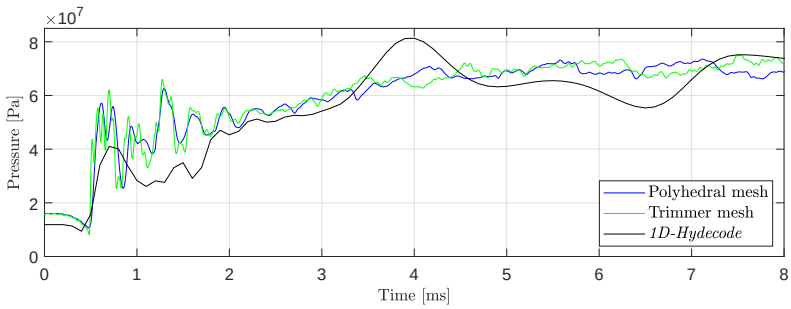

Figure 4.49: Pressure recorded in the sac volume by the *point probe*.

through the observation of the streamlines. This explains the larger amplitude fluctuations in these nozzle holes compared to H1 and H4.

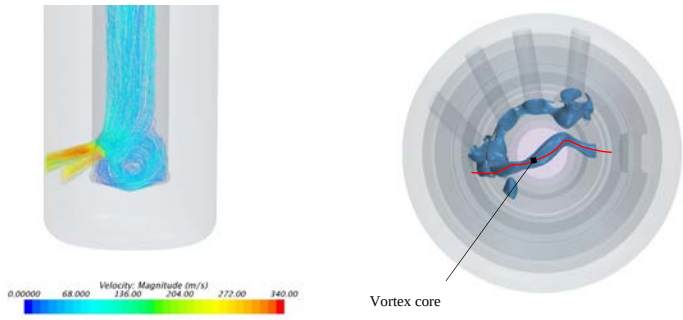

(a) Vortex core at the end of the opening event ($t = 1.8$ ms)

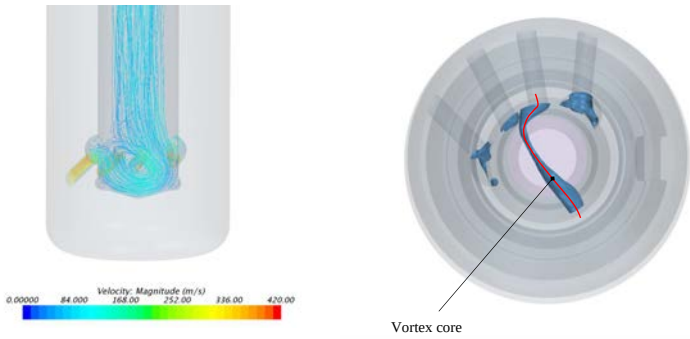

(b) Vortex core once that the flow has developed ($t = 8$ ms)

Figure 4.50: The vortex core location depicted through iso-surface of the pressure field.

From the comparison between the results from the polyhedral and the trimmer mesh, the variation in pecentage of the mass and momentum flow is small. For instance, the variation in the pressure measured in the sac when the quasi-steady condition is reached is approximately equal to 5% on its maximum. This brief analysis allows to demonstrate that the solution is mesh independent. Regardless that, the trimmer mesh should be preferred in the following analysis because it is optimized to be used with the overset technology. In fact, the presence of the above mentioned "scaling" geometries is minimized.

In the project plan of this thesis, a section about the effects of the interpolation option in the overset was programmed. It was relevant to check the difference in the mass flow depending on what interpolation scheme is used. Incidentally, on the engineering point of view, it is essential that the simulation predicts correctly the amount of fuel discharged by the nozzle holes since it influences the performance of the engine. From a first study of the Userguide, it seemed that the continuity was automatically fulfilled by the software through the implementation of corrective algorithm, especially when the *Segregated solver* was used. The above mentioned analysis was then pointless. Through further investigation, it was discovered that the mass continuity is enforced only if the user ticks an option in the *Continua* window. Unfortunately, the time was too little to perform all the analyses again, but a quick assessment of the difference is performed. The residuals from the simulation run without taking special care of the continuity converges at 10^{-3}, while, enforcing continuity, residuals are around 10^{-6}. The error was already very close to be negligible (in general the threshold 10^{-4} is used in CFD), but, of course, the second solution must be preferred. For further studies with the overset and the *Segregated solver*, it is advisable to enforce the continuity using the *Flux correction method*, in case of compressible flow. For incompressible flow, the user might choose the *Source correction method*.

As concern the closing event (EOI), the mass flow from the CFD simulation looks quite different from the benchmark. It might be explained as the consequence of the assumptions used in the CFD model. In fact, the CFD model uses some of the outputs of the *1D-Hydcode*, which are based on the 1D Navier-Stokes equation and on a different geometry. In addition to that, it is possible that the *1D-Hydcode* does not evaluate correctly the motion of the cut-off shaft since the three dimensional geometrical features are not reproduced. Being the displacement of the fuel valve prescribed in the CFD simulation, there is an error propagation through the different models.

It should be pointed out that the residual have a magnitude of 10^{-3} for the continuity and momentum equations. This value is slight larger than the threshold of 10^{-4} which is often used to evaluate the convergence of a solution. Anyways, the history of the residuals shows a monotonically decreasing curve, which is perfectly fine. The term responsible for the production of the turbulent kinetic energy shows this behaviour too. On the contrary, the residuals for the rate of dissipation (abbreviated as *Sdr* in *STAR CCM+*) are high (but they do not diverge) and the function is not monotonic when it is evaluated in the range of the inner iterations. It is believed it is due to the lack of prism layers in the mesh. In fact, from the basics of the turbulence theory [36], the energy dissipation is large near the wall, for small values of $y+$. The presence of the prism layers is in conflict with the need

of having an homogeneous mesh for the overset, and this might lead to the high residual. Another aspect which is worth being investigated is the initial condition for the turbulence quantities; in the simulation the default *STAR CCM+* initial condition for turbulence intensity and velocity are used, but they might not be the optimal choice. Again, the lack of experimental data makes this assessment very difficult and it is hard to set the actual initial conditions for the turbulence quantities. A simulation with fixed valve and trimmer mesh with alignment returned the same results in term of residuals; therefore it seems that the overset is not part of the problem. As it will be discussed further in the next chapter, it might be advisable to have a tighter mesh for the overset and reduce the mesh size and have a better resolution of the flow.

The last consideration is about the pressure limit for the *Segregated solver*, under the option *minimum allowable absolute pressure*. By default, the value is set equal to 1000 Pa, but it was decreased to 0 Pa. The question which might arise is the following: could this value be negative? On one side, the answer is yes; liquid in metastable condition can withstand negative pressure. In this regard, the link between the mechanic and thermodynamic definition of pressure is worth being explained. On the mechanical point of view, a negative pressure simply refers to tension status. In thermodynamics, pressure is the force per unit of area generated by the molecules in a control volume, and it is defined as:

$$p = \frac{1}{2}\rho < u^2 > \tag{4.18}$$

where $< u^2 >$ is average velocity of the molecules in the domain. Accordingly, the pressure from eq. (4.18) can not be negative. At this point, it is important to recall the most relevant hypothesis of the eq. (4.18): the equilibrium. Equilibrium means that the inter-molecular forces could be neglected, with exception of the forces generated from the collisions between the molecules. Therefore, it makes sense to talk about negative pressure when the liquid is in a metastable condition, meaning that the inter-molecular forces have an impact. Cavitating liquid might be in a metastable condition, depending on temperature and density condition. *Steve*, the online user portal of *STAR CCM+*, reports an experiment where cavitating water under certain condition of temperature and purity can withstand a tension of 10^7 Pa.[6]. All this to say that the limitation in the *Segregated solver* might not reflect the real physics, especially when the cavitation model will be activated in the next chapter. On the other hand, the cavitation models implemented in *STAR CCM+* are based on the pre-existing bubble having a minimum diameter (the *seed diameter*) and a pressure equal to the saturation limit. Therefore, the pressure in the liquid should only be positive, and negative values are unwanted effects due to the modelling. It should also be reported that the tutorial about cavitation in the Userguide [45] does not mention to change the default value of the *minimum allowable absolute pressure*.

4.2.8 Conclusion

The test case about the single phase flow through the injector allowed to validate the motion of the cut-off shaft through the overset technique and the following conclusion might be drawn:

[6]The difference in pressure between the saturation limit and the actual pressure is known as *static delay*

- The CFD simulation of the SOI shows a satisfying agreement with the one dimensional code *1D-Hydcode*. The main source of the error is due to misaligned assumptions between the CFD simulation and *1D-Hydcode*.

- A pressure wave is expected at the opening of the fuel valve. Its frequency and amplitude is in line with the theoretical value but it differs from the *1D-Hydcode*. The difference can be attributed to the model of the injectors used in the two tools.

- A large re-circulation region forms in the sac volume. The vortex core changes orientation during the opening event and, once that the quasi-steady condition are reached, it is aligned with the nozzle holes H2 and H3. This affects the mass flow through these nozzle holes, and large fluctuations are observed.

- The overset technique is a powerful tool to simulate the motion in CFD, through the use of multiple superimposed grids. The mass conservation is always satisfied when the appropriate option is ticked and the use of different interpolation options lead to the same solution. Stability and time are affected by the choice of the interpolation option.

- The dynamics of the closing event (EOI) appears quite different from the data of the *1D-Hydcode*, in particular it is observed that the flow reverse before the cut-off shaft covers the orifices. It is due to the superimposition of the motion of the cut-off shaft in the CFD simulation. Being *1D-Hydcode* one dimensional and neglecting the EDM geometries, it does not reproduce the physics correctly. This affects the reliability of the CFD simulation.

- The history and the values of the residuals for the continuity and Navier-Stokes equations are acceptable, but the residuals for the turbulent dissipation rate are large. It is suspected it is due to the mesh, which lacks prism layers to fulfill the need of having comparable sizes between background and overset meshes, and the non-optimal initial condition for the turbulent quantities.

Chapter 5

The injector in operative condition

The previous test cases allowed to gain confidence with the unsteadiness of the cavitating flow and the motion of the cut-off shaft. It is time to combine the elements of the past validation cases to study the in-nozzle flow in real operating conditions. Before going into details of the transient simulation, it is worthwhile to test the behaviour of the injector with the valve partially open and constant pressure at the boundary. The study of injectors at partial lift and steady conditions is very popular in literature, and some authors (Salvador et al. [19]) reported that it is representative of the actual transient injection process. Indeed, they wrote that the difference in terms of the mass flow, momentum flux and cavitation morphology is very small (around 3%) in comparison with the moving valve. This statement is worth being tested; in fact, it is believed that there must be a difference between the simulation in steady condition, where the flow has the time to develop, and the transient simulation where the time scale is very small. In conclusion, these tests will provide suggestions to assess and review the results from the transient cavitating simulation.

5.1 Steady conditions

Three tests are conducted in steady conditions, two of them with partial lift valve while the third one with full lift valve. Only in the latter case, the results can be compared with data provided by MAN Energy Solutions. In table 5.1, the displacement of the cut-off shaft are reported, as well as the pressure at the boundaries.

	Displacement from the seat [mm]	**Percent opening**	**Pressure inlet**	**Pressure Outlet**
Case A	1.5	55%	495 bar	128 bar
Case B	2	75%	500 bar	128 bar
Case C	2.7	100%	760 bar	170 bar

Table 5.1: Position of the cut-off shaft and pressure at the boundaries for each test.

	Liquid phase	**Vapor phase**
Density ρ [kg m^{-3}]	*User field function*	0.1361
Dynamic viscosity μ [Pa s]	0.001672	5.953 10^{-6}
$\frac{\mathrm{d}\rho}{\mathrm{d}p}$ [s^{2}m^{-2}]	5.6532 10^{-7}	-
Molecular weight W [kg kmol^{-1}]	170	170
Surface tension γ [N m^{-1}]	0.029	-
Sound speed c [m s^{-1}]	1330	632
Saturation pressure [Pa]	*User field function*	

Table 5.2: Physical proprieties of liquid and vapor phases of Diesel.

With the experience gained from the converging-diverging nozzle, the cavitation model is enabled and the Reboud's correction for the turbulent viscosity is implemented. Through several tests, the Rayleigh-Plesset cavitation model returned the most reliable results, considering the expected cavitation regime. For this reason, all the results here presented are obtained using this model.

The procedure is very similar to the one that has been used for the Venturi test case. The solver is *Segregated flow*, it can handle mildly compressible flow but it is not suitable for capturing shocks and high Mach number; therefore the local shock waves produced by the collapse of the vapor pockets can not be detected. Moreover, the Useguide [45] suggests to model the vapor phase as incompressible gas.

Table 5.2 summarizes the physical proprieties of the liquid and gas phases; the *User field function* for the density of the liquid phase is the same used in the single phase flow described in the previous section. The numerical values are retrieved from the Master thesis by Andersen [5], who took them from the American Oil Chemical Society. Being the cavitation model enabled, it is necessary to define the saturation pressure. It is believed that the pressure oscillation in the turbulent flow might have an impact on the saturation pressure and, for this reason the correction proposed by Singhal [46] is applied. In particular, the saturation pressure is equal to:

$$p_{sat} = p_{sat0} + \frac{1}{2} 0.39 \rho_l k \tag{5.1}$$

where p_{sat0} is a constant and it depends on the fluid and operative conditions. In this case, it is equal to 5400 Pa. The time discretization is *Euler Second Order* and the time step is 2.5μs; this allows to have a Courant number less than 20 in the nozzle holes. As concern the mesh, a polyhedral geometry for the cell is used, base size and the refinement volumes are similar for all these tests. Since no limitation on the base size is required, prism layers are used. This helped to keep low the residuals of the turbulent dissipation rate function. The volume refinements are located close to the nozzle holes and in the small gaps of the mesh. On average, the number of cells for these simulations is 8 millions.

5.1.1 Case A: 55% Open

Let us start considering the cut-off shaft partially open, being the lift equal to 1.5 mm, 55% of the total displacement. Note, that it does not mean that the orifices are 55% uncovered by the cut-off shaft, since in the first 1.4 mm, the flow through the holes is not allowed.

The mass flow per holes is calculated and reported in table 5.3, in terms of mean value and standard deviation. As expected, the mass flow through the orifices H1 and H4 is the largest because of the inlet section area in these nozzle holes. Indeed, the injector is designed to allow the flow only through H1 and H4 in the first moments of SOI.

	Average	**Standard deviation**
Mass Flow H1 [kg/s]	0.1305	$4.748 \cdot 10^{-4}$
Mass Flow H2 [kg/s]	0.0197	$1.234 \cdot 10^{-4}$
Mass Flow H3 [kg/s]	0.0213	$7.985 \cdot 10^{-5}$
Mass Flow H4 [kg/s]	0.1031	0.0041

Table 5.3: Mass flow through the orifices when the valve is 55% open.

The reader might note that the standard deviations are low for all the nozzle holes, except H4, where it is one order of magnitude larger. The reason is the nucleation and growth of a vapor string, which has a transient behaviour because of the Reboud's correction. Recall, from the *Theory*, that the string cavitation is a completely different mechanism compared to hydrodynamic cavitation. The latter is due to the abrupt variation of the section area while the former is due to the pressure drop in the center of a vortex. It is interesting to note that the string cavitation has been found to prevail at low lift for VCO injectors too, as reported by Gavaises et al. [22] and Neroorkar et al. [37]. In addition, in certain conditions, the string cavitation might form in the sac volume [21].

(a) 1% Volume fraction of vapor. **(b)** 5% Volume fraction of vapor. **(c)** 10% Volume fraction of vapor.

Figure 5.1: A glimpse on cavitation phenomenon; percentage of volume of fraction of vapor; 1% in light blue, 5% in magenta, 10% in dark blue.

Figure 5.1 highlights the cells of the nozzles where the volume fraction of vapor is larger than 1%, 5% and 10%. A small amount of hydrodynamic cavitation might be observered in the orifice H1.

At this point, the following questions might arise: where does the string origin? And what are the reasons which allow the formation of the string? In order to answer these questions, it is interesting to study the streamlines. The streamlines are depicted in figure 5.2, together with the 25% volume fraction of vapor isosurfaces, from the bottom view. The streamlines clearly shows a swirling flow in the nozzle hole H4, while the streamlines are almost straight for the nozzle H1. It is believed that a vortex is formed in the spherical entrance of the nozzle. In fact, due to the impingement angle on the walls, the streamlines are redirected by the spherical shape. Under these circumstances, the velocity vectors at the entrance of the nozzle hole are far for being perpendicular to the inlet section area and the vortex might elongate through it. Lastly, the string cavitation might reach the outlet section. This result is particularly important for the study of the spray pattern: on one hand, the string cavitation enhances the primary break-up but, one the other, it limits the amount of fuel discharged in the cylinder.

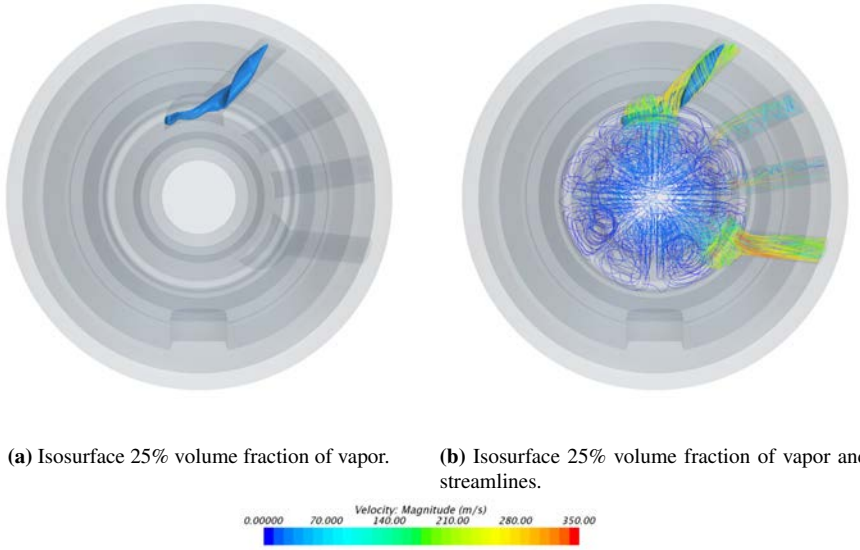

(a) Isosurface 25% volume fraction of vapor.

(b) Isosurface 25% volume fraction of vapor and streamlines.

Figure 5.2: Bottom view, iso-surface 25% of volume fraction of vapor and streamlines. A swirling flow might be clearly detected.

In order to assess the effect of the string cavitation on the erosion of the nozzle hole H4, it is interesting to evaluate the percent of the nozzle volume occupied by the vapor. This has been achieved through *User field functions*; they select the volume of interest (the nozzle

holes) and the amount of vapour is calculated integrating the volume fraction of vapor. Another parameter which deserves special attention is the vapor mass flow through the nozzle holes. It might return useful information for the investigation of the spray pattern. The results are summarized in table 5.4, where the mean value and standard deviation are reported. In figure 5.3, the volume fraction of vapor in four cylindrical sections of the nozzle H4 are plotted.

Nozzle Hole	**Percentage Volume**		**Vapor Mass flow**	
	Average [%]	Std. deviation [%]	Average [mg/s]	Std. deviation [mg/s]
H1	0.425	0.038	0.0912	0.0116
H2	0.012	0.004	-	-
H3	0.019	0.01	-	-
H4	11.65	0.47	2.190	0.170

Table 5.4: Percentage of volume occupied by the vapor in the nozzle holes and phase mass flow through the four orifices.

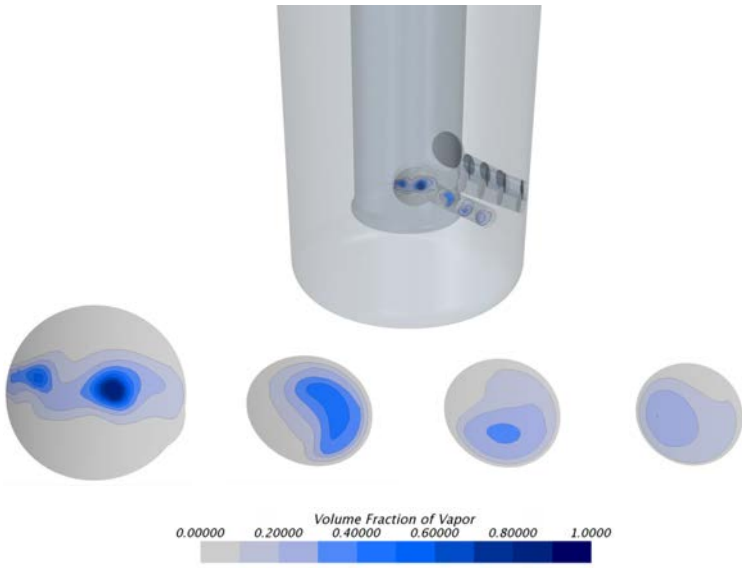

Figure 5.3: Volume fraction of vapour in four cylindrical section of the nozzle hole. The reference radii of the cylindrical surfaces coaxial with the injector are 3.5 mm, 4.5 mm, 5.5 mm, 6.5 mm.

Lastly, in figure 5.4 and 5.5 the velocity and the pressure field are depicted in planes intersecting the nozzles' axes and parallel to the injector's axis.

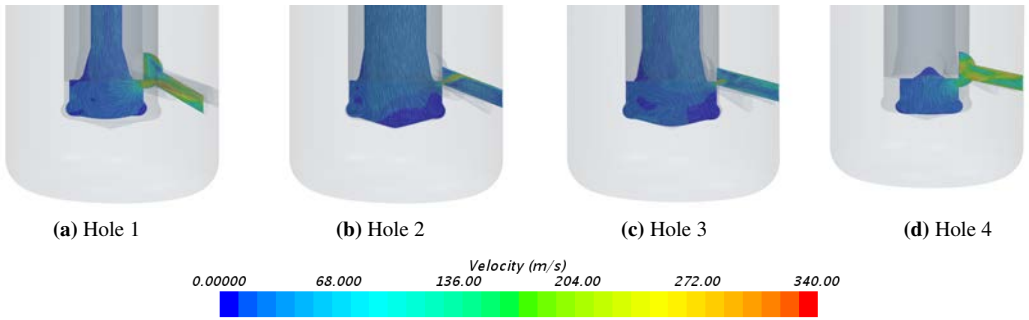

(a) Hole 1 **(b)** Hole 2 **(c)** Hole 3 **(d)** Hole 4

Figure 5.4: The velocity field (integral convolution) of the nozzle holes when the valve is 55% open

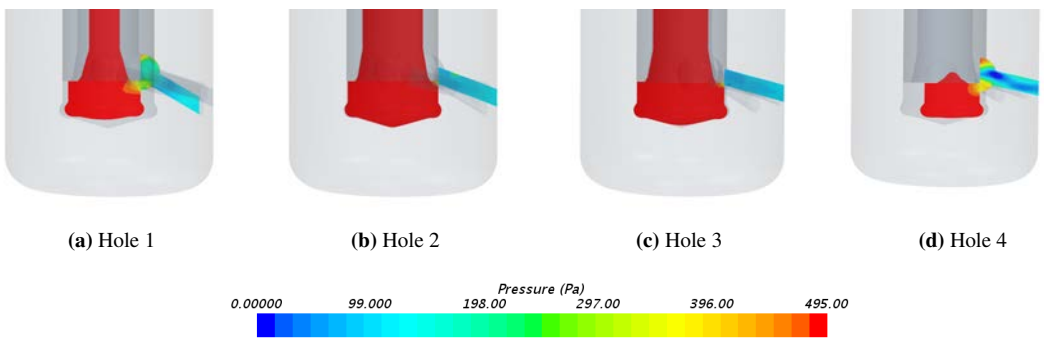

(a) Hole 1 **(b)** Hole 2 **(c)** Hole 3 **(d)** Hole 4

Figure 5.5: The pressure field of the nozzle holes when the valve is 55% open. Note the vortex structure in the nozzle hole 4, which causes the growth of the vapor string.

5.1.2 Case B: 75% Open

The displacement of the cut-off shaft from the seat is now equal to 2 mm, 75% of the total lift. As expected, the mass flow through the orifices is larger than the previous case; the mean values and the standard deviations are calculated and summarized in table 5.5.

	Average	**Standard deviation**
Mass Flow H1 [kg/s]	0.1650	$1.518 \cdot 10^{-4}$
Mass Flow H2 [kg/s]	0.1229	0.0023
Mass Flow H3 [kg/s]	0.1213	$2.747 \cdot 10^{-4}$
Mass Flow H4 [kg/s]	0.1683	$7.046 \cdot 10^{-4}$

Table 5.5: Mass flow through the orifices when the valve is 75% open.

As it might be observed from figure 5.6, all the nozzle holes exhibit a change of phase, due to cavitation. In particular, the orifices H2, H3 and H4 experience the toughest cavitation regime. From the analysis of the scalar field volume fraction if vapor, the hydrodynamic cavitation is observed in H2 and H3. In the latter, a string forms behind the portion of the cut-off shaft which still covers the orifice. The string combines with the cavity pocket due to hydrodynamic cavitation and elongates until the outlet section. String cavitation and swirling flow is still present in nozzle H4. The swirling flow seems to have a large intensity in nozzle H3 too. Table 5.5 shows that the standard deviation is quite low for all the nozzles except H2; here the standard deviation is one order of magnitude larger than the others. The analysis of the mass flow for this nozzle hole show a periodic shedding with a frequency equal to 7600 Hz.

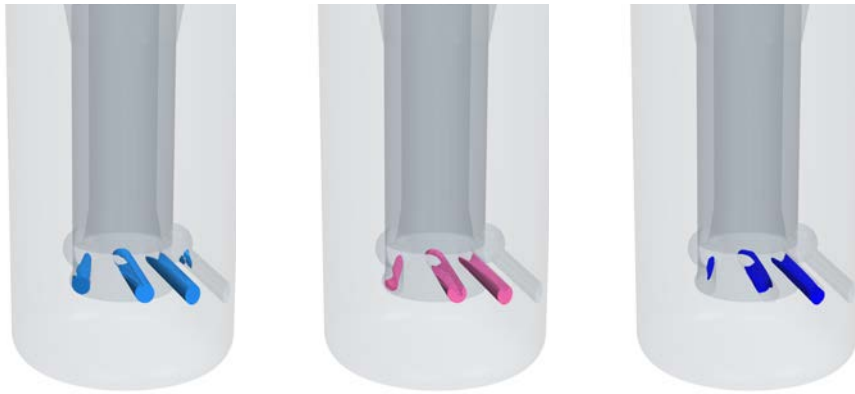

(a) 1% Volume fraction of vapor. **(b)** 5% Volume fraction of vapor. **(c)** 10% Volume fraction of vapor.

Figure 5.6: A glimpse on the cavitation phenomenon, percentage of volume of fraction of vapor; 1% in light blue, 5% in magenta, 10% in dark blue.

The streamlines and the isosurfaces for the volume fraction 5% are depicted in figure 5.7,

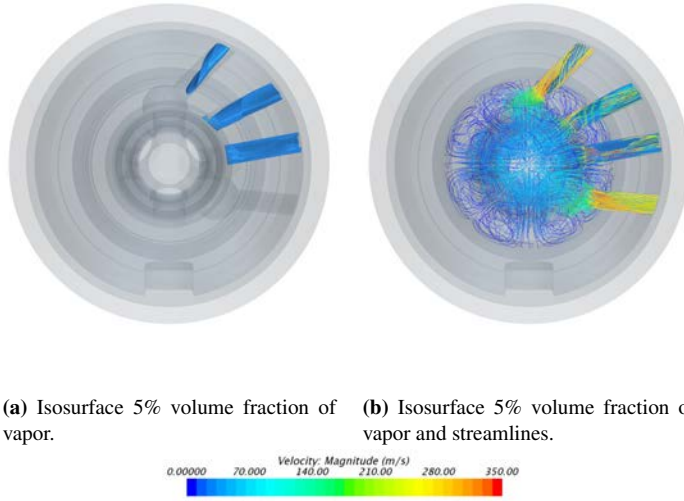

(a) Isosurface 5% volume fraction of vapor.

(b) Isosurface 5% volume fraction of vapor and streamlines.

Figure 5.7: Bottom view, isosurface 5% of volume fraction of vapor and streamlines.

from the bottom view. In order to assess the effect of the collapsing vapor bubbles on the erosion of the injector, the percentage of the volume occupied by the vapor is monitored for each nozzle holes. This has been achieved defining the regions of interest (the nozzle holes) through *User field functions* and integrating the volume fraction of vapor in those regions. The Reboud's correction makes the function unsteady, especially as concern the nozzle hole H2. The fluctuations have the same frequency of the total mass flow through the nozzle H2, around 7600 Hz; this is in agreement with the previous result. Since the amount of the vapor phase at the exit has an impact on the primary break-off of the fuel jet, the vapor mass flow has been monitored for each orifice and it is reported in table 5.6, together with the values of the previous function.

Nozzle Hole	**Percentage Volume**		**Vapor Mass flow**	
	Average [%]	Std. deviation [%]	Average [mg/s]	Std. deviation [mg/s]
H1	0.267	0.125	0.1401	0.0469
H2	11.13	2.48	1.1517	0.1412
H3	6.39	0.39	0.8674	0.0486
H4	0.874	0.299	0.5958	0.2083

Table 5.6: Percentage of volume occupied by the vapor in the nozzle holes and phase mass flow through the four orifices.

In figure 5.8, the field function volume fraction of vapor has been plotted in four cylindrical sections, coaxial with the injector and with radii 3.5 mm, 4.5 mm, 5.5 mm and 6.5 mm.

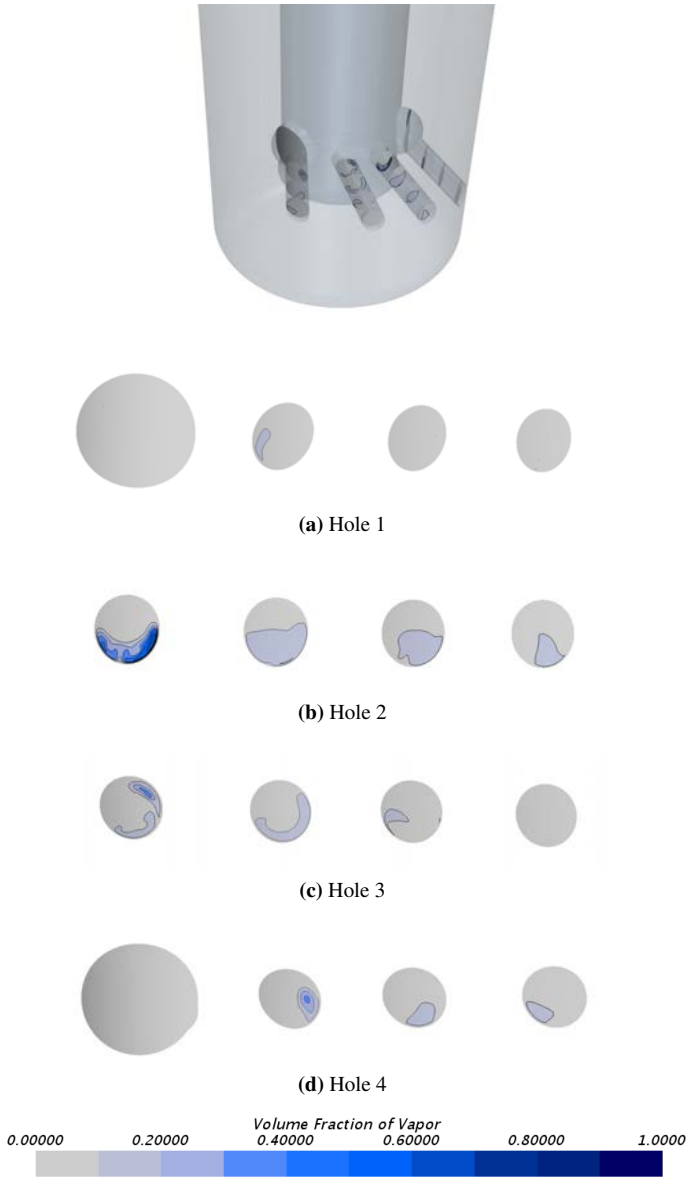

(a) Hole 1

(b) Hole 2

(c) Hole 3

(d) Hole 4

Figure 5.8: Iso-surface (10% of the volume fraction of vapor) and streamlines when the valve is 75% open

The velocity and the pressure field in quasi-steady state is reported in figure 5.9 and 5.10 for each orifices, in the section plane intersecting the nozzle's axis.

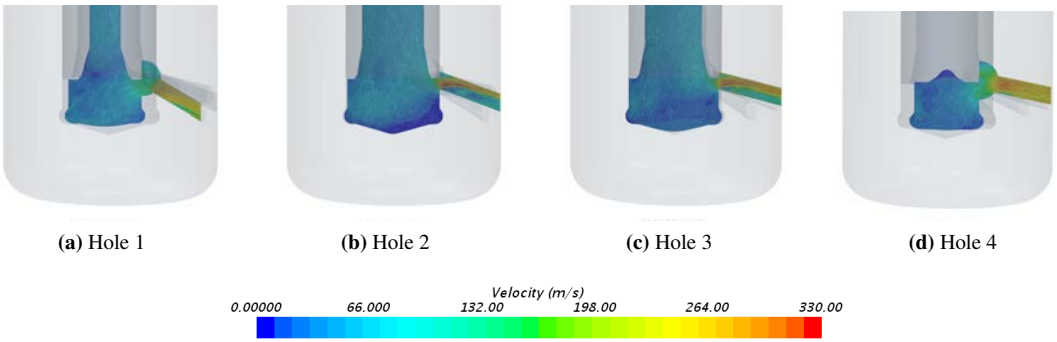

(a) Hole 1 **(b)** Hole 2 **(c)** Hole 3 **(d)** Hole 4

Figure 5.9: The velocity field (integral convolution) of the nozzle holes when the valve is 75% open

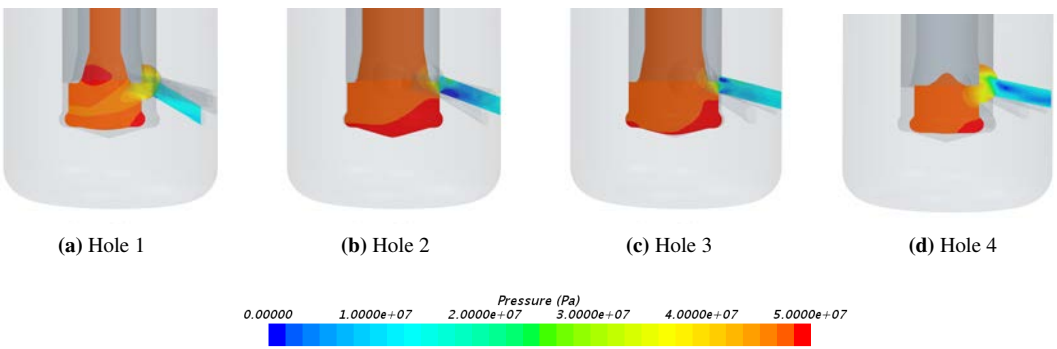

(a) Hole 1 **(b)** Hole 2 **(c)** Hole 3 **(d)** Hole 4

Figure 5.10: The pressure field of the nozzle holes when the valve is 75% open

5.1.3 Case C: 100% Open

Among the simulations in steady conditions, the case with the valve completely open is the most relevant. In fact, it is the only test aimed at reproducing the actual operative condition of the injector. When the fuel valve is fully open in the injection process, the steady condition is achieved. In addition to that, this test allows to make an assessment of the model against the data from MAN Energy Solutions. The company provided a chart which relates the discharge coefficient with the square root of the cavitation number K.
Firstly, it is convenient to calculate the cavitation number in order to predict the cavitation regime. The cavitation number CN is equal to:

$$\text{CN} = \frac{p_i - p_o}{p_o - p_{sat}} = \frac{(722 - 170) \cdot 10^5}{170 \cdot 10^5 - 5400} = 3.25 \tag{5.2}$$

where the inlet pressure, p_i, is recorded by a probe located in the sac volume. From the chart in figure 2.5, which relates the inverse of the cavitation number, CN^{-1} with the cavitation length, the super-cavitation regime is expected. A vapor film should form around the wall of the nozzles holes and it should reach the outlet section. It is likely to happen in nozzles H2 and H3, where there is an abrupt variation in the section area from the sac to the entrance of the orifices. The smooth curvature around the inlet of H1 and H4 should make cavitation unlikely to appear; in addition to that, the nozzle H1 and H4 are slightly longer than the other two and it contributes to increase the pressure in the region of vena contracta.

Once that the steady condition has been reached, the average and the standard deviation of the mass flow can be evaluated. The mean value and the standard deviation are calculated and presented in table 5.7:

	Average	**Standard deviation**
Mass Flow H1 [kg/s]	0.2061	0.003
Mass Flow H2 [kg/s]	0.1989	0.006
Mass Flow H3 [kg/s]	0.2054	0.002
Mass Flow H4 [kg/s]	0.2240	0.002

Table 5.7: Mass flow through the orifices when the valve is at full lift.

In order to make an assessment against the data from MAN, the discharge coefficient, C_d, must be calculated. Recall the definition of this non dimensional quantity: it is the ratio between the actual and the theoretical mass flow:

$$C_d = \frac{\dot{m}}{A_o \rho U_b} \tag{5.3}$$

where U_b is the velocity in the outlet section and it is calculated from the Bernoulli equation (see eq.(2.1)):

$$U_b = \sqrt{\frac{2(p_i - p_o)}{\rho}} \tag{5.4}$$

Here, p_i and p_o are, in turn, the pressure at the entrance (in the sac) and exit of the nozzle holes. Using the values recorded by *point probes* located in strategical position, the theoretical mass flow is calculated:

$$\begin{aligned}\dot{m}_{th} &= \left(\frac{D^2\pi}{4}\right)\cdot\rho\cdot\sqrt{\frac{2(p_i-p_o)}{\rho}} \\ &= \left(\frac{(1.05\cdot10^{-3})^2\pi}{4}\right)\cdot 876\cdot\sqrt{\frac{2(722-170)10^5}{876}} \\ &= 0.2693 \text{ kg/s}\end{aligned}$$

Before proceeding with the assessment, the square root of the cavitation number K is equal to:

$$\sqrt{\mathrm{K}} = \sqrt{\frac{p_i - p_{sat}}{p_i - p_o}} = \sqrt{\frac{722\cdot10^5 - 5400}{722\cdot10^5 - 170\cdot10^5}} = \sqrt{1.308} = 1.146 \tag{5.5}$$

The theoretical momentum flow could be calculated as follows:

$$\dot{M} = 2A_o(p_i - p_o) = 2\cdot\left(\frac{(1.05\cdot10^{-3})^2\pi}{4}\right)(722-170)\cdot10^5 = 95.6 \text{ N} \tag{5.6}$$

The discharge coefficient and momentum coefficient are summarized for each of the four nozzle holes in table 5.8 and plotted against the data from MAN in figure 5.11. The results are in agreement with the data from the company, especially as concerns the nozzles H2 and H3. For the nozzle H1 and H4, my results show an underestimation of the discharge coefficient which might be attributed to a different physical model (especially, Reboud and Singhal' corrections).

	H1	**H2**	**H3**	**H4**
Discharge coefficient C_d	0.7654	0.7386	0.7629	0.8318
Momentum coefficient C_m	0.6259	0.6003	0.6326	0.7605

Table 5.8: Non dimensional coefficient in the outlet section of the nozzle holes

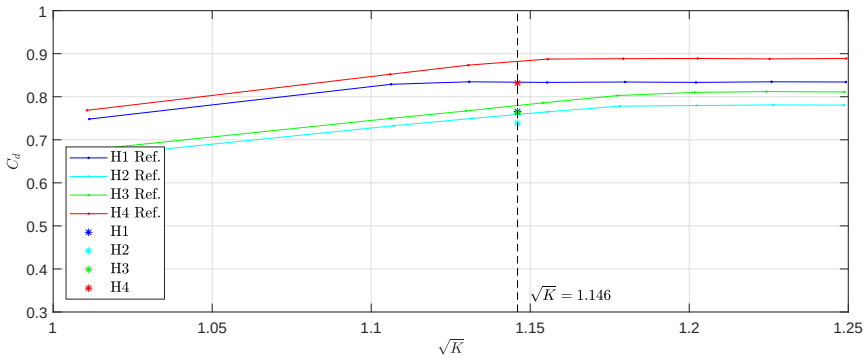

Figure 5.11: Discharge coefficient through the nozzle holes and reference data from MAN Energy Solutions.

It was demonstrated in the *Theory* section that the pressure distribution along the length of a one-dimensional nozzle gives information about the cavitation regime (refer to figure 2.4 for the one dimensional case). For this reason, two *linear probes* are located along the symmetry axis and the inferior wall with the aim of recording the pressure. The results are depicted in figure 5.12, where the outlet pressure has been plotted too. At the entrance, all the nozzle holes exhibit a pressure drop; in particular, the *linear probe* close to the wall records a pressure below the saturation limit for all the nozzle holes. It takes approximately 2% of the nozzle length for the pressure to increase again in H1 and H4, while 10% in H2 and H3. This means that the most tumultuous cavitation regime is expected in H2 and H3. This result was expected because of the absence of a smooth entrance. The cavitating flow through the nozzle holes might be observed in figure 5.13, where the cells with the volume fraction of vapor above 1%, 5% and 10% have been highlighted.

As in the previous analysis, the percentage of volume occupied by the vapor in the nozzle hole and the phase mass flow are calculated and they are reported in table 5.9.

Nozzle Hole	**Percentage Volume**		**Vapor Mass flow**	
	Average [%]	Std. deviation [%]	Average [mg/s]	Std. deviation [mg/s]
H1	0.0892	0.0213	0.0441	0.0188
H2	4.5059	0.3883	1.0454	0.1483
H3	3.5120	0.2120	0.699	0.0581
H4	0.4434	0.0158	0.4176	0.0190

Table 5.9: Percentage of volume occupied by the vapor in the nozzle holes and phase mass flow through the four orifices for the full lift case.

(a) 1% Volume fraction of vapor. **(b)** 5% Volume fraction of vapor. **(c)** 10% Volume fraction of vapor.

Figure 5.13: A glimpse on the cavitation phenomenon when the fuel valve is at full lift. The cells with the volume fraction of vapor larger than a threshold have been highlighted; 1% in light blue, 5% in magenta, 10% in dark blue.

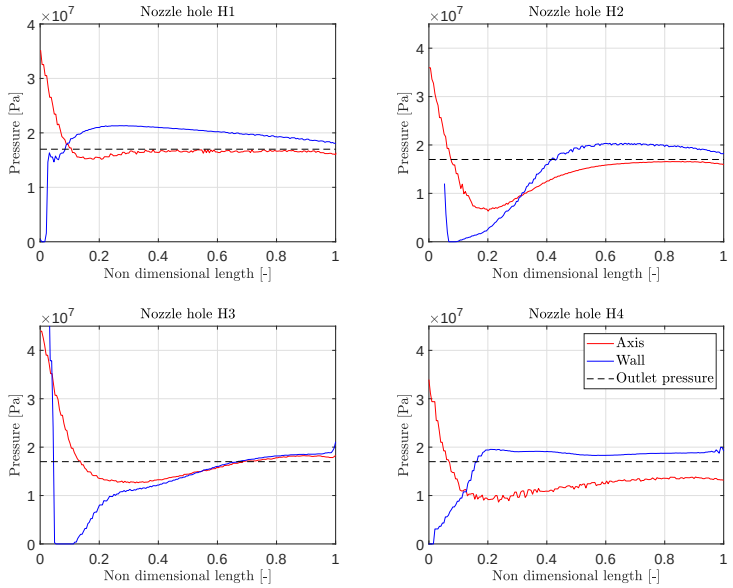

Figure 5.12: Pressure distribution along the symmetry axis and the inferior wall of the four nozzle holes

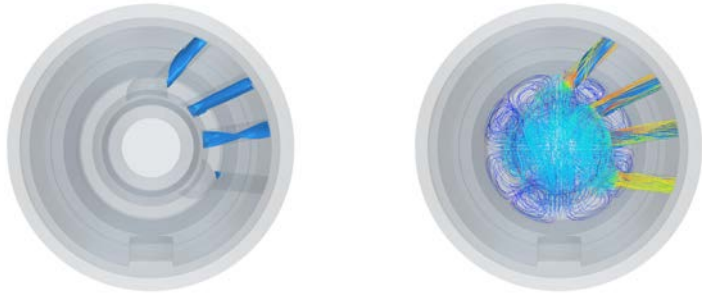

(a) Isosurface 2% volume fraction of vapor.

(b) Isosurface 2% volume fraction of vapor and streamlines.

Figure 5.14: Bottom view, iso-surface 5% of volume fraction of vapor and streamlines.

Lastly, the velocity and the pressure field for significant sections of the nozzle holes are depicted in figure 5.15 and 5.16.

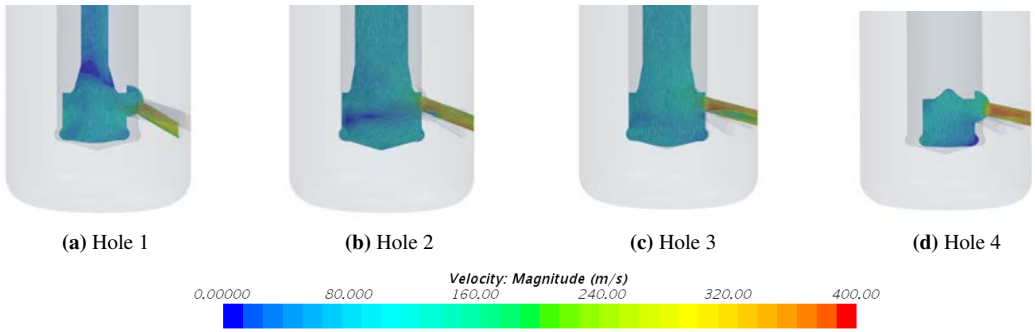

(a) Hole 1 **(b)** Hole 2 **(c)** Hole 3 **(d)** Hole 4

Figure 5.15: The velocity field (integral convolution) of the nozzle holes when the valve is 100% open

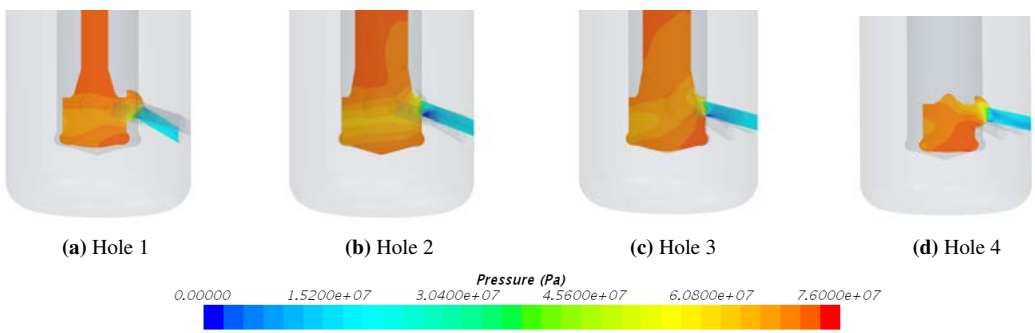

(a) Hole 1 **(b)** Hole 2 **(c)** Hole 3 **(d)** Hole 4

Figure 5.16: The pressure field of the nozzle holes when the valve is 100% open. The reader could note the vortex core in the sac in the picture of the nozzle H2.

5.2 Transient simulation

The previous simulations were run in steady conditions, meaning that the needle was still and the pressure at the boundaries was constant. The next step consists in introducing the actual operative pressure conditions and the motion of the cut-off shaft by means of the overset technology. Because of the EOI limitations discussed in the previous chapter, only the SOI will be considered.

The trimmer mesh is used in this analysis since it is optimized to operate with the overset technology being the ”scaling” geometries only close to the edges of the orifices. The physical proprieties of the liquid and vapor phases are equal to those presented in table 4.5, while the reader might refer to figure 4.28 and 4.29 for the lift and the pressures at the boundaries versus time. The full Rayleigh-Plesset cavitation model is used. The transient analysis is aimed at answering the following questions: does the seat exhibit cavitation in the first moments of the opening as reported by several authors [8]? What is the relationship between the volume fraction of vapor and the lift? Lastly, is true that the difference between the transient and steady simulation might be negligible? Before start answering these questions, let us have a look at the mass flow and the momentum flow in figure 5.17 and 5.18 respectively.

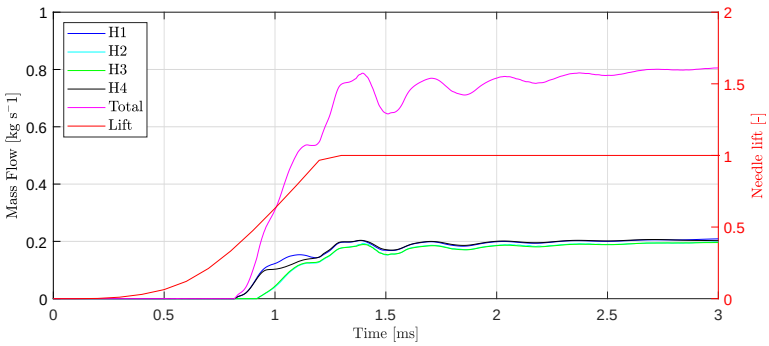

Figure 5.17: Mass flow through the four orifices and total mass flow versus time.

The plots of the mass and momentum flow look similar to those presented in the single phase flow during the opening of the fuel valve. In addition to that, even if the steady conditions have not been achieved yet, the mass and momentum flow in the last time step are in agreement with the values from the steady simulation and full lift. The fluctuations are due to the pressure wave travelling back and forth in the system with a frequency of around 3300 Hz, in a similar way of what has been discussed in the single phase flow validation case.

The solution is recorded in a .simh history file and the first instant of the disclosure event is reported in figure 5.19 for the velocity field, zooming on the seat. Being the geometry axisymmetric above the seat, only a section of the entire fluid domain is considered. Due to the pressure difference between the room above and below the seat, the velocity reaches

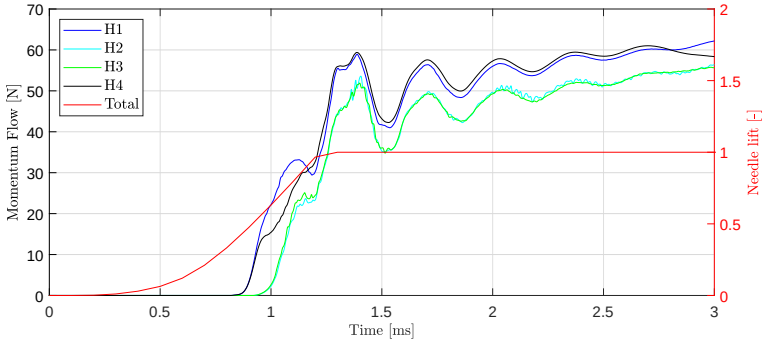

Figure 5.18: Momentum flow through the four orifices versus time.

the value of around 170 m/s in the gap between the two components. It is relevant to analyse the values of the pressure field in the same section, to check whether the pressure reaches the saturation limit, as a consequence of the pressure loss. With this purpose, figure 5.20 reports the pressure and the volume fraction of vapor scalar fields.
It was expected that the small cross sectional area could cause the growth of cavitation structures; indeed, Baumgartner [8] reports that the seat is a source of cavitation, second only to the entrance of the nozzle holes. It should be mentioned that Baumgartner mainly refers to VCO and mini-SAC injectors for the automotive industry, where the injection pressure is higher (around $1,800 \sim 2,000$ bar), as well as the pressure difference. In this model, cavitation structures are not observed. The region of interest was selected through a *User field function* and the volume of vapor was calculated, but the analysis returned a very small amount of vapor. In fact, from the volume fraction of vapor scalar field, it has the same magnitude of the volume fraction of vapour homogeneously distributed in the domain.

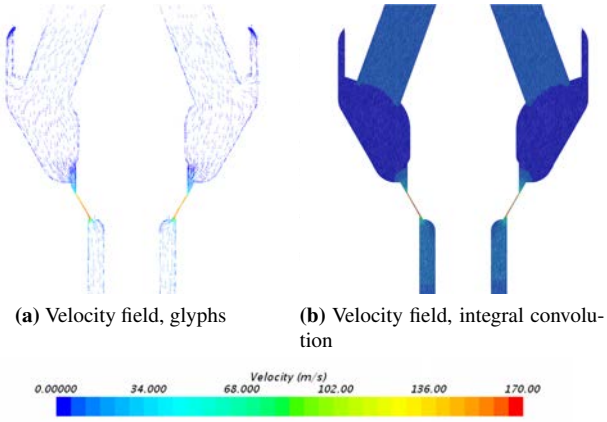

(a) Velocity field, glyphs

(b) Velocity field, integral convolution

Figure 5.19: Velocity field in the seat in the first instant of the SOI.

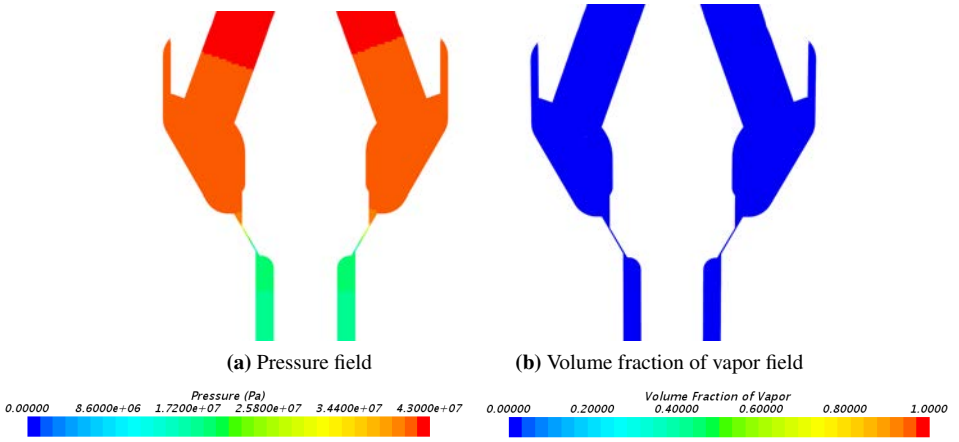

(a) Pressure field **(b)** Volume fraction of vapor field

Figure 5.20: Pressure and volume fraction of vapor scalar fields.

In order to provide data for assessing the erosion of the nozzle holes due to cavitation, the percentage of the nozzle volume occupied by vapor is calculated. The procedure is the same as the one used in the previous chapter, in the steady simulations. The phase mass flow through the orifices is monitored and plotted as well, with the aim of giving indication for the further analysis of the spray break-up and spray pattern. The plots are reported in figure 5.21 and 5.22 respectively. Both the plots shows a periodic trend once that the valve is at full lift. The fluctuations have the same frequency of the pressure wave travelling back and forth in the system. Ideally, once that the steady conditions are reached (from the single phase analysis around 8 ms are required), the values of the function should be in agreement with those reported in table 5.9.

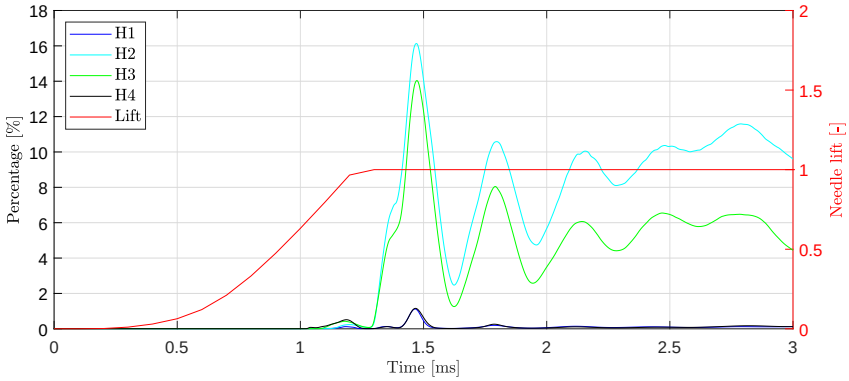

Figure 5.21: Percentage of the volume of the nozzle hole occupied by fuel vapor with respect to time.

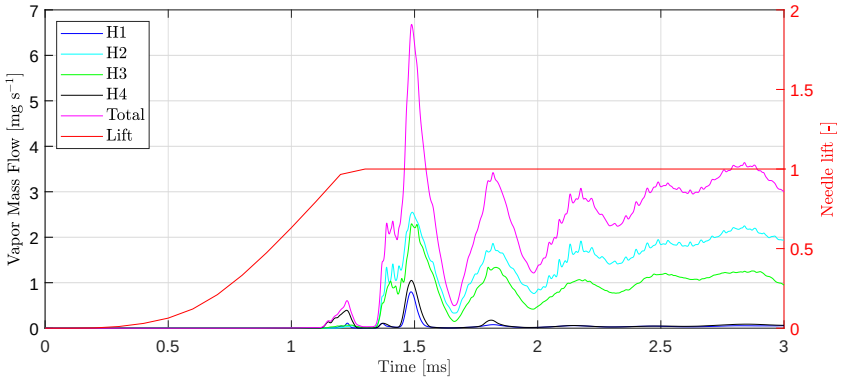

Figure 5.22: Phase mass flow through the four orifices versus time.

Lastly, it is interesting to conduct an analysis on the cavitation mechanism and the bubble morphology. For this reason, figure 5.23 shows the time evolution of the 10% isosurface of the scalar function volume fraction of vapor. In particular, the attention is addressed to the first peak of figure 5.21, from 1.25 ms to around 1.6 ms.

The first visible cavitation structure is observed at time 1.04 ms; it develops in the spherical entrance of the nozzle hole H4. At that time step, the lift of the spindle is approximately equal to 70 % of the maximum displacement. It is believed that the cavitation mechanism responsible for the growth of the bubble is the string cavitation. The pressure field in a section of the nozzle H4 shows a vortex, as it was predicted in the discussion of the single phase flow (in this regard, refer to figure 4.43) and in the steady simulation (75% of the total lift). The reason is discussed in the previous chapter and it is due to the impingement angle on the nozzle entrance; the streamlines follow the spherical shape of the entrance, which allows the vortex generation. In this time step the amount of vapor is very little, less than 1% of the volume of the nozzle hole. Just from this first analysis, it is clear that the simulation in transient condition differs from the previous simulation with steady condition at the boundaries and constant lift of the needle. At the time 1.36 ms, the onset of the largest production of vapor might be observed; at this point, the fuel valve is completely open. The hydrodynamic cavitation is the mechanism responsible for the vapor pockets in the nozzles H2 and H3; while, in the nozzle H1 and H2, a string stretches (elongates) in length. This situation might be observed in figure 5.23, where the highest peak of the vapor mass flow is located at time 1.46 ms. The volume of the nozzle occupied by the vapor reaches the 16% at its maximum. Note that this peak is in correspondence of the mass and momentum flow peaks, meaning that the fluctuations have the same phase. The pressure fluctuations in the system cause this behaviour. Increasing the time step, the string in nozzle H2 and H3 are tightened (time 1.58 ms) and they almost vanish (time 1.60 ms). The same cycle is replicated in the further time steps but the amplitude of the oscillation of the cavitation quantities is dumped.

As it was introduced in the previous paragraph, the difference between the steady and

transient solutions is not negligible and the overset technique is fundamental to predict the cavitation structures and morphology. This result was expected; the actual opening event lasts approximately 1 ms; this time span is not large enough to achieve the steady condition, meaning that the characteristic scalar and vector fields are different. This explains why, for instance, no vapor bubbles were observed when the needle was at 55% of the total lift. Anyways, the simulations in steady condition might be relevant for injections with a partial lift valve and duration longer than 8 ms, which is approximately the time required by the fluid to establish a steady behaviour.

It should be mentioned that these results were obtained limiting the minimum allowable absolute pressure to 0 Pa for the *Segregated solver*. As it was discussed in the validation of the single phase flow, it might not be a correct assumption. Experimental records showed that the cavitating fluid might withstand negative pressure being the fluid in a metastable state. For this reason, it is convenient to replicate the simulation setting a proper (coherent with the equation of state) negative limit for the absolute pressure. A brief analysis was performed but the results were non-physical: the pressure in the sac reaches the saturation limit for the first milliseconds of the simulation. It is suspected that the negative limit could cause this behaviour and it is advisable to contact the *STAR CCM+* engineers to obtain more information about the effect of this modification in the numerical model.

(a) $t = 1.04$ ms **(b)** $t = 1.30$ ms **(c)** $t = 1.36$ ms **(d)** $t = 1.42$ ms

(e) $t = 1.46$ ms **(f)** $t = 1.48$ ms **(g)** $t = 1.58$ ms **(h)** $t = 1.60$ ms

Figure 5.23: 10% volume fraction of vapor isosurface. Visualization of the cavitation regime in the first peak of figure 5.21.

Chapter 6

Conclusion

The study of this Master thesis allows to develop and tune-up a numerical CFD model for the in-nozzle flow during the opening and closing of the fuel valve. The overset technique is the technology chosen to reproduce the motion of the valve. The choice of the overset is justified by the good resolution of the small gaps during the entire transient process; this feature might not be fulfilled with other techniques. In addition to that, the Userguide of *STAR CCM+* [45] suggests to use this technique in case of opening and closing of valves.

Experiments about the actual injection conditions are not possible due to the high pressures involved in the process, the need of use optical technique to detect and study the morphology of the vapor bubbles, the dimensions of the nozzle holes and the fluid velocity (around 0.3$\sim$0.4 Ma). Therefore, only little information is available in literature. This lack of information forces to take a step back and validate the numerical model.

The first validation is about the transient cavitation; in fact, high transient cavitation structures are expected at the opening of the fuel valve. The question which arises is whether the standard cavitation model could reproduce correctly the dynamics of the vapor bubbles. For this reason, after a wide research in the literature, the experimental periodic cavitating flow inside a converging-diverging Venturi nozzle [28] is simulated numerically. The main assumptions of this test case are the use of the Unsteady Reynolds Averaged Navier-Stokes equations (URANS), the Eulerian multiphase Volume of Fraction method (VOF) and the axysimmetry. It is discovered that the turbulence model plays a relevant role in the shedding process. The large values of the turbulent viscosity do not permit to get the detachment of the vapor pocket; for this reason the correction proposed by Reboud is introduced. It consists in multiplying the turbulent viscosity by a scaling factor, which is function of the density field. This allows to reproduce the physics of the phenomenon with a larger accuracy and, in the best solution, the relative error of the shedding frequency is limited to 6%.

The second validation case is about the single phase flow in the injector during the tran-

sients, at the opening and closing of the fuel valve. The results are compared with a in-house code by MAN Energy Solutions named *1D-Hydcode*. The lack of the experimental data forces to use some of the output of the one-dimensional code as input in the CFD simulation. The opening event is well represented; through the use of the *Overset Zero Gap Interface* technology, the first instant of the opening is correctly detected. The mass flow and the pressure in the sac volume show a satisfying agreement with the *1D-Hydecode*. The plots of these quantities exhibit a phase displacement due to the different frequencies of the pressure wave travelling through the system. This result was expected considering that in the CFD simulation only three component of the full system are considered, while the *1D-Hydcode* is aimed at modelling the entire injector. In this analysis a vortex is observed in the sac volume; its core changes orientation with respect to time. In particular, when the steady conditions are achieved, it is aligned with two nozzle holes of the injector, leading to large fluctuations in mass and momentum flow. The results from the end of injection event can not be trusted; in this case, the misalignment between the hypotheses of the one-dimensional code and the CFD simulation (absence of EDM, different length of the system and, above all, the fact that in one model the motion is the consequence of the pressure acting on the surfaces of the cut-off shaft while in the other it is prescribed) leads to reversed flow and negative mass flow.

Before moving on to the transient and multiphase simulation, three tests were conducted with the valve partially open and at full lift. These test are aimed at checking whether there is a large difference in the cavitation morphology and in the mass and momentum values compared to the transient simulation. They permit to discover that different cavitation mechanisms appear in the nozzle holes. When the valve is a low lift, the string cavitation mechanism dominates; especially as regard the two nozzle holes having a spherical entrance. The impingement angle on the wall causes a vortex which stretches and elongates in the nozzles. A mix of vortex and hydrodynamic cavitation is observed when the spindle is at 75% of the total lift, while hydrodynamic cavitation prevails when the valve is at full lift. For each of these cases, the mass and momentum flow is calculated, as well as the volume occupied in the nozzle holes and the phase mass flow. These quantities will provide relevant information for further possible investigation of the erosion of the nozzles' walls due to the collapse of the vapor bubbles and the break-up of the fuel jet.

Lastly, the simulation with the moving valve and cavitation model is run. The amount of vapor follows the trend given by the pressure fluctuations in the fluid domain. Contrary to expectations, cavitation in the seat is not observed. The lack of experimental data does not allow to make safe statement, but it is believed that prescribing the motion of the spindle might have an effect on the cavitation in the gap between seat and spindle. As it will be widely discussed in the next chapter, further investigation should be conducted implementing the DFBI (Dynamic Fluid-Body Interaction) option, and coupling the cut-off shaft with a one-dimensional linear spring. In this way, the motion of the shaft might be due to the forces acting on it. The time evolution of the cavitation structure allows to conclude that the hydrodynamic cavitation prevails in the process but string cavitation is present in the nozzles with a smooth entrance too. The percentage of volume of the nozzle hole occupied by fuel vapor and the fuel vapor mass flow for each of the nozzle holes is

monitored and plotted versus time; providing information for further analyses.

6.1 Recommendations for the Future

With the experience gained working in the project, these improvements of the CFD model are suggested. Let us start from the mesh. The geometry of the moving part (the spindle) is quite complex; it is hollowed and it is not axisymmetric. The overset mesh was created simply reproducing the shape of the needle and using the Bolean operation subtract. This method works fine but it returns quite a loose fit; as a consequence of that, the mesh of overset is heavy and it has an impact on the CPU time. For this reason, I suggest to use a tighter fit. In this regard, some CAD software (for instance, *Solidworks*) allows to create offset surface from the actual body's surface. I believe that the tighter fit mesh might help in achieving the convergence of rate of dissipation term too.

It is important to recall that the overset technique is not mass conservative; in general, the error is negligible but, for this application, it is advisable to turn on the method *Flux correction* for compressible flow to enforce the continuity.

Further developments of the physical model might consist in coupling the one-dimensional code *1D-Hydcode* and *STAR CCM+*; in this way, the dynamic effects in the entire system might be replicated numerically. In this regard, instead of prescribing the motion, it might be convenient to model the motion of the spindle as a consequence of the pressure acting on its surfaces. This might be achieved using the DFBI (Dynamic Fluid Body Interaction) options; in particular, allowing the translation in the vertical coordinate (system with one degree of freedom) and modelling a linear spring coupling.

Once that the in-nozzle flow has been investigated, it is interesting to study the spray development in the cylinder too. Some numerical correlations between the needle position, cavitation structures and spray angle (or penetration length, Mean Sauer Diameter, ...) might be derived.

On the experimental side, it would be convenient to test the geometry of this project in the steady state rig and compare the results with the CFD solutions for the partial lift tests. In this way, the different cavitation mechanisms might be investigated experimentally too.

Bibliography

[1] https://www.youtube.com/watch?v=sHTf2wzDqVY, Accessed May 19, 2019.

[2] https://www.youtube.com/watch?v=7Y1rCU3kUm0, Accessed May 19, 2019.

[3] https://www.dieselnet.com/standards/inter/imo.php, Accessed May 7, 2019.

[4] https://www.cfdsupport.com/OpenFOAM-Training-by-CFD-Support/node199.html, Accessed May 8, 2019.

[5] F. H. Andersen. Numerical simulation of flow in fuel nozzles for two stroke diesel engines, 2011.

[6] E. H. Atta and J. Vadyak. A grid overlapping scheme for flowfield computations about multicomponent configurations. *American Institute of Aeronautics and Astronautics*, 21(9):1271–1277, 1983.

[7] C. Badock, R. Wirth, A. Fath, and A. Leipertz. Investigation of cavitation in real size diesel injector nozzle. *International Journal of Heat and Fluid Flow*, 20(5):538–544, 1999.

[8] Baumgartner. *Mixture Formation in Internal Combustion Engines*. Springer, 2006.

[9] R. Benson. *The Thermodynamics of gas dynamics of internal combustion engine*. Clarendon Press Oxford, 1982.

[10] W. Bergwerk. Flow pattern in diesel nozzle spray holes. *Proceedings of the Institution of Mechanical Engineers*, 173(25):655–660, 1959.

[11] H. B. Bingham, P. Larsen, and A. Barker. *Lecture Notes for CFD Course*. DTU Mekanik, 2018.

[12] M. Blessing, G. Konig, C. Kruger, U. Micheals, and V. Schwarz. Analysis of flow and cavitation phenomena in diesel injection nozzles and its effects on spray and mixture formation. *SAE International*, 1(1358), 2003.

[13] D. Bonilla, J. D. K. Bishop, C. J. Axon, and D. Banister. Innovation, the diesel engine and vehicle markets: Evidence from oecd engine patents. *Transportation Research*, 27:51–58, 2014.

[14] C. E. Brenner. *Cavitation and Bubble Dynamics*. Oxford University Press, 1995.

[15] M. Callenaere, J. Franc, J. Michel, and M. Riondet. The cavitation instability induced by the development of a re-entrant jet. *Journal of Fluid Mechanics*, 444:223–256, 2001.

[16] Y. Cengel, J. Cimbala, G. Cozzo, and C. Santoro. *Meccanica dei Fluidi*. McGraw Hill Educational, 3 edition, 2015.

[17] O. Coutier-Delgosha, R. Fortes-Patella, and J. Reboud. Evaluation of the turbulence model influence on the numerical simulation of unsteady cavitation. *ASME*, 125, 2003.

[18] B. Dam. Experimental and numerical investigations of sprays in two stroke diesel engines, 2007.

[19] J. M. Desantes, F. Salvador, M. Carreres, and J. Martinez-Lopez. Large eddy simulation analysis of the influence of the needle lift on the cavitation in diesel injector nozzles. *Journal of Automobile Engineering*, 229(4):407–423, 2014.

[20] J. Ferziger and M. Peric. *Computational Methods for Fluid Dynamics*. Springer, 2002.

[21] M. Gavaises, A. Andriotis, and C. Arcoumanis. Vortex flow and cavitation in diesel injector nozzles. *Journal of Fluid Mechanics*, 610:195–215, 2008.

[22] M. Gavaises, A. Andriotis, D. Papoulias, M. N., and A. Theodorakakos. Characterization of string cavitation in large-scale diesel nozzles with taperad holes. *Physics of Fluids*, 21, 2009.

[23] E. Giannadakis. Modeling of cavitation in automotive fuel injector nozzles, 2005.

[24] P. Gorkh, J. S. Schmidt, and N. Adams. Numerical investigation of cavitation-regimes in a converging-diverging nozzle. 10^{th} International Symposium on Cavitation, 2018.

[25] H. Hiroyatsu, M. Arai, and Shimizu. Break-up length of a liquid jet and internal flow in a nozzle. *ICLASS-91*, 26, 1991.

[26] W. Hogendoorn. Experimental investigation of cavitation regimes in a converging-diverging nozzle. 2017.

[27] J. Hult, P. Simmank, and S. Matlok. Interior flow and near-nozzle spray development in a marine-engine diesel fuel injector. *Experiments in Fluids*, 57(49), 2016.

[28] S. Jahangir, W. Hogendoorn, and C. Poelma. Dynamics of partial cavitation in an axisymmetric converging-diverging nozzle. *International Journal of Multiphase Flow*, 106:34–45, 2018.

[29] R. T. Knapp. Recent investigation of the mechanics of cavitation and cavitation damage. *ASME*, 1955.

[30] P. Krishaswamy. Flow modelling for partially cavitating hydrofoils, 2000.

[31] K. Kundu, I. M. Cohen, and D. Dowling. *Fluid Mechanics*. Elsevier, 2012.

[32] O. Lord Rayleigh. Viii. on the pressure developed in a liquid during the collapse of a spherical cavity. *The London, Edinburgh, and Dublin Philosophical Magazine and Journal of Science*, 34(200):94–98, 1917.

[33] S. Martynov. Numetical simulation of the cavitation process in diesel fuel injectors, 2005.

[34] P. Martí Gómez-Aldaraví. Development of a computational model for a simultaneous simulation of internal flow and spray break-up of the diesel injection process, 2014.

[35] T. Melissaris, N. Bulten, and T. van Terwisge. A numerical study on the shedding frequency of sheet cavitation. *VII International Conference on Computational methods in Marine Engineering*, 2017.

[36] S. B. Multu. *Lecture notes on turbulence*. DTU Mekanik, 2013.

[37] K. Neroorkar, C. Mitcham II, R. Grover Jr, and D. Schmidt. Simualtions and analysis of fuel flow in an injector including transient needle effects. *ILASS, Conference on Liquid Atomization and Spray System*, 2012.

[38] J. Nikuradse. Gesetzmäßigkeiten der turbulenten strömung in glatten rohren. *Forschung auf dem Gebiet des Ingenieurwesens*, page 1–36, 1932.

[39] W. H. Nurick. Orifice cavitation and its effects on spray mixing. *Journal of Fluids Engineering*, 98(4):681–687, 1976.

[40] S. Patankar and D. Spalding. A calculation procedure for heat, mass and momentum transfer in three-dimensional parabolic flows. *International Journal of Heat and Mass Transfer*, 15:1787–1806, 1972.

[41] R. Payri, J. Garcia, F. Salvador, and J. Gimeno. Using spray momentum flux measurements to understand the influence of diesel nozzle geometry on spray characteristics. *FUEL*, 84(5):551–561, 2005.

[42] M. S. Plesset. The dynamics of cavitation bubbles. *Journal of Applied Mechanics*, 16:277–282, 1949.

[43] J. Reboud, B. Stutz, and O. Coutier. Two-phase flow structure of cavitation: experiment and modelling of unstedy effects. *Third International Symposium on Cavitation*, 1998.

[44] K. Sato and Y. Saito. Unstable cavitation behavior in a circular-cylindrical orifice flow. *CAV 2001: Fourth International Symposium on Cavitation*, 2001.

[45] Siemens. *Simcenter STAR-CCM+ Documentation*. Siemens PLM Software, 2018.

[46] A. Singhal, H. Li, M. Athavale, and Y. Jiang. Mathematical basis and validation of the full cavitation model. *ASME FEDSM*, 2001.

[47] C. Stanley, T. Barber, B. Milton, and G. Rosengarten. Periodic cavitation shedding in a cylindrical orifice. *Exp Fluids*, 51:1189–1200, 2011.

[48] C. von Kuensberg Sarre, S. Kong, and R. Reitz. Modeling the effects of injector nozzle geometry on diesel sprays. *Society of Automotive Engineers*, 1999.

[49] D. Wilcox. *Turbulence Modeling for CFD*. DCW Industries, INC, 1993.

[50] D. Woodyard. *Pounder's Marine Diesel Engines and Gas Turbines*. Elsevier Butterworth-Heinemann, 2004.

[51] W. Yuan, J. Sauer, and G. H. Schnerr. Modeling and computation of unsteady cavitation flows in injection nozzles. *Mecanique & Industries*, 2:383–394, 2001.

Appendix

6.1.1 Equation of State for Compressible Liquid

This paragraph is intended to comment the equation of state used in the CFD simulations. In general, all the equations of state, $\rho = f(p, T)$ could be written in differential form as follows:

$$\mathrm{d}\rho = \left(\frac{\partial \rho}{\partial T}\right)_p \mathrm{d}T + \left(\frac{\partial \rho}{\partial p}\right)_T \mathrm{d}p \tag{6.1}$$

where the subscripts p and T are used in order to stress that the partial derivatives are obtained considering the pressure and temperature constant.

The coefficient of thermal expansion α is defined as:

$$\alpha = -\frac{1}{\rho}\left(\frac{\partial \rho}{\partial T}\right)_p \tag{6.2}$$

while the inverse of the bulk modulus, ε is equal to:

$$\varepsilon^{-1} = \frac{1}{\rho}\left(\frac{\partial \rho}{\partial p}\right)_T \tag{6.3}$$

Inserting these definitions in eq. (6.1):

$$\mathrm{d}\rho = -\alpha\rho \mathrm{d}T + \rho\varepsilon^{-1}\mathrm{d}p \tag{6.4}$$

When the fluid is a liquid, the coefficient of thermal expansion and the bulk modulus might be written as presented in eqs. (6.5) and (6.6):

$$\alpha = \alpha_0[1 + \alpha'(T - T_0)] \tag{6.5}$$

$$\varepsilon = \varepsilon_0[1 + \varepsilon'(p - p_0)] \tag{6.6}$$

The constants α' and α_0 are independent of pressure for a large range of values; ε' and ε_0 are temperature independent as well. In most of engineering application, the terms α' and ε' are negligible; therefore, inserting eqs.(6.5) and (6.6) in (6.4) and integrating, the following expression might be derived:

$$\ln\left(\frac{\rho}{\rho_0}\right) = \alpha_0(T - T_0) + \varepsilon_0^{-1}(p - p_0) \tag{6.7}$$

which is equivalent to:

$$\rho = \rho_0 \exp\left[-\alpha_0(T - T_0) + \varepsilon_0^{-1}(p - p_0)\right] \tag{6.8}$$

If $[-\alpha_0(T - T_0) + \varepsilon^{-1}(p - p_0)] \ll 1$, the exponential function $\exp(x) \approx 1 + x + o(x)$, then:

$$\rho = \rho_0(1 - \alpha_0(T - T_0) + \varepsilon_0^{-1}(p - p_0)) \tag{6.9}$$

The hypothesis of this work is that the temperature is constant, therefore the first term in the brackets might be neglected. By definition, the speed of sound is equal to:

$$c = \sqrt{\frac{\varepsilon_0}{\rho_0}} \tag{6.10}$$

It follows that $\varepsilon_0 = c^2 \rho_0$. With these considerations in mind, eq. (6.9) becomes:

$$\rho = \rho_0 + \frac{p}{c^2} \tag{6.11}$$

6.1.2 Pressure probe located close to the inlet

This section is aimed at showing the pressure fluctuations recorded by the point probe in the inlet of the injector during the single phase validation test.

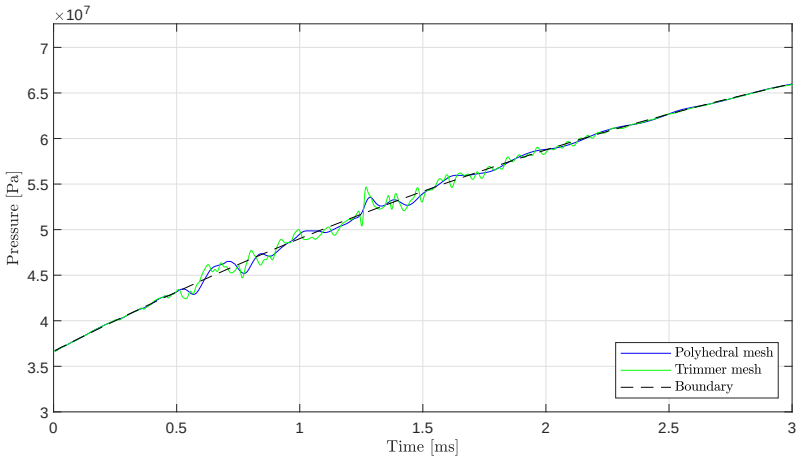

Figure 6.1: Pressure recorded by a point probe in the inlet of the injector.

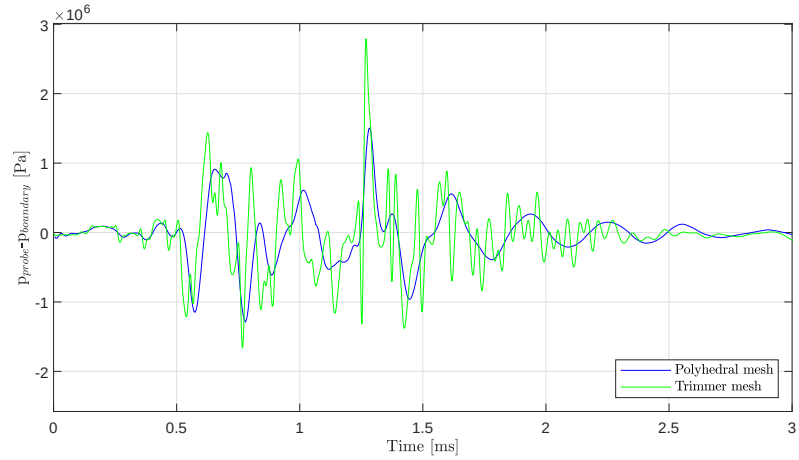

Figure 6.2: Pressure fluctuations at the inlet of the injector.

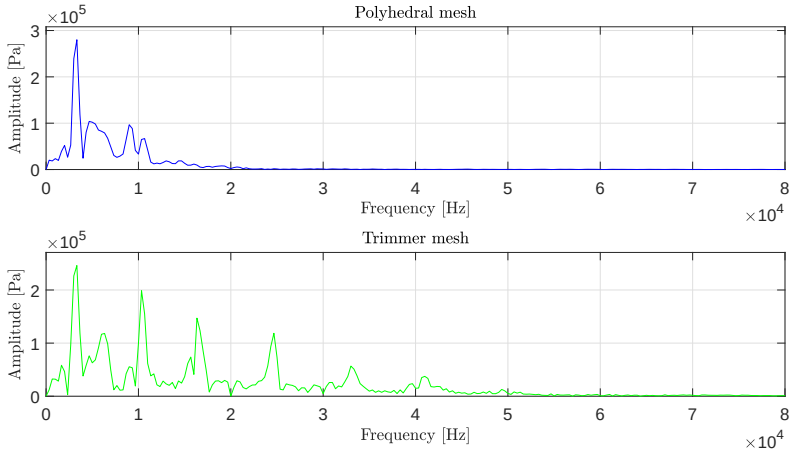

Figure 6.3: Analysis of the pressure signal in the frequency domain.

6.1.3 Single Phase, Closing Event

The additional plot of the momentum flow is here presented for the trimmer mesh.

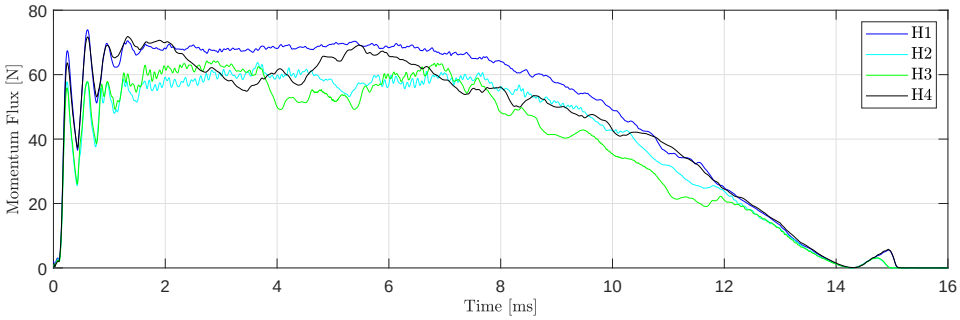

Figure 6.4: Momentum flow, end of injection. Results form the trimmer mesh.

6.1.4 Field Functions in *STAR CCM+*

Activate Source Term Schnerr-Sauer

```
($Time<$StartCavitation)?0:1
```

Density

```
836+$Pressure/(1330*1330)
```

H1

```
($$Position(CoordinateSystem("Laboratory.Cylindrical 1"))[0]>0.0032 &&
$$Position(CoordinateSystem("Laboratory.Cylindrical 1"))[1]>0.01 &&
$$Position(CoordinateSystem("Laboratory.Cylindrical 1"))[1]<1 &&
$$Position(CoordinateSystem("Laboratory.Cylindrical 1"))[2]<0 &&
$$Position(CoordinateSystem("Laboratory.Cylindrical 1"))[2]>-0.005)?1:0
```

H2

```
($$Position(CoordinateSystem("Laboratory.Cylindrical 1"))[0]>0.0031 &&
$$Position(CoordinateSystem("Laboratory.Cylindrical 1"))[1]>5.8 &&
$$Position(CoordinateSystem("Laboratory.Cylindrical 1"))[1]<8 &&
$$Position(CoordinateSystem("Laboratory.Cylindrical 1"))[2]<0 &&
$$Position(CoordinateSystem("Laboratory.Cylindrical 1"))[2]>-0.004005)?1:0
```

H3

```
($$Position(CoordinateSystem("Laboratory.Cylindrical 1"))[0]>0.003 &&
$$Position(CoordinateSystem("Laboratory.Cylindrical 1"))[1]>5.3 &&
$$Position(CoordinateSystem("Laboratory.Cylindrical 1"))[1]<5.8 &&
$$Position(CoordinateSystem("Laboratory.Cylindrical 1"))[2]<0 &&
$$Position(CoordinateSystem("Laboratory.Cylindrical 1"))[2]>-0.0038)?1:0
```

H4

```
($$Position(CoordinateSystem("Laboratory.Cylindrical 1"))[0]>0.003 &&
$$Position(CoordinateSystem("Laboratory.Cylindrical 1"))[1]>4.3 &&
$$Position(CoordinateSystem("Laboratory.Cylindrical 1"))[1]<5.3 &&
$$Position(CoordinateSystem("Laboratory.Cylindrical 1"))[2]<0 &&
$$Position(CoordinateSystem("Laboratory.Cylindrical 1"))[2]>-0.0038)?1:0
```

Initial condition

```
($$Position[1]<-0.2995)?12750000:36658930
```

Momentum flux

```
$Density*dot($$Velocity,$$Normal_2)*$$Velocity
```

Normal outward

```
$$Area*(-1/mag($$Area))
```

Pressure Cylinder

```
interpolateTable(@Table("CylPres"), "Time", LINEAR, "Pressure", $Time)
```

Pressure inlet

```
interpolateTable(@Table("PumpPres"), "Time", LINEAR, "Pressure", $Time)
```

Reboud

```
1/$Density*(0.1361+pow($Density 2-0.1361, $n)/pow(836-0.1361,$n-1))
```

Reboud coefficient

```
n=10
```

Seat

```
($$Position(CoordinateSystem("Laboratory.Cylindrical 2"))[0]>0 &&
$$Position(CoordinateSystem("Laboratory.Cylindrical 2"))[1]>0 &&
$$Position(CoordinateSystem("Laboratory.Cylindrical 2"))[1]<8 &&
$$Position(CoordinateSystem("Laboratory.Cylindrical 2"))[2]<-0.002 &&
$$Position(CoordinateSystem("Laboratory.Cylindrical 2"))[2]>-0.005)?1:0
```

Singhal

```
5400 + 0.5 * 0.39 *$DensityLiquid*$TurbulentKineticEnergy
```

Volume fraction of Vapor Seat

```
$Seat*$VolumeFractionVapor
```

Volume fraction of Vapor H1

```
$H1*$VolumeFractionVapor
```

Volume fraction of Vapor H2

```
$H2*$VolumeFractionVapor
```

Volume fraction of Vapor H3

```
$H3*$VolumeFractionVapor
```

Volume fraction of Vapor H4

```
$H4*$VolumeFractionVapor
```

The study of this Master thesis allows to develop and tune-up a numerical CFD model for the in-nozzle flow during the opening and closing of the fuel valve. The lack of the experimental data required the need of taking a step back and validate the model with two test cases: the periodic cavitating flow in a converging-diverging nozzle and the single phase flow inside the injector. After having shown a satisfying agreement with the reference data, the Rayleigh-Plesset cavitation model is implemented in the CFD model of the injector and the supercavitation regime is observed. The transient simulation demonstrated that both the mechanisms known as hydrodynamic and string cavitation appear in operative conditions.

Technical University of Denmark
DTU MEK
Section of Fluid Mechanics, Costal and Maritime Engineering

Nils Koppels Alle, Building 403

2800 Kgs. Lyngby

Denmark

www.mek.dtu.dk

Università degli Studi di Padova
Department of Industrial Engineering
Mechanical Engineering

via 8 Febbraio, 2

35122 Padova

Italy

www.im.dii.unipd.it